Title
Plasmonic Molecules Assembled by 3D DNA Origami Cage

Permalink
https://escholarship.org/uc/item/9qq7b65j

Author
Zhang, Yehan

Publication Date
2022

Peer reviewed|Thesis/dissertation

University of California, Merced

Plasmonic Molecules Assembled by 3D DNA Origami Cage

A dissertation submitted in partial satisfaction of the

requirements for the degree Doctor of Philosophy

in

Chemistry and Biochemistry

by

Yehan Zhang

2022

Committee Members:

Professor Son Nguyen, Chair

Professor Tao Ye, Advisor

Professor Erik Menke

Professor Jin Z. Zhang

The Dissertation of Yehan Zhang is approved, and it is acceptable in quality and form for publication on microfilm and in digital formats.

_____

Professor Tao Ye, Advisor

_____

Professor Erik Menke

_____

Professor Jin Z. Zhang

_____

Professor Son Nguyen, Chair

University of California, Merced

2022

To Nannan and Lynsi.

Table of Contents

Acknowledgements

First, I would like to express my sincere gratitude to my doctoral advisor, Dr. Tao Ye, for his guidance and support over the past six years at the University of California, Merced (UC, Merced) especially during the Pandemic. It is a long and difficult journey during which I have matured into an independent thinker.

Next, I would like to thank my committee, Dr. Son Nguyen, Dr. Erik Menke and Dr. Jin Z. Zhang for their continuous support over these years, and for their precious feedback and advice.

In addition, I take this opportunity to express my gratitude to the faculty and staff in chemistry and biochemistry department of UC, Merced. I received a lot of help in and out of the classroom, and it has been great joy to work with them over the past six years.

I want to thank my master thesis advisor, Dr. Simon J. Garrett, whose appreciations encouraged me to pursue PhD education. My thanks also go to Dr. Xiao Cai, a lifelong friend who "lured" me to UC, Merced, Kennedy Nguyen for his help with electron microscopes and Dr. A'Lester Allen for Raman data acquisitions and discussions.

I am very grateful to my lab mates in Dr. Tao Ye's research group: Dr. Huan H. Cao, a great friend who has mentored me tremendously when I first joined this group; Zachary J. Petrek, Melissa C. Goodlad, Paniz Rahmani, Warren A. Nanney, Dr. Qufei Gu and Devanshu Kumar, who are reliable friends and offered invaluable help and discussions over these years. My heart-felt thanks are also extended to Jasdip Singh, William Zhang, Vianna G. Martinez, Yichen Li, Rambod Rezayan, Uriel P. Reyes, Angel Avalos, Joshua Marquez and Dr. Gary R. Abel, Jr.

Special recognitions go to my family. I am extremely grateful to my mom and dad for their unconditional love and democratic parenting. I am grateful to my maternal grandmother, who gives me a healthy and worry-free childhood. I would also thank my maternal uncle Zhijun, who inspired me to pursue higher education across the Pacific Ocean. I would like to thank my cat for her company when I worked on computers at nights.

Finally, I would express my deepest gratitude to my better half Nannan and all my love to our baby daughter Lynsi. Nannan, you are the light of my life and nothing would I accomplish without your love and support.

Curriculum Vitae

Yehan Zhang

Education:

- **PhD** Chemistry and Biochemistry
  University of California, Merced (2016-2022)

- **M.S** Analytical Chemistry
  California State University, Northridge (2011-2015)

- **BEng** Chemical Engineering and Technology
  Changzhou University, China (2006-2010)

Research Experience:

- Merced Nanomaterials Centers for Energy & Sensing (MACES) (2017-2022)
- Tao Ye Lab, Chemistry and Biochemistry, UC Merced (2017-2022)
- Simon J. Garrett Lab, Chemistry and Biochemistry, California State University, Northridge (2012-2015)

Publications:

- Cao, H.H., Abel, G.R., Gu, Q., Gueorguieva, G.A.V., Zhang, Y., Nanney, W.A., Provencio, E.T. and Ye, T., 2020. Seeding the Self-Assembly of DNA Origamis at Surfaces. ACS nano.
- Gu, Q., Cao, H. H., Zhang, Y., Wang, H., Petrek, Z. J., Shi, F., ... & Ye, T. (2020). Toward a Quantitative Relationship between Nanoscale Spatial Organization and Hybridization Kinetics of Surface Immobilized Hairpin DNA Probes. ACS sensors.
- Gu, Q., Zhang, Y., Cao, H. H., Ye, S., & Ye, T. (2021). Transfer of Thiolated DNA Staples from DNA Origami Nanostructures to Self-Assembled Monolayer-Passivated Gold Surfaces: Implications for Interfacial Molecular Recognition. ACS Applied Nano Materials, 4(8), 8429-8436.
- Rahmani, P., Goodlad, M., Zhang, Y., Li, Y., & Ye, T. (2022). One-Step Ligand-Exchange Method to Produce Quantum Dot–DNA Conjugates for DNA-Directed Self-Assembly. ACS Applied Materials & Interfaces, 14(42), 47359-47368.

Presentations:

- TMS Annual Meeting & Exhibition, San Diego, 2014
  "Dealloying and Corrosion Behavior of a Pd-based Metallic Glass"
- ACS 255th National Meeting & Exhibition, New Orleans, 2018
  "Organize Gold Nanoparticles by DNA Origami Cage"
- Molecular Foundry Annual User Meeting (Virtual), 2020
  "Making Linear Heterotrimeric Nanolenses"
- MACES Energy Efficiency Thrust Meeting, UC, Merced, 2020
  "Making Linear Heterotrimeric Nanolenses"

Teaching Experience:

- Worked as teaching assistant for General Chemistry in California State University, Northridge (2012-2015)
- Worked as teaching assistant for General Chemistry, Organic Chemistry, Physical Chemistry and Analytical Chemistry in UC, Merced (2016-2022)
- Directed, filmed, and edited instructional videos for Instrumental Analytical Lab in UC, Merced (2020)
- Trained and mentored over 10 undergraduate students in research lab

Awards and Honors:

- Changzhou University Third Prize Scholarship (2006, 2008)
- Excellence Award of Knowledge Competition of Jiangsu Province (2007)
- Graduate Research Fellowship (2017, 2022)
- UC Merced Chemistry and Chemical Biology Summer Fellowship (2018)
- UC Merced Chemistry and Chemical Biology Travel Fellowship (2018)
- NASA-funded MACES Travel Fellowship (2018)
- NASA-funded MACES Summer Fellowship (2018-2022)
- Departmental Outstanding Teaching Assistant Award (2022)

Abstract of the Dissertation

Plasmonic Molecules Assembled by 3D DNA Origami Cage

by

Yehan Zhang

Doctor of Philosophy in Chemistry and Biochemistry

University of California, Merced, 2022

Plasmonic molecules are small assemblies of metal nanoparticles with definitive bond angles and gap sizes. Simulations predict plasmonic molecules support strong plasmonic coupling and have other interesting plasmonic effects, which make them attractive for numerous optical, sensing applications and investigative tools for fundamental plasmonic theories. Despite the promising simulation results, the syntheses of those plasmonic molecules are challenging because the current assembly approaches cannot precisely control the geometry of these assemblies, especially when the constituent nanoparticles have disparate sizes. Consequently, the plasmonic coupling within these assembled structures is often much lower than that predicted by simulations of ideal plasmonic molecules. To unleash the enormous potentials in plasmonic molecules, it is critical to organize different-sized nanoparticles with well-defined bond angles and gap sizes.

This dissertation describes two new stepwise assembly approaches to form linear trimeric plasmonic molecules that consist of two large nanoparticles flanking a small nanoparticle, which can serve as plasmonic lenses concentrating intense electric fields in the inter-particle gap. Both approaches use a DNA origami cage to encapsulate the DNA functionalized central particle. In the first approach, termed docking to DNA origami cage (D-DOC), the two

DNA functionalized terminal nanoparticles bind to the openings of the cage via hybridization with capture strands. In the second approach, termed cage-constrained inter-particle hybridization (CCIPH), the terminal nanoparticles are connected to the central nanoparticle as their ligands hybridize with the ligands of the central nanoparticle exposed at the two cage openings. These two approaches have been used to align the centers of 10 nm, 30 nm, and 50 nm gold nanoparticles into plasmonic heterotrimeric molecules. Two symmetric timers and an asymmetric trimer are synthesized, and each assembly step is investigated. For all three trimers, structural analyzes are conducted by scanning electron microscopy (SEM) to assess the bond angles and gap distances. The plasmonic effects of two symmetric trimers are evaluated by UV-Vis absorption spectroscopy and Raman spectroscopy. In accordance with experimental data, extensive finite-difference time-domain (FDTD) simulations are performed. The bond angles and gap sizes of our assembled plasmonic molecules are precisely defined, and one of our model trimers shows strong plasmonic coupling and expected surface enhanced Raman scattering enhancement factor. The optimizations and future directions of these two assembly approaches are also discussed.

List of Figures

List of Tables

Chapter 1: Introduction

1.1 Overview

63 years ago in Pasadena, Richard Feynman gave a famous lecture 'plenty room at the bottom' where he described a new field of controlling things on a small scale.[1] Later the term "nanotechnology" was given to this field by Norio Taniguchi (1974) and K. Eric Drexler (1986) independently.[2] The term nano means dwarf in Greek, and extremely small in modern English, the exact definition of nano is one billionth, one nanometer (nm) is then one billionth of a meter (m). It is difficult to imagine how small one nanometer is, take hummingbird as an example, the smallest bee hummingbird is ~5 centimeters (cm) in length, if using nanoscale, this tiny bird then becomes a 50,000,000-nanometer 'behemoth'. Tiny but mighty, nanotechnology has grown into a burgeoning multi-disciplinary field claiming multiple Nobel prizes.[3-4] As its name suggests, nanotechnology is all about sizes ranging from 1 nm-1,000 nm. In other words, nanotechnology sits on the border of the intuitive classical (bulk) and counterintuitive quantum (molecular) realms.[5] Scientists have long noticed properties are tied to size effects,[6] for instance, the bulk gold has shining golden color but gold nanoparticles display a myriad of colors depending on their sizes (Fig.1.1). However, the discovery of these interesting properties was not new, as early as twentieth and third century B.C., Chinese and Egyptian artists used nanoparticles to make colored ceramics,[7-8] later in 4th century A.D. Roman craftsmen made the famous Lycurgus cup (Fig.1.2), the epitome of ancient applications.[9] There is a hiatus between knowing and understanding, these ancient applications, though very artistic, were entirely empirical and often lost to history. Thanks to the rapid development of nanotechnology, the startling properties have been gradually understood leading to the explosions of modern applications. From state-of-art AFM (atomic force microscopy) and computer chips to the nanoparticle-containing sunscreen and stainproof coating in everyday life, nanotechnology is now everywhere.[5,10-11] One main category of nanotechnology applications asks for the fabrication of functional nanostructures, and two approaches,[5] top-down and bottom-up, are often used.

Top-down, like making a sculpture, starts with a large structure, and the excess parts were gradually cut out or trimmed to the final nanofeatures, which is often associated with physical processing such as lithography. Top-down approach is often costly and has limited resolution at surfaces (~ 5 nm). To reach the level of miniaturizations in Feynman's lecture, the precise and cheap bottom-up approach is more promising. Bottom-up approach, inspired by self-assembly in nature, starts by connecting all small building blocks into designed nanostructures. Of all building blocks in bottom-up approach, DNA (deoxyribonucleic acid) stands out for its high programmability and nanometer precision. DNA has been under spotlight since Watson and Crick discovered

the double duplex structure in 1954,[12] and Adenine (A) to Thymine (T), Guanine (G) to Cytosine (C) base-parings and Holliday junction (Fig.1.3) gave rise to DNA nanotechnology pioneered by Ned Seeman in the early 1980s.[13-14] Based on the fundamental concept of Seeman's work, the revolutionary DNA origami was invented by Paul Routhmund in 2006.[15] DNA origami is easy to design and has been widely used to fold DNAs into a myriad of 2D and 3D shapes, such as triangle,[16] smiley face, [16] and even nano Mona Lisa and Gigadalton-scale 3D hierarchical nanostructures.[17-18] Apart from making cool shapes (Fig.1.4), DNA origami templated assembly (DOTA) is widely used to organize functional nanoparticles to produce molecular devices.[19] Of all the nanoparticles assembled, gold nanoparticle is the focus of this dissertation and will be first discussed in section 1.2.

Figure 1.1. Size effects of gold. Top: Bulk gold (Image Credits: Getty image). Bottom: gold nanoparticles of varying sizes (Image Credits: Nikonianman / CC BY-SA 4.0).

Figure 1.2. Photographs of Lycurgus Cup. The dichroic effects upon light irradiation from different angles are due to the gold and silver nanoparticle colorants. © The Trustees of the British Museum.
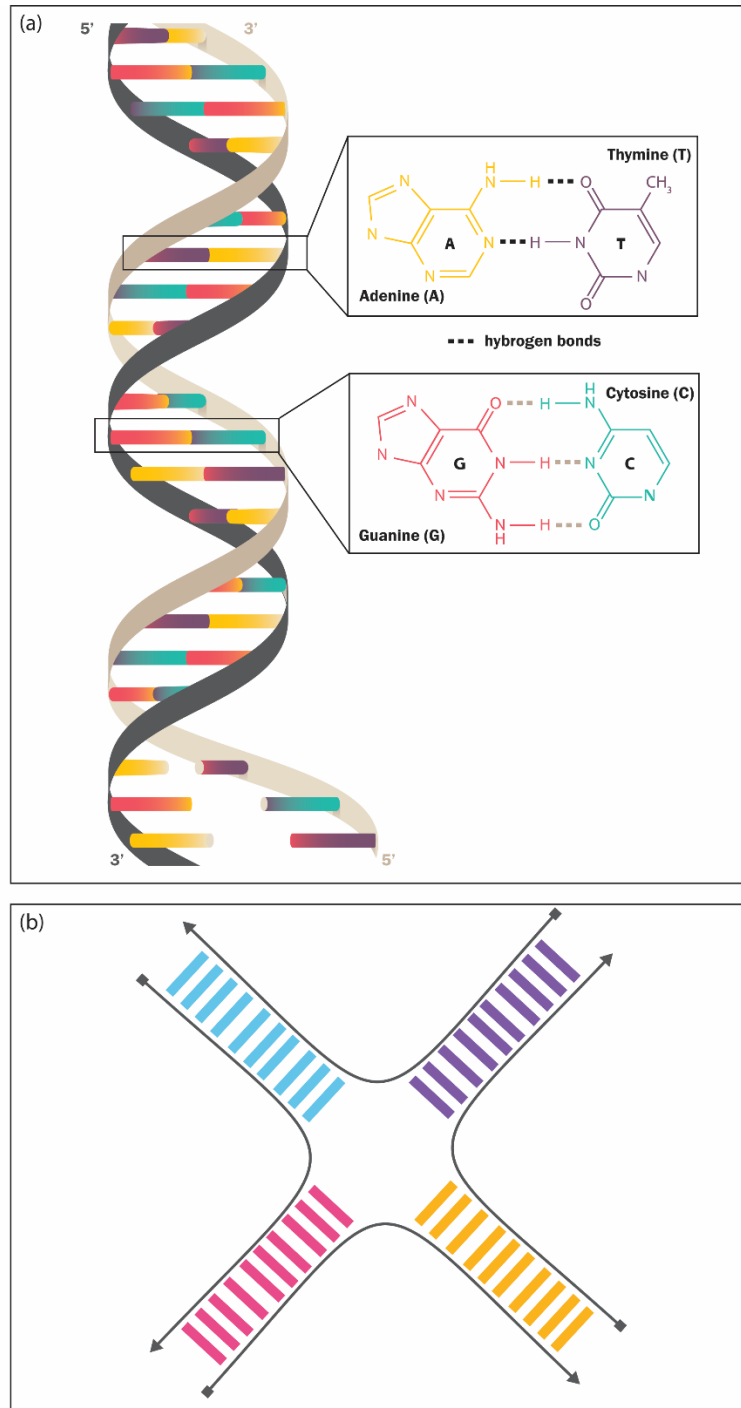
Figure 1.3. Illustrations of DNA.(a) DNA helical duplex and base-paring. (b) Holliday junction. Triangle end: 3'. Square end: 5'. Colored bars: base pairs.
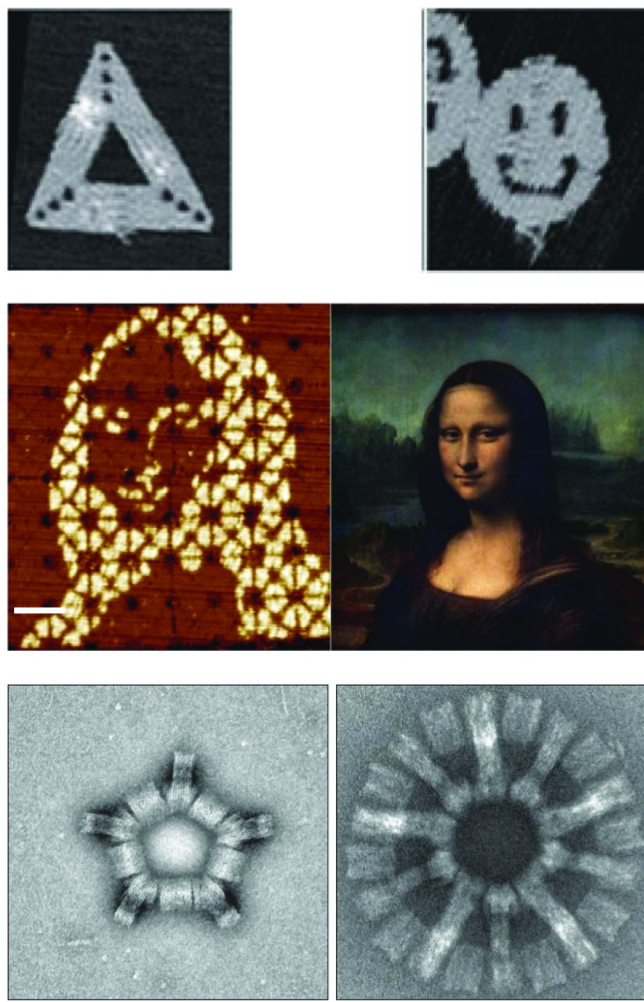
Figure 1.4. Various 2D and 3D shapes made by DNA origami. Top: triangle, smiley face (AFM image size: 165 nm × 165 nm). Reproduced from ref 16. Copyright © 2006, Nature Publishing Group. Middle: nano Mona Lisa (AFM image size: 100 nm × 100 nm). Reproduced from ref 17. Copyright © 2017, Macmillan Publishers Limited, part of Springer Nature. All rights reserved. Bottom: Gigadalton-scale hierarchical 3D nanostructures (scale bar: 50 nm). Reproduced from ref 18. Copyright © 2017, Macmillan Publishers Limited, part of Springer Nature. All rights reserved.

1.2 Gold Nanoparticle and Surface Functionalization

When a gold nanoparticle (AuNP) is irradiated by light (electromagnetic wave), the electric field of light oscillates the free conduction electrons at surface, and such oscillations at surface are localized surface plasmon (LSP, Fig.1.5).[20] The oscillation of free electrons leads to dipole as the positive charges reside one end, the negative charge on the other. When isolated gold nanoparticles are assembled in proximity, LSPs of neighboring gold nanoparticles form strong

plasmonic coupling giving rise to interesting collective effects the isolated nanoparticles don't have,[21] which enables applications such as surface enhanced Raman sensing and plasmon ruler to determine nanoscale distance, just to name a few.[22-23] Plasmonic hybridization theory (Fig.1.6), the analogy of molecular orbital theory, is often used to explain the interactions between LSPs.[24] If charges of the neighboring nanoparticles shift in the same direction (in phase), effective plasmonic coupling takes place producing a lower energy bright mode; if charges are out of phase, a higher energy dark mode is formed with minimal plasmonic coupling. The strength of plasmonic coupling depends largely on two factors: inter-particle gap and electric field polarization direction (Fig.1.7).[25] General trend is the smaller the gap, the stronger the coupling, however, if the gap is below 1 nm, quantum tunneling effects might affect the predicted coupling strength.[26-27] For electric field polarization perpendicular to longitudinal axis, the dark mode is excited, and the resultant signal enhancements is no different from isolated nanoparticles. For polarization along the longitudinal axis of the gold nanoparticle assembly, effective plasmonic coupling gives rise to red-shifted LSP wavelength and enormously amplifies local electric fields (E). The amplified local electric fields are often used to augment the weak Raman scattering termed as surface enhanced Raman scattering (SERS). Enhancement factor (EF) of SERS is proportional to E^4, simulations predicted the highest EF values of over 10^{10} enabling single molecule detections. Isotropic spherical nanoparticles are often used for plasmonic assembly, however, anisotropic pointy gold nanoparticles, such as oblate nanoparticles, often show different plasmonic properties due to lightning-rod effects.[28]

Despite their mesmerizing optical properties, bare (unfunctionalized) gold nanoparticles are unstable in various buffers and have little practical uses.[29] Moreover, bare nanoparticles are incapable of specific interactions that are needed for sensing as well as self-assembly.[30] It is then pertinent to add functionalities to gold nanoparticles with surface modifications to increase stability and enable practical applications. The surface of gold has long been considered chemical inert, if true, the surface modification of gold would be very difficult. Fortunately, though invisible to naked eyes, thiol group (-SH) actively reacts with gold atom on its outmost surface (both bulk and nanoparticle) forming a dense monolayer at room temperature.[31] This finding opened the door to surface functionalization of gold nanoparticles. Thiolated DNA (Fig.1.8) are often used to impart molecular recognition functions to gold nanoparticles. In addition to Au-S bond (~232 kJ/mol), DNA bases also adsorb to the AuNP surfaces with different adsorption energy (A>C>G>T).[32] Even thymine shows ~100 kJ/mol adsorption energy, and adsorbed DNAs could occupy large surface areas and repel the incoming DNA resulting in low DNA coverage.[32] It is noted that with rational sequence design, usually poly-

adenine, one or a few DNA strands without thiol modification can be grafted on gold nanoparticle surfaces.[33-34] As thiolated DNA and gold nanoparticles are both negatively charged, for successful surface functionalization, it is important to reduce the charge repulsion while maintaining the stability of AuNPs.[32] NaCl could reduce charge repulsion. However, abrupt addition of NaCl to the mixture of thiolated DNA and gold nanoparticles would result in irreversible aggregations.[32] To solve this problem, Mirkin et al.[35-36] developed salt-aging method where salt was gradually added. Briefly, the mixture of AuNPs and high excess thiolated DNA is incubated >1 hour, 2 M NaCl solution is added to adjust the final salt concentration of the mixture from 0 M to 0.050 M, then after 1 hour incubation, more salts were added at 0.050 M increments till ≥0.30 M. After the desired final NaCl concentration is met, the mixture is incubated at room temperature overnight. The resultant gold nanoparticle is fully coated with DNA ligands and displays high stability in solutions containing up to 1 M NaCl or 12 mM $MgCl_2$. Before salt is added, a small number of DNAs are added to AuNP surfaces via either DNA base adsorption or Au-S bond after overnight incubation (Fig.1.9). The initially grafted DNAs protect bare AuNP at the cost of surface negative charge increments. Gradual NaCl addition reduces the repulsions between the incoming DNAs and the previously added DNAs, which eventually lead to full DNA surface coverage of AuNPs (Fig.1.9). Salt-aging method usually takes several day to accomplish, to shorten functionalization time, Liu group developed the less time-consuming low-pH assisted method and freezing conjugation method.[33,37] Low-pH method requires long poly-adenine spacers limiting the DNA sequence design, while freezing method produces unstable product for >20 nm AuNPs. As a result, salt-aging method is still the most popular and reliable method to coat AuNPs of varying sizes with thiolated DNAs.
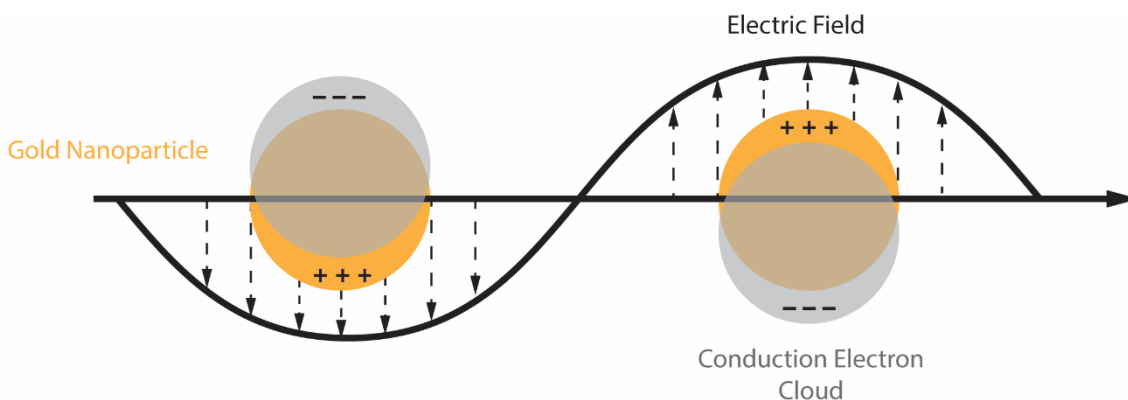
Figure 1.5. Illustration of localized surface plasmon (LSP) of isolated gold nanoparticle.
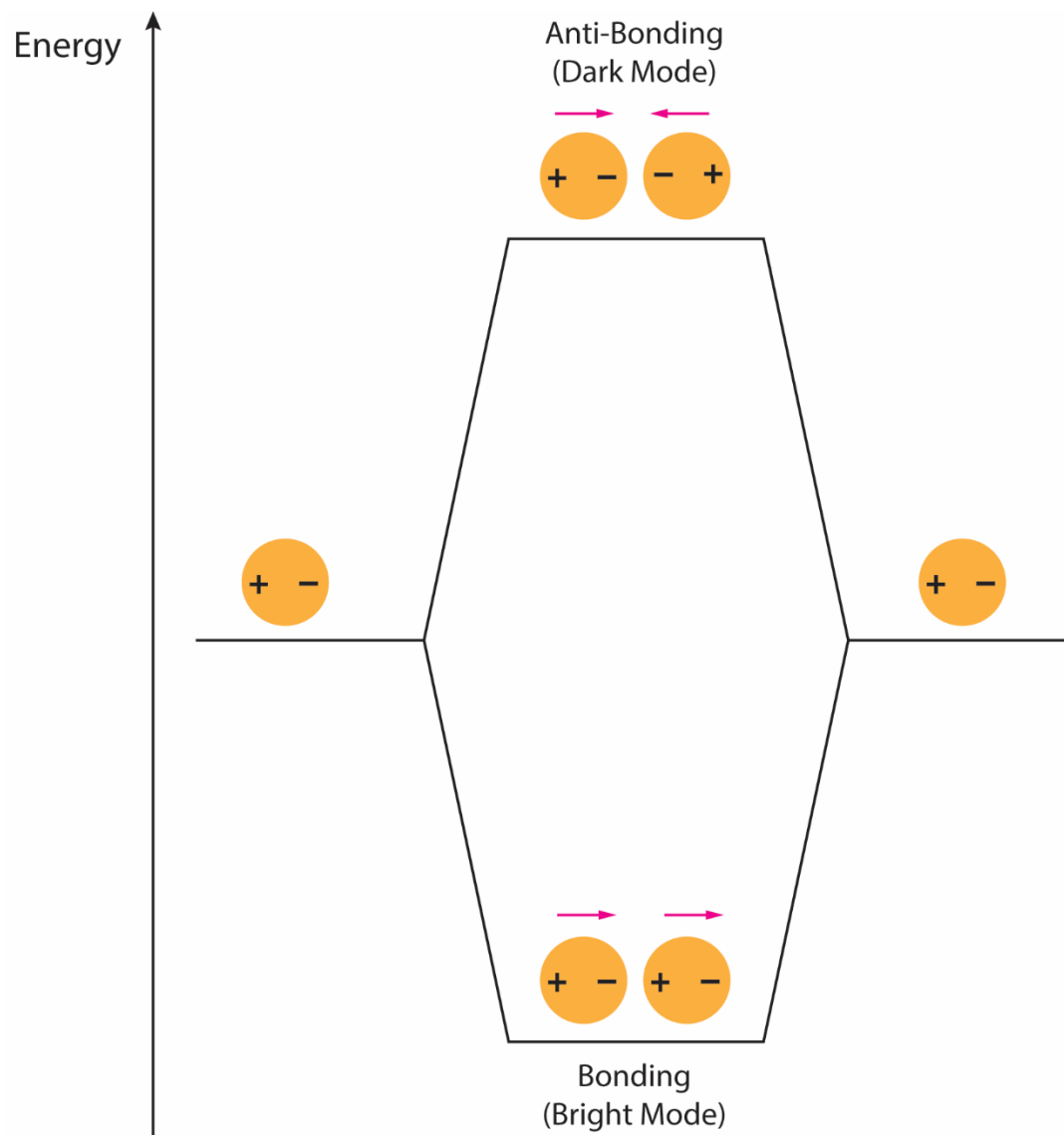
Figure 1.6. Illustration of plasmon hybridization theory. Red arrows: conduction electron oscillation directions.
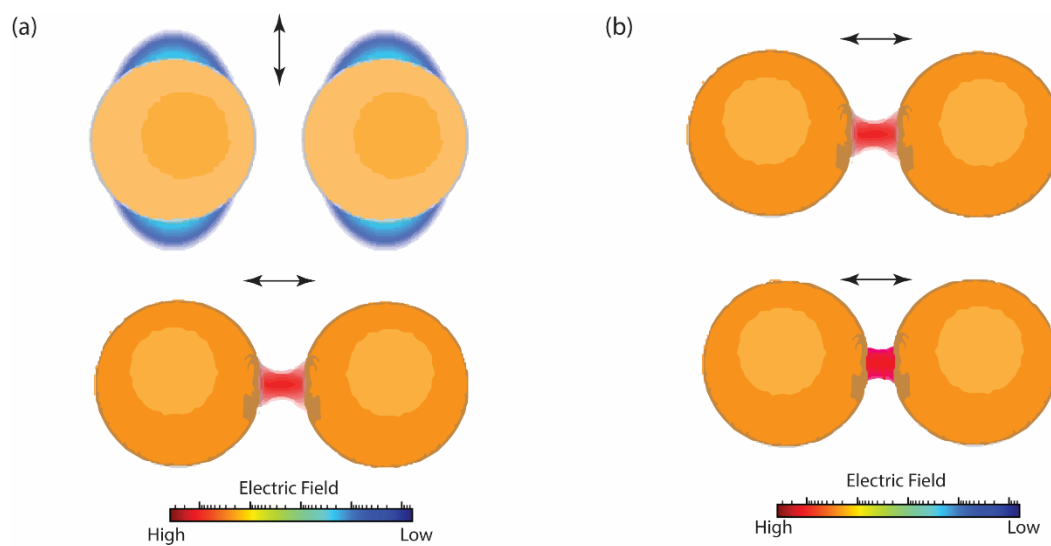
Figure 1.7. Illustrations of plasmonic coupling. (a) Electric polarization dependence. (b) Interparticle gap size dependence. black arrows: electric field polarization direction.
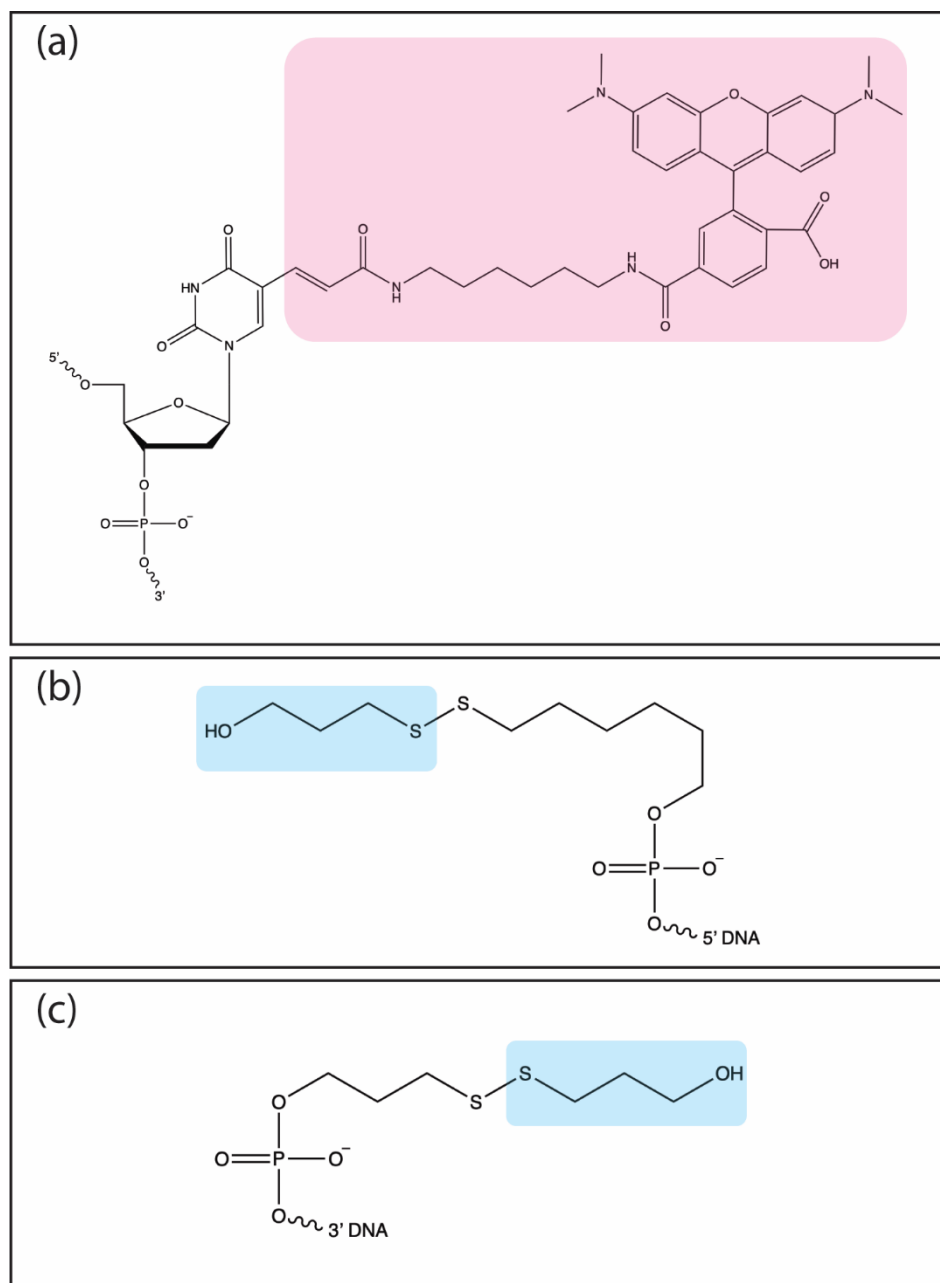
Figure 1.8. Chemical structures of thiolated DNAs. (a) TAMRA (tetramethyl rhodamine) -tagged thiolated DNA on 3' end. Highlighted: TAMRA. (b) 5' end functionalized DNA. Highlighted: protective group. (c) 3' end functionalized DNA. Highlighted: protective group.
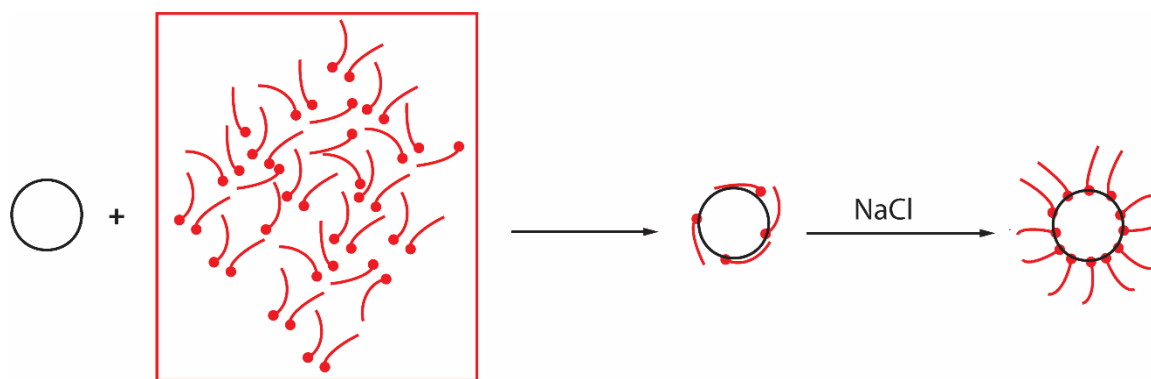
Figure 1.9. Illustration of salt-aging method. Curved line is thiolated DNA, thiol (S) is depicted as the red dot.

1.3   Approaches to Assemble Nanoparticles

When gold nanoparticles are functionalized with DNA, the next goal is naturally to assemble them into pre-defined geometries, known as plasmonic molecules. Often plasmonic assemblies containing >3 nanoparticles showed tantalizing properties simple dimers don't have,[38-40] for instance, Li and colleagues proposed a nanolens, a linear chain of nanoparticles of varying sizes in 2003 (Fig.1.10).[41] According to their simulations, the cascading plasmonic enhancements in nanolens could arguably beat most plasmonic dimer having a much smaller gap in terms of EF. The larger gap not only makes fabrication easier but also enables binding of target molecules the smaller gap doesn't allow. Apart from signal enhancement, other simulations also suggest nanolens supports lossless energy transfer and the generations of second harmonics.[40,42] The nanolens and other plasmonic multimeric nanostructures have attracted a great deal of attentions, however, their complex shapes hindered experimental investigations. Only limited studies in literature reported the "assembly" of nanolens/plasmonic multimers. The laborious top-down approaches such as EBL (electron beam lithography) and SHCL (shrinking-hole colloidal lithography) were used to make nanolenses, however, the low-throughput 2D lithography is challenging to make 3D structures, and the resultant "nanoparticles" often have rough surfaces that severely weaken LSP resonance;[43-46] Bach et al.[47] used electrostatic surface-assembly, a bottom-up approach, to make nanolenses, but only a fraction of the synthesized nanolenses were linear, and this method had restrictions on nanoparticle sizes. Of all bottom-up approaches, DNA-directed assembly stands out owing to its high programmability and nanometer accuracy.[19,48] As shown in Fig.1.11a, Alivisato et al.[49] grafted one DNA ligand to 1.4 nm gold clusters, then the DNA-functionalized gold cluster hybridized with a long complementary DNA

strand to make gold nanoparticle dimers and trimers. Later Alivisato group improved their method and conjugated small nanoparticles (<20 nm) with one or a few thiolated DNA ligand(s), which then hybridized with the other particles functionalized with a complementary ligand(s). They used the direct linkages between DNA ligands to organize nanoparticles into various geometries (Fig.2.11a).[50-52] In 2015, Fan et al.[34] used a poly-adenine sequence to produce monovalent gold nanoparticles (5-20 nm), which can be used to form gold nanoparticle dimers via direct linkage (Fig.2.11a). This approach was extended to produce small gold nanoparticles (<10 nm) with programmable valence bonds in 2020 (Fig.2.11a).[53] In addition, Sleiman group in 2016 used a different approach to position a few DNA strands onto small gold nanoparticle surfaces (5-20 nm) and made some gold nanoparticle multimers by direct linkage (Fig.2.11a).[54] Despite the interesting nanostructures these three groups have made, these surface functionalization methods cannot yet conjugate large nanoparticle (>20 nm) surfaces with well-defined number of strands under high salt conditions that are needed for direct linkage. Moreover, direct linkage has only one DNA duplex between constituent nanoparticles, which remains too flexible to avoid large variations in bond angles and gap sizes. As mentioned earlier, the salt-aging method could produce nanoparticles with high DNA ligand density, which are not limited by nanoparticle size and could resist self-aggregations in high ionic-strength buffer. These two advantages allow gold nanoparticle to be assembled on DNA template whose stability relies on high salt environment. In pre-DNA-origami era, Kiehl et al.[55] functionalized gold nanoparticles with dense DNA ligands and added them to a flexible DNA template in 2002 (Fig.1.11b). The invention of robust DNA origami in 2006 inspired DNA origami templated assembly (DOTA) and profoundly changed the DNA-directed assembly of nanoparticles. The introductions of DNA origami and DOTA will be presented in section 1.4.
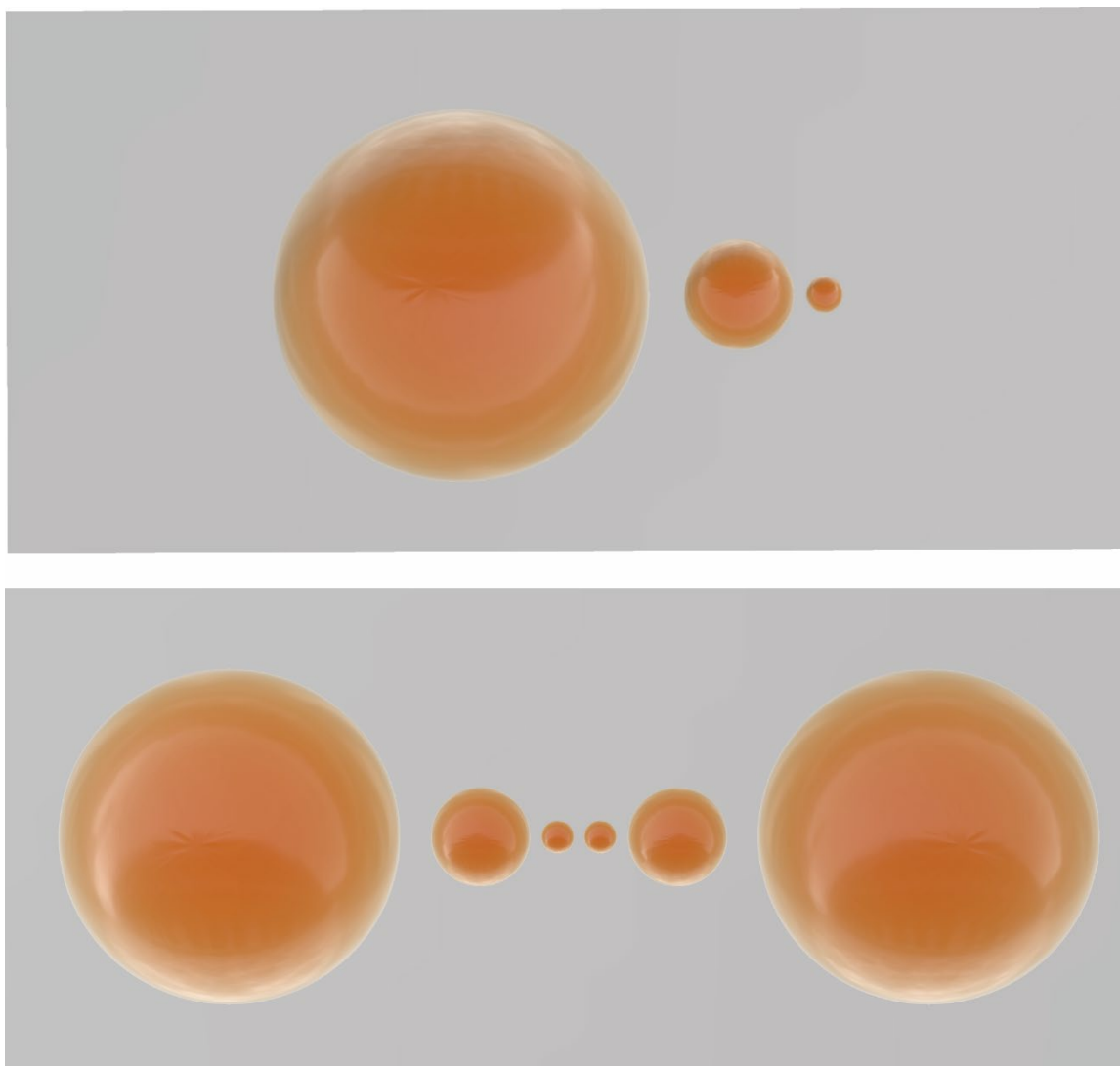
Figure 1.10. Illustrations of proposed nanolenses. Nanolens is a (self-similar) linear chain of nanoparticles of decreasing nanoparticle and gap sizes (from left to right). The special arrangements of nanoparticles enable cascading field enhancements according to simulations.
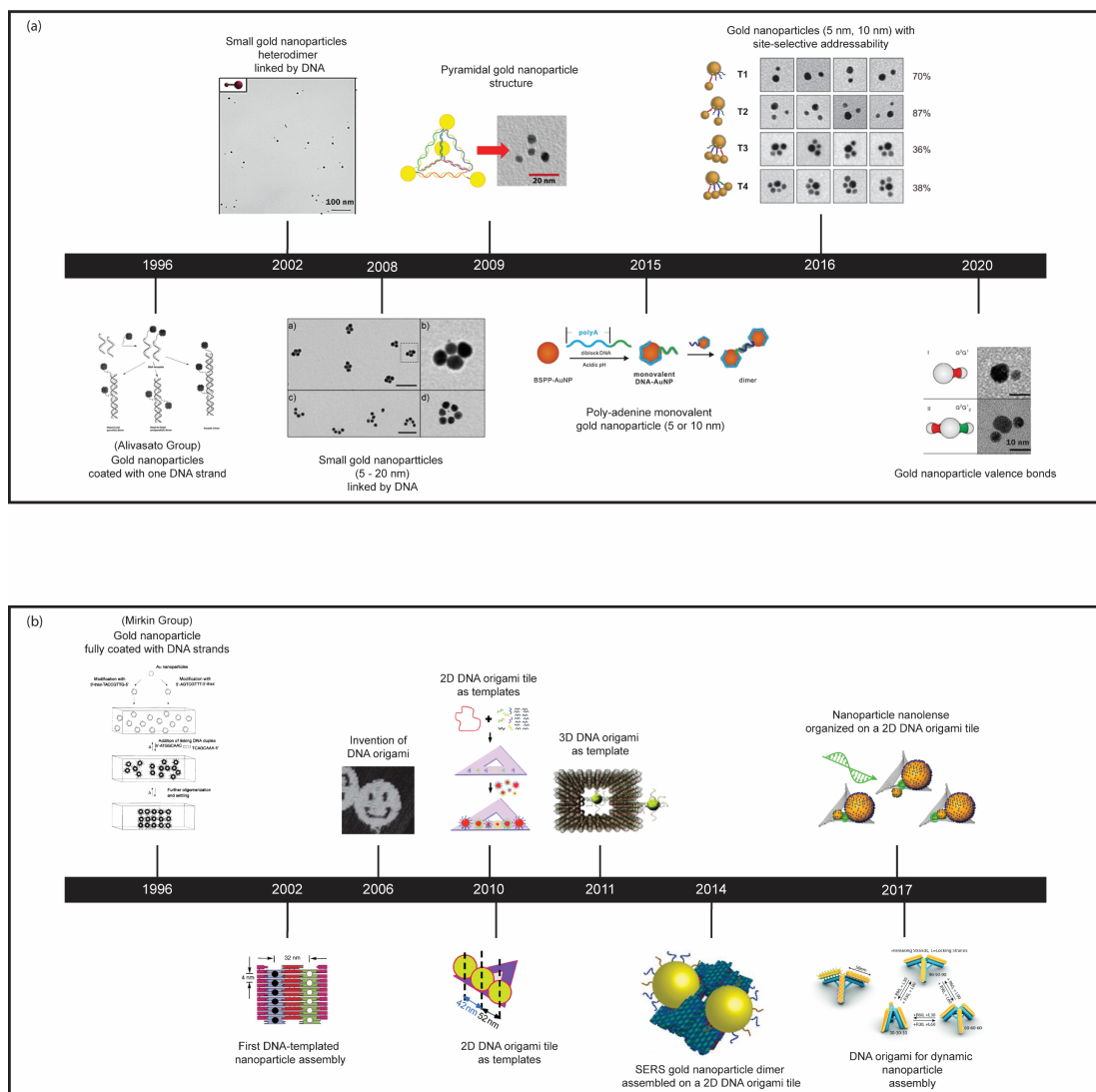
Figure 1.11. Timeline of DNA-directed gold nanoparticle assembly. (a) Development of direct linkage route. Year 1996: Reproduced from ref 49. Copyright © 1996, Nature Publishing Group. Year 2002: Reproduced from ref 49. Copyright © 2002, Nature Publishing Group. Year 2008: Reproduced from ref 51. Copyright © 2008, American Chemical Society. Year 2009: Reproduced from ref 52. Copyright © 2009, American Chemical Society. Year 2015: Reproduced from ref 34. Copyright © 2015, The Author(s). Year 2016: Reproduced from ref 54. Copyright © 2016, Nature Publishing Group. Year 2020: Reproduced from ref 53. Copyright © 2020, The Author(s), under exclusive licence to Springer Nature Limited. (b) Development of DNA origami templated assembly route. Year 1996: Reproduced from ref 35. Copyright © 1996, Nature Publishing Group. Year 2002. Reproduced from ref 35. Copyright © 2002, American Chemical Society. Year 2006: Reproduced from ref 16. Copyright © 2006, Nature Publishing Group. Year 2010: Reproduced from ref 56 (top) and ref 57 (bottom). Copyright © 2010, American Chemical Society. Copyright © 2010 WILEY-VCH Verlag GmbH & Co. KGaA, Weinheim. Year 2011: Reproduced from ref 58. Copyright © 2011 WILEY-VCH Verlag GmbH & Co. KGaA, Weinheim. Year 2014: Reproduced from ref 59. Copyright © 2014, Nature Publishing Group, a division of Macmillan Publishers Limited. All Rights Reserved. Year 2017: Reproduced from ref 60 (top) and ref 61(bottom). Copyright © 2017, American Chemical Society (top). Copyright © 2017, American Chemical Society (bottom).

1.4 DNA Origami Templated Assembly

The design of DNA origami starts by routing a single strand DNA (scaffold) into the shapes of interest, then multiple complementary short DNAs (staple) are added to bind with scaffold forming double helices.[15] The adjacent double helices are connected to each other by multiple anti-parallel double crossovers. Unlike other DNA nanostructures, scaffold DNA functions as a backbone and greatly enhances the overall rigidity of DNA origami. To fold DNA origami, the scaffold is mixed with excess staples and then slowly annealed in salt, usually $MgCl_2$ (Fig.1.12), 2D single-layer DNA origami can be folded with high yield, Moreover, by controlling the positions of crossovers, multilayered 3D DNA origami be readily designed. However, folding of 3D DNA origami often requires extended annealing time with lower yield because of the complexity and high density of crossovers.[15] To characterize overall folding yield of DNA origami, agarose gel electrophoresis (Fig.1.13) is widely used in which the negatively charged DNA origami nanostructures migrate to the anode (positive end) under an applied electric field.[19] The charge-to-mass ratio determines the electrophoretic mobilities of species in gel, meaning the short staples move much faster than the folded origami, and the misfolded structures often produce smear.

One key merit of DNA origami is that the position of each staple is defined by the sequence of scaffold, making modifications of staples easy. The accurate position of staples allows precise and selective placements of gold nanoparticles.[19] The staples can be extended to have a single strand overhang or sticky end, and the staple extensions can be used to anchor the DNA-functionalized gold nanoparticles that have the complementary sequence, which is the cornerstone of DNA origami templated assembly (DOTA). 2D DNA origami tiles have been widely used to organize gold/silver nanoparticles of varying sizes since 2010 (Fig.1.11b).[56-58] In addition, a 40 nm-homo-dimer assembled on a 2D DNA origami tile showed strong surface enhancement Raman scattering (2014).[59] 3D DNA origami nanostructures were also employed to arrange nanoparticles (2011) and were recently extended for dynamic gold nanoparticle assembly in 2017.[60-61] Except for the 3D DNA origami used in Yan's work,[60] flat surfaces of the DNA origamis are mostly used to bind the nanoparticles. Using this binding strategy, same- or similar-sized nanoparticles could be organized on the surface of DNA origami templates, and homo-dimers still take up a lion's share of assembled nanostructures using DOTA.[62-63] To make nanolenses, Ding et al.[56] and Bald et al.[58] used two different 2D DNA origami tiles to assemble multiple gold nanoparticles of varying sizes (Fig.1.14, Fig.1.11b), but their resultant nanolenses produced less-than-predicted plasmonic coupling and SERS enhancement, which they ascribed to the misalignments of the assembled

nanoparticles. The capture strands of their tiles only tethered nanoparticles near their south poles (Fig.2.4), which resulted in poor confinements of bound nanoparticles. The poor nanoparticle confinements eventually led to large deviation from designed geometries. Despite the significant potentials of DOTA, the current binding strategy is incapable of precisely arranging >2 nanoparticles with large size differences. To unleash the full potentials of DOTA in the self-assembly of more complex plasmonic structures, this dissertation is dedicated to new binding strategies and approaches to make plasmonic hetero-trimeric molecules with defined bond angles and gap sizes.

The structure of this dissertation is as follows. Chapter 2 is the main chapter that includes the design of our new assembly approach and systematic investigations of plasmonic trimeric molecules, which entail detailed syntheses, structural and plasmonic characterizations and simulations. We take one step further to explore another binding strategy in Chapter 3 together with simulations. The findings in Chapters 2 and 3 broaden the horizon of all existing binding strategies of DNA origami templated assembly and establish new concepts in DNA-directed assembly.
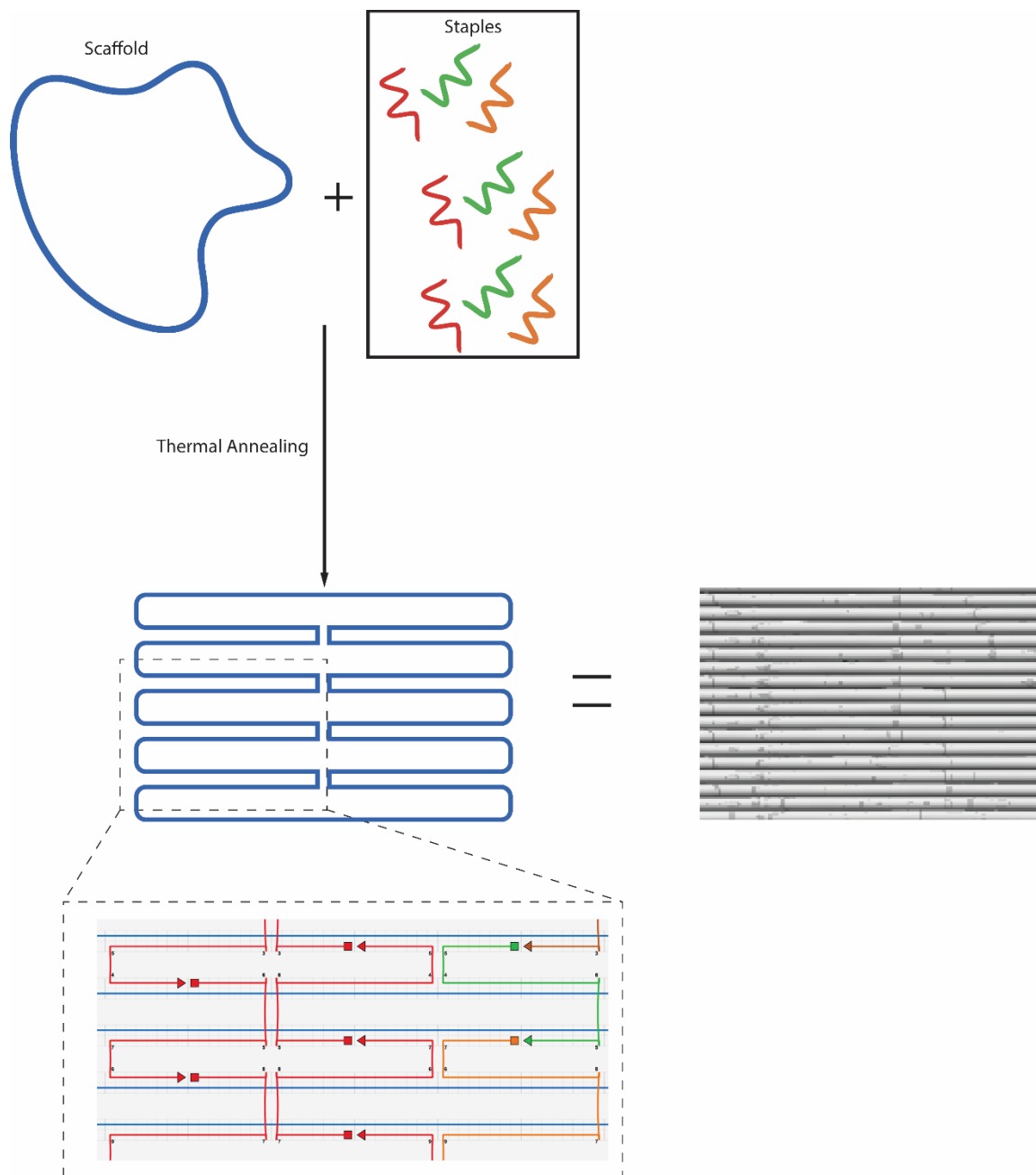
Figure 1.12. Illustrations of DNA origami design and folding.
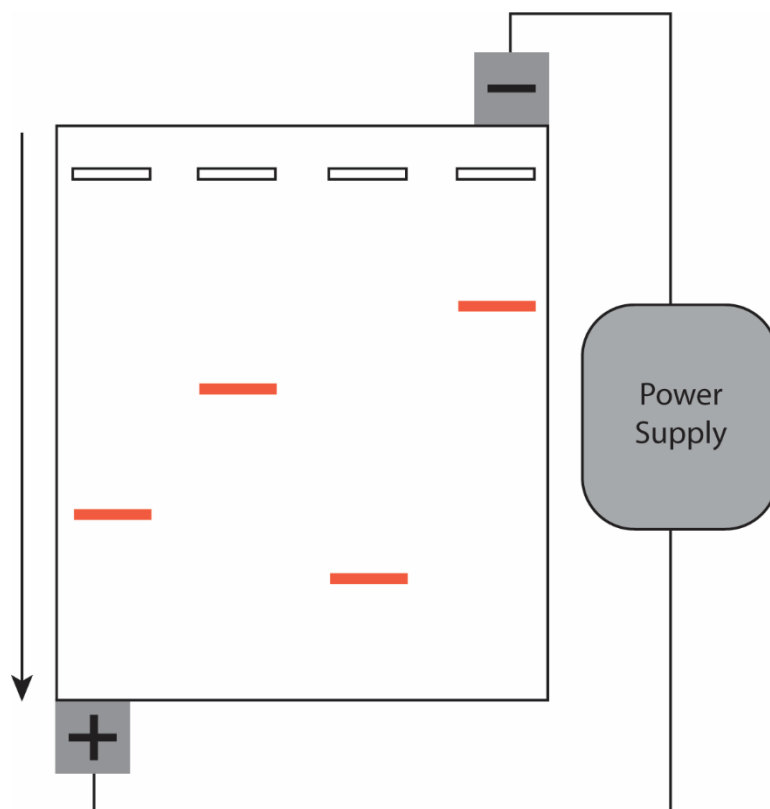
Figure 1.13. Schematic of agarose gel electrophoresis. Red bands: Nanostructures of different electrophoretic mobilities. Black arrow: Migration direction. Small white squares on top: Loading pockets (wells).
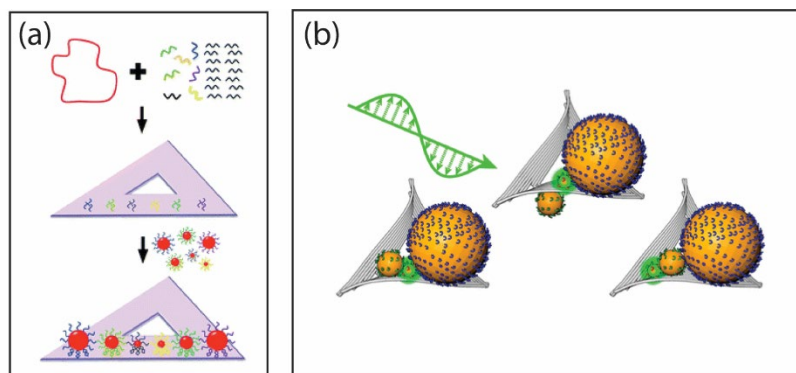
Figure 1.14. Schematic of nanolenses assembled by DOTA. (a) Ding's nanolens. Reproduced from ref 56. Copyright © 2010, American Chemical Society. (b) Bald's nanolenses. Reproduced from ref 60. Copyright © 2017, American Chemical Society.

Reference

(1) Feynman, R. P. There's Plenty of Room at the Bottom. *Engineering and Science* **1960**,23, 22-36.

(2) Hulla, J.; Sahu, S.; Hayes, A. Nanotechnology:History and future. *Human & Experimental Toxicology* **2015**, *34* (12), 1318-1321.

(3) Bayda, S.; Adeel, M.; Tuccinardi, T.; Cordani, M.; Rizzolio, F. The History of Nanoscience and Nanotechnology: From Chemical-Physical Applications to Nanomedicine. *Molecules* **2019**, *25* (1).

(4) Toumey, C. From nano machines to Nobel prizes. *Nature Nanotechnology* **2017**, *12* (1), 1-1.

(5) Cademartiri, L.; Ozin, G. A.; Lehn, J. M. *Concepts of Nanochemistry*; Wiley, 2009.

(6) Roduner, E. *Nanoscopic Materials: Size-Dependent Phenomena and Growth Principles*; Royal Society of Chemistry, 2015.

(7) Wu, X.; Zhang, C.; Goldberg, P.; Cohen, D.; Pan, Y.; Arpin, T.; Bar-Yosef, O. Early Pottery at 20,000 Years Ago in Xianrendong Cave, China. *Science* **2012**, *336* (6089), 1696-1700.

(8) Johnson-McDaniel, D.; Barrett, C. A.; Sharafi, A.; Salguero, T. T. Nanoscience of an Ancient Pigment. *Journal of the American Chemical Society* **2013**, *135* (5), 1677-1679.

(9) Freestone, I.; Meeks, N.; Sax, M.; Higgitt, C. The Lycurgus Cup — A Roman nanotechnology. *Gold Bulletin* **2007**, *40* (4), 270-277.

(10) Müller, D. J.; Dufrêne, Y. F. Atomic force microscopy as a multifunctional molecular toolbox in nanobiotechnology. *Nature Nanotechnology* **2008**, *3* (5), 261-269.

(11) Nasrollahzadeh, M.; Sajadi, S. M.; Sajjadi, M.; Issaabadi, Z. Chapter 4 - Applications of Nanotechnology in Daily Life. In *Interface Science and Technology*, Nasrollahzadeh, M., Sajadi, S. M., Sajjadi, M., Issaabadi, Z., Atarod, M. Eds.; Vol. 28; Elsevier, 2019; pp 113-143.

(12) Watson, J. D.; Crick, F. H. C. Molecular Structure of Nucleic Acids: A Structure for Deoxyribose Nucleic Acid. *Nature* **1953**, *171* (4356), 737-738.

(13) Holliday, R. A mechanism for gene conversion in fungi. *Genet Res* **2007**, *89* (5-6), 285-307.

(14) Pelesko, J. A. *Self Assembly: The Science of Things That Put Themselves Together*; CRC Press LLC, 2017.

(15) Rothemund, P. W. K. Folding DNA to create nanoscale shapes and patterns. *Nature* **2006**, *440* (7082), 297-302.

(16) Rothemund, P. Folding DNA to create nanoscale shapes and patterns. *Nature* **2006**, *440* (7082), 297-302.

(17) Tikhomirov, G.; Petersen, P.; Qian, L. Fractal assembly of micrometre-scale DNA origami arrays with arbitrary patterns. *Nature* **2017**, *552* (7683), 67-71.

(18) Wagenbauer, K.; Sigl, C.; Dietz, H. Gigadalton-scale shape-programmable DNA assemblies. *Nature* **2017**, *552* (7683), 78-83, Article.

(19) Endo, M. *DNA Origami: Structures, Technology, and Applications | Wiley*.

(20) Mayer, K. M.; Hafner, J. H. Localized surface plasmon resonance sensors. *Chemical Reviews* **2011**, *111* (6), 3828-3857.

(21) Jain, P. K.; El-Sayed, M. A. Plasmonic coupling in noble metal nanostructures. *Chemical Physics Letters* **2010**, *487* (4-6), 153-164.

(22) Stiles, P. L.; Dieringer, J. A.; Shah, N. C.; Van Duyne, R. P. Surface-Enhanced Raman Spectroscopy. *Annual Review of Analytical Chemistry* **2008**, *1* (1), 601-626.

(23) Unser, S.; Bruzas, I.; He, J.; Sagle, L. Localized Surface Plasmon Resonance Biosensing: Current Challenges and Approaches. *Sensors* **2015**, *15* (7), 15684-15716.

(24) Prodan, E.; Radloff, C.; Halas, N. J.; Nordlander, P. A Hybridization Model for the Plasmon Response of Complex Nanostructures. *Science* **2003**, *302* (5644), 419-422.

(25) Le Ru, E.; Etchegoin, P. Quantifying SERS enhancements. *Mrs Bulletin* **2013**, *38* (8), 631-640.

(26) Savage, K. J.; Hawkeye, M. M.; Esteban, R.; Borisov, A. G.; Aizpurua, J.; Baumberg, J. J. Revealing the quantum regime in tunnelling plasmonics. *Nature* **2012**, *491* (7425), 574-577.

(27) Zuloaga, J.; Prodan, E.; Nordlander, P. Quantum Description of the Plasmon Resonances of a Nanoparticle Dimer. *Nano Letters* **2009**, *9* (2), 887-891.

(28) Liao, P. F.; Wokaun, A. Lightning rod effect in surface enhanced Raman scattering. *The Journal of Chemical Physics* **1982**, *76* (1), 751-752.

(29) Wang, A.; Ng, H. P.; Xu, Y.; Li, Y.; Zheng, Y.; Yu, J.; Han, F.; Peng, F.; Fu, L. Gold Nanoparticles: Synthesis, Stability Test, and Application for the Rice Growth. *Journal of Nanomaterials* **2014**, *2014*, 451232.

(30) Dykman, L.; Khlebtsov, N. *Gold Nanoparticles in Biomedical Applications*; CRC Press, 2017.

(31) Pensa, E.; Cortés, E.; Corthey, G.; Carro, P.; Vericat, C.; Fonticelli, M. H.; Benítez, G.; Rubert, A. A.; Salvarezza, R. C. The chemistry of the sulfur-gold interface: In search of a unified model. *Accounts of Chemical Research* **2012**, *45* (8), 1183-1192.

(32) Liu, B.; Liu, J. Methods for preparing DNA-functionalized gold nanoparticles, a key reagent of bioanalytical chemistry. *Anal. Methods* **2017**, *9* (18), 2633-2643.

(33) Zhang, X.; Servos, M. R.; Liu, J. Instantaneous and quantitative functionalization of gold nanoparticles with thiolated DNA using a pH-assisted and surfactant-free route. *Journal of the American Chemical Society* **2012**, *134* (17), 7266-7269.

(34) Yao, G.; Pei, H.; Li, J.; Zhao, Y.; Zhu, D.; Zhang, Y.; Lin, Y.; Huang, Q.; Fan, C. Clicking DNA to gold nanoparticles: poly-adenine-mediated formation of monovalent DNA-gold nanoparticle conjugates with nearly quantitative yield. *NPG Asia Materials* **2015**, *7* (1), e159-e159.

(35) Mirkin, C. A.; Letsinger, R. L.; Mucic, R. C.; Storhoff, J. J. A DNA-based method for rationally assembling nanoparticles into macroscopic materials. *Nature* **1996**, *382* (6592), 607-609.

(36) Hurst, S.; Lytton-Jean, A.; Mirkin, C. Maximizing DNA loading on a range of gold nanoparticle sizes. *Analytical Chemistry* **2006**, *78* (24), 8313-8318.

(37) Liu, B.; Liu, J. Freezing Directed Construction of Bio/Nano Interfaces: Reagentless Conjugation, Denser Spherical Nucleic Acids, and Better Nanoflares. *Journal of the American Chemical Society* **2017**, *139* (28), 9471-9474.

(38) Brandl, D. W.; Mirin, N. A.; Nordlander, P. Plasmon modes of nanosphere trimers and quadrumers. *Journal of Physical Chemistry B* **2006**, *110* (25), 12302-12310.

(39) Li, Z. P.; Shegai, T.; Haran, G.; Xu, H. X. Multiple-Particle Nanoantennas for Enormous Enhancement and Polarization Control of Light Emission. *Acs Nano* **2009**, *3* (3), 637-642.

(40) Roller, E.-M.; Besteiro, L. V.; Pupp, C.; Khorashad, L. K.; Govorov, A. O.; Liedl, T. Hotspot-mediated non-dissipative and ultrafast plasmon passage. *Nature Physics* **2017**, *13* (8), 761-765.

(41) Li, K.; Stockman, M.; Bergman, D. Self-similar chain of metal nanospheres as an efficient nanolens. *Physical Review Letters* **2003**, *91* (22), 227402.

(42) Li, K.; Stockman, M. I.; Bergman, D. J. Enhanced second harmonic generation in a self-similar chain of metal nanospheres. *Physical Review B - Condensed Matter and Materials Physics* **2005**, *72* (15), 1-4.

(43) Kravets, V.; Zorinyants, G.; Burrows, C.; Schedin, F.; Casiraghi, C.; Klar, P.; Geim, A.; Barnes, W.; Grigorenko, A. Cascaded Optical Field Enhancement in Composite Plasmonic Nanostructures. *Physical review letters* **2010**, *105*, 246806.

(44) Syrenova, S.; Wadell, C.; Langhammer, C. Shrinking-Hole Colloidal Lithography: Self-Aligned Nanofabrication of Complex Plasmonic Nanoantennas. *Nano Letters* **2014**, *14* (5), 2655-2663.

(45) Höppener, C.; Lapin, Z. J.; Bharadwaj, P.; Novotny, L. Self-Similar Gold-Nanoparticle Antennas for a Cascaded Enhancement of the Optical Field. *Physical Review Letters* **2012**, *109* (1), 017402.

(46) Tinguely, J.-C.; Sow, I.; Leiner, C.; Grand, J.; Hohenau, A.; Felidj, N.; Aubard, J.; Krenn, J. R. Gold Nanoparticles for Plasmonic Biosensing: The Role of Metal Crystallinity and Nanoscale Roughness. *BioNanoScience* **2011**, *1* (4), 128-135.

(47) Lloyd, J.; Ng, S.; Liu, A.; Zhu, Y.; Chao, W.; Coenen, T.; Etheridge, J.; Gomez, D.; Bach, U. Plasmonic Nanolenses: Electrostatic Self-Assembly of Hierarchical Nanoparticle Trimers and Their Response to Optical and Electron Beam Stimuli. *ACS Nano* **2017**, *11* (2), 1604-1612.

(48) Seeman, N. C. *Structural DNA Nanotechnology*; Cambridge University Press, 2015.

(49) Alivisatos, A. P.; Johnsson, K. P.; Peng, X. G.; Wilson, T. E.; Loweth, C. J.; Bruchez, M. P.; Schultz, P. G. Organization of 'nanocrystal molecules' using DNA. *Nature* **1996**, *382* (6592), 609-611.

(50) Zanchet, D.; Micheel, C. M.; Parak, W. J.; Gerion, D.; Williams, S. C.; Alivisatos, A. P. Electrophoretic and Structural Studies of DNA-Directed Au Nanoparticle Groupings. *The Journal of Physical Chemistry B* **2002**, *106* (45), 11758-11763.

(51) Claridge, S. A.; Liang, H. W.; Basu, S. R.; Fréchet, J. M. J.; Alivisatos, A. P. Isolation of Discrete Nanoparticle−DNA Conjugates for Plasmonic Applications. *Nano Letters* **2008**, *8* (4), 1202-1206.

(52) Mastroianni, A. J.; Claridge, S. A.; Alivisatos, A. P. Pyramidal and Chiral Groupings of Gold Nanocrystals Assembled Using DNA Scaffolds. *Journal of the American Chemical Society* **2009**, *131* (24), 8455-8459.

(53) Yao, G.; Li, J.; Li, Q.; Chen, X.; Liu, X.; Wang, F.; Qu, Z.; Ge, Z.; Narayanan, R. P.; Williams, D.; et al. Programming nanoparticle valence bonds with single-stranded DNA encoders. *Nature Materials* **2020**, *19* (7), 781-788.

(54) Edwardson, T.; Lau, K.; Bousmail, D.; Serpell, C.; Sleiman, H. Transfer of molecular recognition information from DNA nanostructures to gold nanoparticles. *Nature Chemistry* **2016**, *8* (2), 162-170.

(55) Pinto, Y. Y.; Le, J. D.; Seeman, N. C.; Musier-Forsyth, K.; Taton, T. A.; Kiehl, R. A. Sequence-Encoded Self-Assembly of Multiple-Nanocomponent Arrays by 2D DNA Scaffolding. *Nano Letters* **2005**, *5* (12), 2399-2402.

(56) Ding, B.; Deng, Z.; Yan, H.; Cabrini, S.; Zuckermann, R.; Bokor, J. Gold Nanoparticle Self-Similar Chain Structure Organized by DNA Origami. *Journal of the American Chemical Society* **2010**, *132* (10), 3248-3249, Article.

(57) Pal, S.; Deng, Z.; Ding, B.; Yan, H.; Liu, Y. DNA-origami-directed self-assembly of discrete silver-nanoparticle architectures. *Angew Chem Int Ed Engl* **2010**, *49* (15), 2700-2704.

(58) Heck, C.; Prinz, J.; Dathe, A.; Merk, V.; Stranik, O.; Fritzsche, W.; Kneipp, J.; Bald, I. Gold Nanolenses Self-Assembled by DNA Origami. *ACS Photonics* **2017**, *4* (5), 1123-1130.

(59) Thacker, V. V.; Herrmann, L. O.; Sigle, D. O.; Zhang, T.; Liedl, T.; Baumberg, J. J.; Keyser, U. F. DNA origami based assembly of gold nanoparticle dimers for surface-enhanced Raman scattering. *Nature Communications* **2014**, *5*, 3448-3448.

(60) Zhao, Z.; Jacovetty, E.; Liu, Y.; Yan, H. Encapsulation of Gold Nanoparticles in a DNA Origami Cage. *Angewandte Chemie-International Edition* **2011**, *50* (9), 2041-2044.

(61) Zhan, P.; Dutta, P. K.; Wang, P.; Song, G.; Dai, M.; Zhao, S.-X.; Wang, Z.-G.; Yin, P.; Zhang, W.; Ding, B.; et al. Reconfigurable Three-Dimensional Gold Nanorod Plasmonic Nanostructures Organized on DNA Origami Tripod. *ACS Nano* **2017**, *11* (2), 1172-1179.

(62) Liu, N.; Liedl, T. DNA-Assembled Advanced Plasmonic Architectures. *Chemical Reviews* **2018**, *118* (6), 3032-3053.

(63) Kuzyk, A.; Jungmann, R.; Acuna, G. P.; Liu, N. DNA Origami Route for Nanophotonics. *ACS Photonics* **2018**, *5* (4), 1151-1163.

Chapter 2: Nanoparticle Heterotrimers Organized by 3D
DNA Origami Cage

2.1 Introduction

Within an assembly of metal nanoparticles, the surface plasmons, i.e., collective charge oscillations, of these nanoparticles can interact, mix, and hybridize in a fashion that is analogous to electronic wave functions in atomic and molecular orbitals.[1-3] Such plasmonic molecules have enabled interesting collective phenomena that are not available with isolated nanoparticles,[4] such as strong local field enhancement,[5] Fano resonances,[6] magnetic resonances,[7] and chiral optical properties.[8] These phenomena lead to numerous applications, such as biomolecular sensing,[9] surface-enhanced Raman and fluorescence spectroscopies,[10-13] and energy harvesting.[14] A prerequisite of many of these properties is the precise arrangement of these nanoparticles in 3D.[15-16] Often, nanoparticles of different sizes need to be incorporated into the same "molecule" for interesting plasmonic effects such as nano lensing.[17] Moreover, these assemblies need to have precisely controlled gap sizes, tailored valances, and predefined bond angles.[18] While organic synthesis has enabled the construction of highly sophisticated natural molecules, the synthesis of artificial plasmonic molecules with complex 3D shapes remains in its infancy.

The arguably most promising route to make such complex plasmonic molecules is DNA-directed assembly that used base-pairing to organize DNA functionalized nanoparticles.[19] A key strategy for DNA-directed assembly is direct linkage in which the DNA ligands of constituent nanoparticles hybridize with each other, linking these nanoparticles into assemblies.[20-22] Owing to the development of surface functionalization and purification techniques, a small (≤20 nm) single nanoparticle can be functionalized with controlled number of DNA strands, which enabled direct linkage to produce assemblies with designed valences and shapes (Fig.1.11a, Fig.2.1).However, as this strategy relies on single DNA duplexes to connect constituent small nanoparticles, the flexibility of these duplexes leads to large variations in bond angle and gap sizes. Consequently, the resulting structures often lack strong plasmonic coupling. The other approach is to bind nanoparticles fully coated with DNA ligands to addressable sites on the surface of self-assembled DNA templates, often 2D origami tiles (Fig.1.11b, Fig.2.2). This approach can be extended to large nanoparticles (Fig.1.11b) and is widely used to organize nanoparticles having the same or similar sizes.[23] However, this approach works poorly on organizing arrange nanoparticles of varying sizes into assemblies with defined bond angles and gap sizes, and the larger the size differences, the greater the variations.[24-25] Another limitation of this approach is the lack of tight nanoparticle confinements. In this approach, nanoparticle confinements rely exclusively on the capture strands projecting from the template surfaces, and all capture strands are bound near a single point of the nanoparticle. With such

near single-point-tethering, the motions of bound nanoparticles remain significant (Fig.2.3).[26] In addition, the single-layer 2D DNA origami tiles, the most popular templates, have notable conformational fluctuations that may lead to variability in the geometry of the plasmonic molecules assembles on these templates (Fig.A.1).[27] Consequently, even a simple heterotrimer that comprises two large particles flanking a small one in a collinear configuration, the equivalent of CO_2, is too challenging to form using these two approaches.

To make plasmonic molecules with defined bond angles and gap sizes, we developed a new nanoparticle assembly strategy (Fig.2.4) called docking to DNA origami cage (D-DOC). We used a rigid 3D DNA origami cage (Fig.A.1) to tightly confine bound nanoparticles in 3D and make the gap size and bond angle to be independent of nanoparticle sizes. Instead of confining a nanoparticle using a single or a few closely-spaced tethering points as in conventional DNA origami templated assembly, D-DOC uses the cage to administer tethering points across nanoparticle surfaces (Fig.2.3) to achieve a tighter confinement of the bound nanoparticles and reduce the dependence of gap/bond angle on the size and shape of the nanoparticles. The bound terminal nanoparticles may be further stabilized by the shape complementarity with the cage openings as well as physical contacts between ligand shells on the nanoparticles. We hypothesize all these interactions would work synergistically to tightly confine constituent nanoparticles in 3D and maintain designed geometry regardless of the nanoparticle sizes. Our model system to test this strategy is a linear heterotrimer consisting of a central small nanoparticle and two large terminal nanoparticles, which has not been successfully made to the best of our knowledge.

Besides the superior nanoparticle confinements, our cage has another unique merit. The capture strands on the flat surfaces of DNA templates are parallel to each other, if one poly-dispersed nanoparticle is tethered to a binding site, the functionality of the neighboring sites will be impaired or even deactivated (Fig. 2.5). On the contrary, the outside and inside capture strands of our cage are orthogonal to each other. The orthogonal design of capture strands allows ever-accessible binding sites that minimize the impacts of poly-dispersed nanoparticles.

Our cage-mediated approach shows strong nanoparticle confinements by holding all three constituent "atoms" of different sizes at consistent gap distance in a collinear fashion. We first made symmetric 30 nm-10 nm-30 nm, an analogue of CO_2, and 50 nm-10 nm-50 nm trimers respectively, then explored the synthesis of an asymmetric 30 nm-10 nm-50 nm trimer. Our assembled trimers can effectively serve as a plasmonic nanolens that focuses

intense electric fields onto the surface of the central nanoparticle.[28] Our initial efforts focused on linear trimers that consists of only gold nanoparticles (AuNPs), but we expect that it can be readily extended to a host of plasmonic molecules that have more nanomaterial constituents,[29] such as a hybrid of gold nanoparticle and quantum dot, and plasmonic molecules with different valences and bond angles, such as analogues of NH_3 and CH_4. Hence, our approach may represent a paradigm shift in the study of plasmonic molecules by making a class of molecules with precise 3D arrangements synthetically accessible.[4]
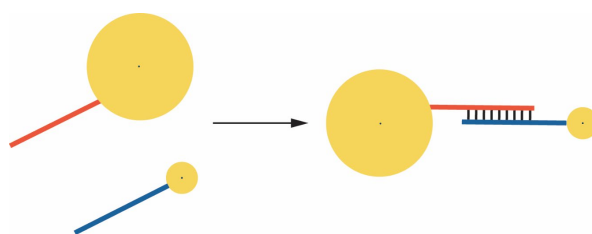
Figure 2.1. Schematic of direct linkage strategy. Yellow circles are nanoparticles. Red and blue lines are DNA ligands of small and large nanoparticles, respectively
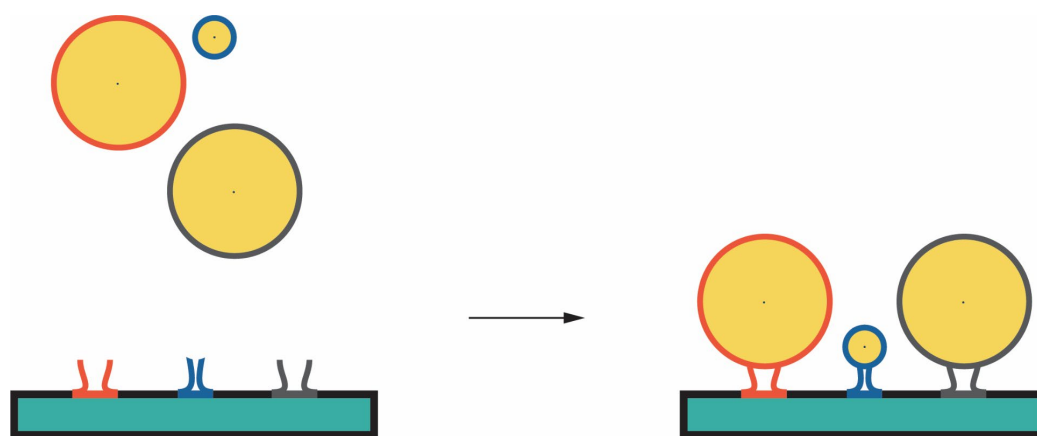
Figure 2.2. Schematic of binding to the DNA template surface. Green squares with black outlines are 2D DNA origami template. Yellow circles are nanoparticles. Red, blue, and grey curves/lines are capturing strands of 2D DNA origami template; red, blue, and grey circumference are DNA ligands of large and small gold nanoparticles, respectively.

(a)

(b)
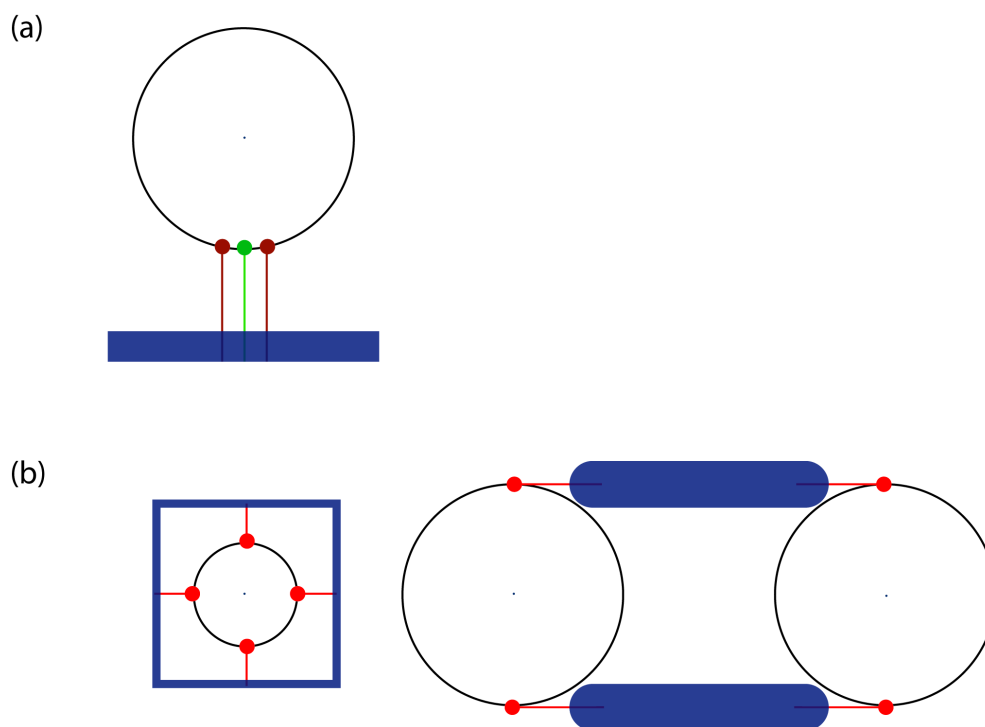
Figure 2.3. Schematic of tethering point distributions. (a) Cross section of binding to flat surface (blue square). Nanoparticle is bound to template surface by narrowly distributed anchors (brown and green lines with round ends) near the south pole. (b) Cross section of binding to our cage (blue square frame and rectangle with rounded corner). The central nanoparticle is bound by anchors (red lines with round ends) at two pairs of antipodal points (left), and the two large nanoparticles are anchored (red lines with round ends) at the antipodal points from two terminals and the cavity docks the large particles via shape complementarity.
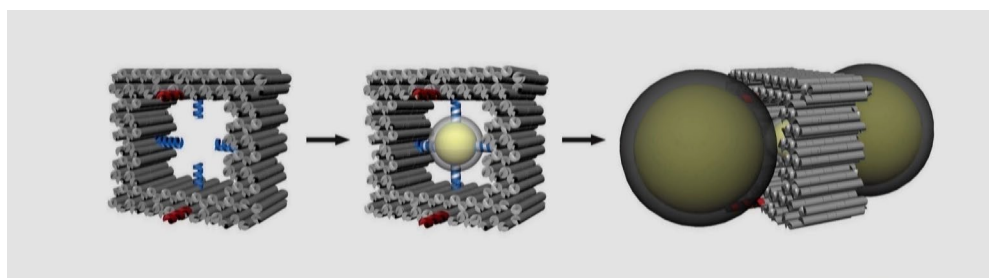
Figure 2.4. Schematic of our cage-mediated approach to assemble trimers. 10 nm AuNP is encapsulated in cavity of 3D DNA origami cage through base pairing between thiolated DNA ligands on AuNP surface and 4 inside capture strands projecting from the four cavity walls (blue helices). Then, two DNA functionalized 30 nm or 50 nm AuNPs are captured via outside captures strands (red helices) at the two openings forming the linear heterotrimer.
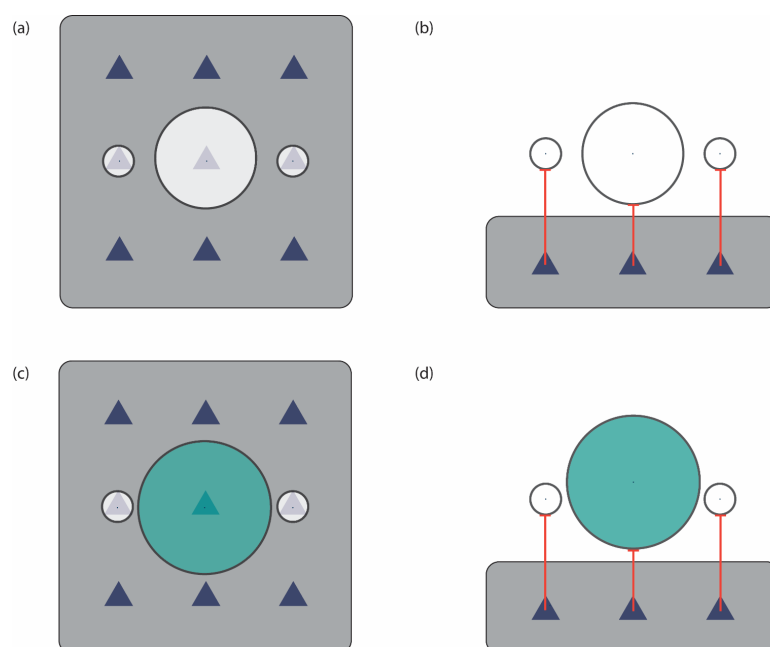
Figure 2.5. Schematic of poly-dispersed nanoparticles assembled on template surface. (a) Top view: Three nanoparticles with nominal sizes (white spheres) bound to the template surface (grey square: 2D tiles, blue triangle: binding site), the centers of three nanoparticles are aligned. (b) Side view: Three nanoparticles with nominal sizes bound to the template surface (red line: capture strand) (c) Top View: The central nanoparticle (green sphere) is slightly larger than its nominal size (the central white circle in (a)), and the poly-dispersed central particle leads to smaller than nominal gap size. (d) Side view showing the centers of three nanoparticles are not aligned indicating bond angle variations caused by poly-dispersed central nanoparticle.

2.2   Materials and Method

Materials are included in section 2.2.1. Thiolated DNA functionalization of gold nanoparticles is described in section 2.2.2, and the design and folding DNA origami cage are in section 2.2.3 together with the trimer assembly protocol. Assembled trimers are separated from unreacted nanoparticles by gel electrophoresis (section 2.2.4) and dynamic light scattering (DLS) was used to optimize trimer synthesis (section 2.2.5). To have plasmonic and structural characterizations, trimers are examined by UV/Vis spectroscopy (section 2.2.6), fluorimetry (section 2.2.7), SERS (surface enhanced Raman scattering) spectroscopy (section 2.2.8) and scanning electron microscopy (SEM) in section 2.2.9. Furthermore, FDTD (finite-difference time-domain) simulations are included in section 2.2.10.

2.2.1 Materials

M13mp18 ssDNA (scaffold) was purchased from New England Biolabs (NEB), resuspended in ultrapure water, and used without further purification. All staple DNA strands were purchased from Integrated DNA Technologies (IDT), diluted with 1× Tris-EDTA (TE) buffer without further purification. Regular 3' and 5'thiol-modified and carboxytetramethylrhodamine (TAMRA)-labeled 3'thiol-modified DNAs were purchased from IDT (Fig.1.8), resuspended in ultrapure water without further purification. DNA loading dye was purchased from Fischer Scientific. SYBR green (I) DNA stain and TAMRA mixed isomers were purchased from ThermoFisher. Agarose and Tris-Borate-EDTA (TBE), EDTA (Ethylenediaminetetraacetic acid), and TE buffers, Tris, sodium dodecyl sulfate (SDS), sodium chloride (NaCl), magnesium chloride ($MgCl_2$), tri(carboxyethyl) phosphine hydrochloride (TCEP), PEG (polyethylene glycol) and dithiothreitol (DTT) were purchased from MilliporeSigma, USA. Colloidal solutions of unconjugated (bare) 10 nm, 30 nm, and 50 nm AuNPs were purchased from Ted Pella. All staple DNAs and thiolated DNA sequences are summarized in Table A.1-Table A.4 (Appendix).

2.2.2 Functionalization of Gold Nanoparticles

The protective disulfide bond of thiolated DNAs was cleaved to form monothiol using TCEP (stock concentration of 100 mM) at room temperature (RT) in water, and the molar ratio of thiolated DNA to TCEP was 1:1000. The reduced thiolated DNAs were purified using Amicon ultra centrifugal filters (MilliporeSigma) with a molecular weight cut-off (MWCO) value of 3k Da twice to remove the small molecules. The purified mono-thiolated DNAs were added to bare AuNP with a DNA to AuNP molar ratio of 660:1 for 10 nm AuNPs, and 9090:1 for 30 nm AuNPs, in ultra-pure water containing 0.1% (w/v) SDS, then incubated with gentle shaking on a vortex mixer overnight at room temperature (RT). To functionalize 50 nm AuNPs,[32] there are two other requirements: (1) the total volume for each batch needs to be ≤0.2 mL (2) the final DNA concentration needs to be > 3.0 µM. After overnight incubation, a slow salt-aging method was used to promote the attachment of thiolated DNA to AuNP surfaces.[33]A concentrated NaCl stock solution (5 M) was added to AuNP and thiolated DNA mixture to increase the [NaCl] by 0.050 M. The mixture was then backfilled with N_2, sonicated for 5 seconds, and incubated at least 1 hour with gentle shaking at RT. Such salt-additions were repeated until reaching a final NaCl concentration of 0.30 M for 10 nm AuNP and 30 nm AuNP, 0.50 M for 50 nm AuNP then the mixture was left on RT to incubate overnight with gentle shaking. The 10 nm functionalized AuNPs (fAuNPs) were washed with ultra-pure water in 100k Da Amicon filters eight times to

remove excess thiolated DNAs. The 30 nm and 50 nm fAuNPs were purified by centrifugation at 14,000×g for 3 minutes in a 2 mL Eppendorf Microcentrifuge tube three times. After each centrifugation, the supernatant was removed and then resuspended in ultra-pure water. Purified fAuNPs were backfilled with N_2 and stored in a refrigerator at 4 °C before use. The concentrations of fAuNPs were determined from the optical absorbances at 520 nm (10 nm AuNP), 528 nm (30 nm AuNP) and 530 nm (50 nm AuNP) assuming no change in molar extinction coefficients after DNA functionalization. For the SERS detection, a mixture of TAMRA-labeled mono-thiolated DNA and 5× regular mono-thiolated DNA was used, and the molar ratio of total thiolated DNA to 10 nm AuNP was 660:1, all other steps remained unchanged. All fAuNPs were stable in the trimer assembly buffer (TAB) containing 1.0 mM EDTA, 5.0 mM Tris, 12.0 mM $MgCl_2$, and 0.30 M NaCl at RT or subject to prolonged thermal annealing, which is ideal for the directed assembly by DNA origami.

2.2.3 Design of 3D DNA Origami Cage and Syntheses

Our 3D origami cage with a cuboid cavity (20 nm × 20 nm × 17 nm), a modification of Yan's nanocage,[32] was designed with honeycomb lattice using caDNAno (http://cadnano.com/). The software generated 196 staple strand sequences that are complementary to that of single-stranded M13mp18 scaffold DNA. The cage has 124 DNA helices and an overall dimension of 47 nm × 40 nm × 17 nm (Fig.2.6-7) estimated by using 0.34 nm per base pair and 2 nm DNA helix width.[33] To avoid blunt-end stacking between the cages,[32] either two bases are left unpaired or two extra thymines (T) are added at the ends of each helix.

To bind the small nanoparticle in the cavity, four inside capture strands all have 5' end extensions and protrude from the centers of helices # 31,41,96,73 respectively (Fig.2.7c). There are two outside capture strand designs: the first design is for 30 nm-10 nm-30 nm and 50 nm-10 nm-50 nm trimers, where the four capture strands are extended from helices #39, 105, 38 and 106 respectively, and all extensions are on 3' end (Fig.2.7d); the second design is for 30 nm-10 nm-50 nm trimer, where the four outside capture strands protrude from two ends of helix 38 and helix 106 respectively, and each of two openings has two capture strands (Fig.2.7e) from 3' and 5' ends respectively.

The molar ratio of the scaffold to capture strands was 1:1, while 10× other staples with respect to scaffold were used. The mixture of the scaffold (10 nM) and staples was placed in a folding buffer (1 mM EDTA, 5 mM Tris, 12 mM $MgCl_2$) and slowly cooled from 90 °C to 25 °C over 2 days in a thermal cycler. The cooling rate at effective folding temperatures 60 °C to 40 °C was reduced

to –0.2 ˚C/hr. Four methods, PEG precipitation,[34] gel extraction,[35] Amicon ultrafiltration and gel filtration,[35-36] were explored to purify the folded origami cage from excess staples. The concentration of purified origami was determined by the optical absorbance of DNA at 260 nm. The concentration of unpurified origami was estimated by assuming a 100% folding yield. The purified or unpurified origami cages were mixed with purified 10 nm fAuNPs in TAB with 0.05% SDS, backfilled with N_2. The mixture was first slowly heated from 20 ˚C to 42 ˚C, and then thermal annealed from 42 ˚C to 20 ˚C over 34 hours in total to encapsulate 10 nm fAuNP in the origami cage cavity. The cage-encapsulated 10 nm fAuNPs were used without purification. Then the purified 30 nm/50 nm fAuNP and cage-encapsulated 10 nm fAuNPs were mixed in the TAB with 0.05% SDS, backfilled with N_2, and incubated at RT in the dark for ~4 hours to form the target trimers, the synthesized trimers were stored at 4 ˚C prior to purification.
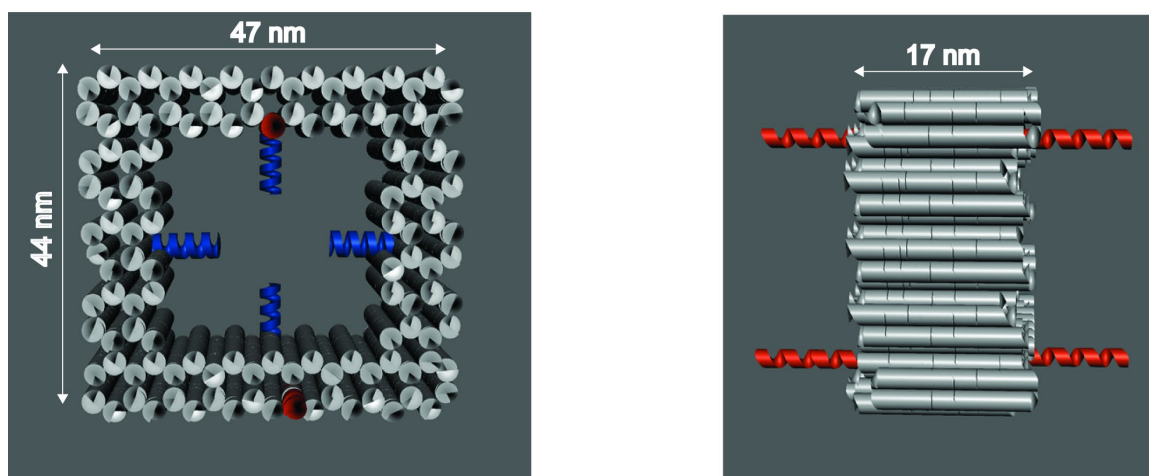
Figure 2.6. Sizes of 3D DNA origami cage. Blue helices are inner capture strands, red helices are outside capture strands.
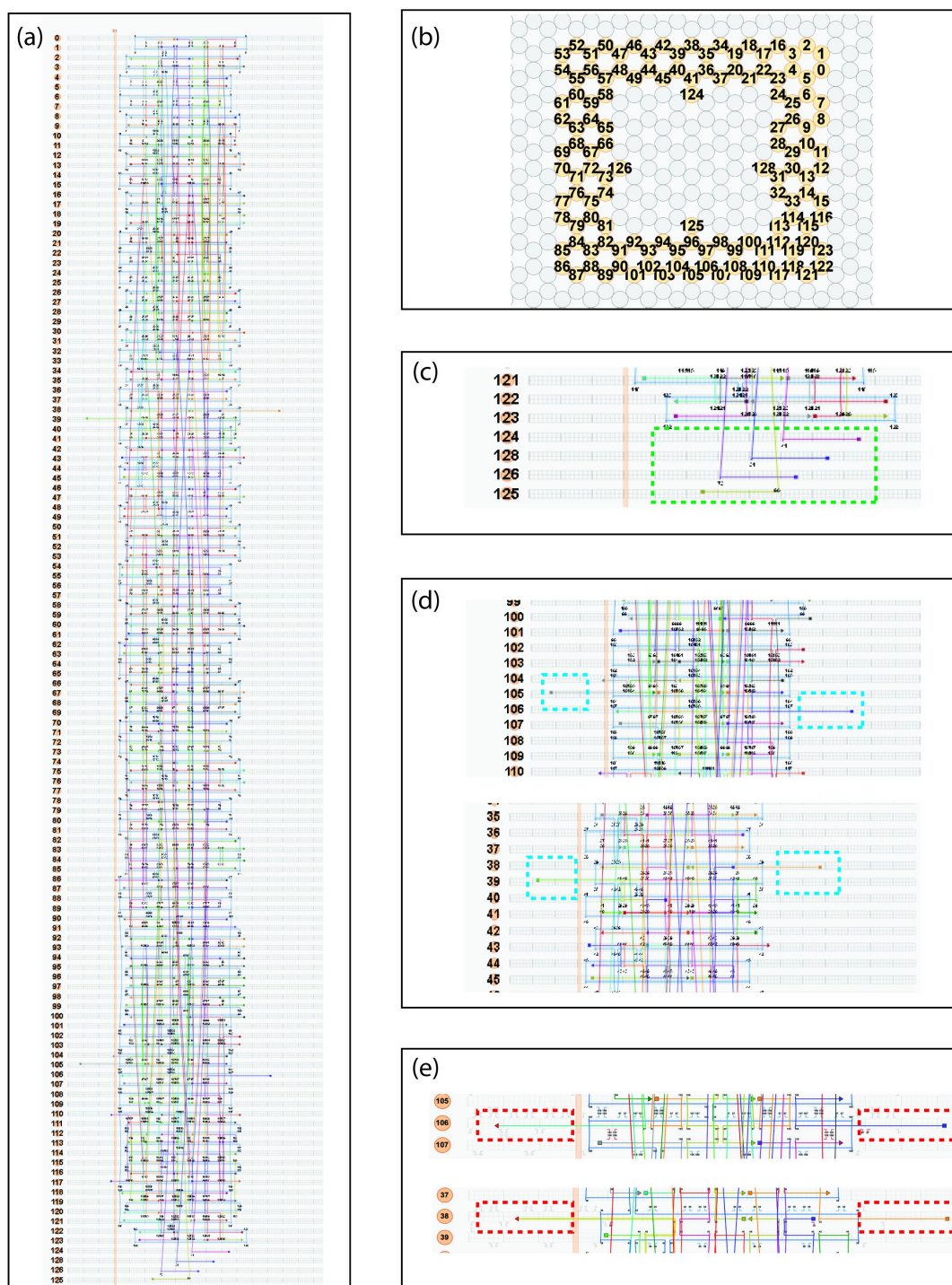
Figure 2.7. CaDNAno design of cage. (a) Map of staple strands (triangle end: 3' end, square end:5' end). (b) Map of honeycomb lattice where helices #123, #124, #125, #128 are added for visualization of inside capture strands located at helices #41, #73, #96, #31 respectively. (c) Inside capture strands (green dashed box). (d) Outside capture strands for 30 nm-10 nm-30 nm and 50 nm-10 nm-50 nm trimers (blue dashed box). (e) Outside capture strands for 30 nm-10 nm-50 nm trimer (red dashed box).

2.2.4 Purification of Trimers

After overnight incubation at RT, the mixture of cage-encapsulated 10 nm fAuNPs and 30 nm/50 nm fAuNPs was loaded with the help of a DNA loading dye in an agarose double gel layer system (running buffer: 0.5× TBE) at constant 65 V for 1 hour over ice.[37] The bottom gel layer was a 4% agarose gel to prevent leakage of the sample from the top layer, and a 0.8% or 1% top layer was poured directly on the bottom layer. After band separation appeared, the unwanted band was cut out, and a small pocket in front of the band of interest was dug through the top layer and filled with TAB. Then, the band of interest was electroeluted to the pocket and collected by micropipette. If needed, the purified heterotrimers could be concentrated by centrifugation (14,000×g, 5 minutes) in a 2 mL microcentrifuge tube (Eppendorf).

2.2.5 DLS Measurements

All dynamic light scattering (DLS) experiments were performed using ZETASIZER NANO series S90 (Malvern Panalytical) to measure D_h (hydrodynamic diameter, Fig.2.8). Samples were loaded in a micro volume quartz cuvette (50 μL) and measured using 632.8 nm laser with 90° scattering angle at 20 °C. Multiple narrow mode (MNM) algorithm was used for data analyzes.
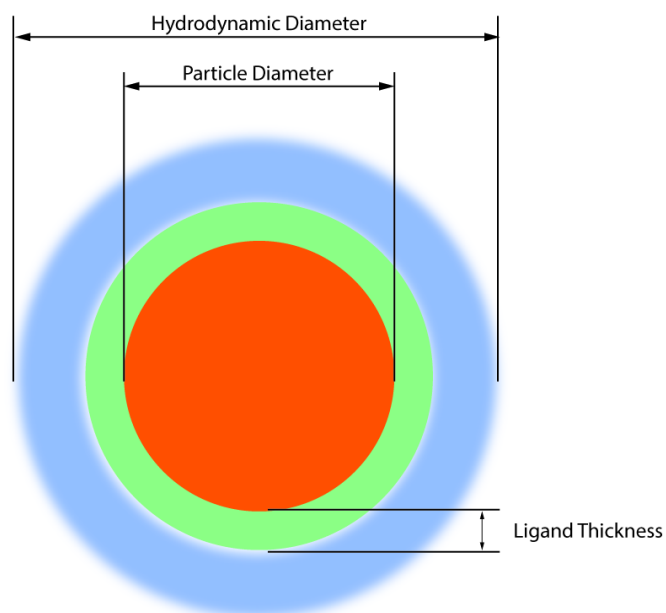
Figure 2.8. Schematic of hydrodynamic diameter. Blue halo: Hydration layer.

2.2.6 UV-Vis Measurements

Concentrations of DNA origami, thiolated DNA and bare unfunctionalized AuNP were determined using NanoDrop ND-1000 Spectrophotometer (Thermo Fisher Scientific). All UV-Vis spectra of trimer and fAuNPs were collected using a Perkin-Elmer Lambda 35 UV/Vis spectrophotometer and a 100 µL quartz cuvette.

2.2.7 Determination of TAMR Concentration on Trimer

TAMRA solutions of known concentrations were measured using a Horiba Jobin-Yvon Fluorolog®-3 fluorometer to construct a standard calibration curve of TAMRA. The solution containing heterotrimers was mixed with 0.5 M DTT (final DTT concentration of 0.1 M) overnight at RT to break the Au-S bond and desorb TAMRA labeled thiol-DNA from heterotrimers. After overnight incubation, the sample was centrifuged to precipitate the AuNPs, and the supernatant was collected for fluorescence measurements to determine the TAMRA concentration using a standard calibration curve (Fig.2.9).
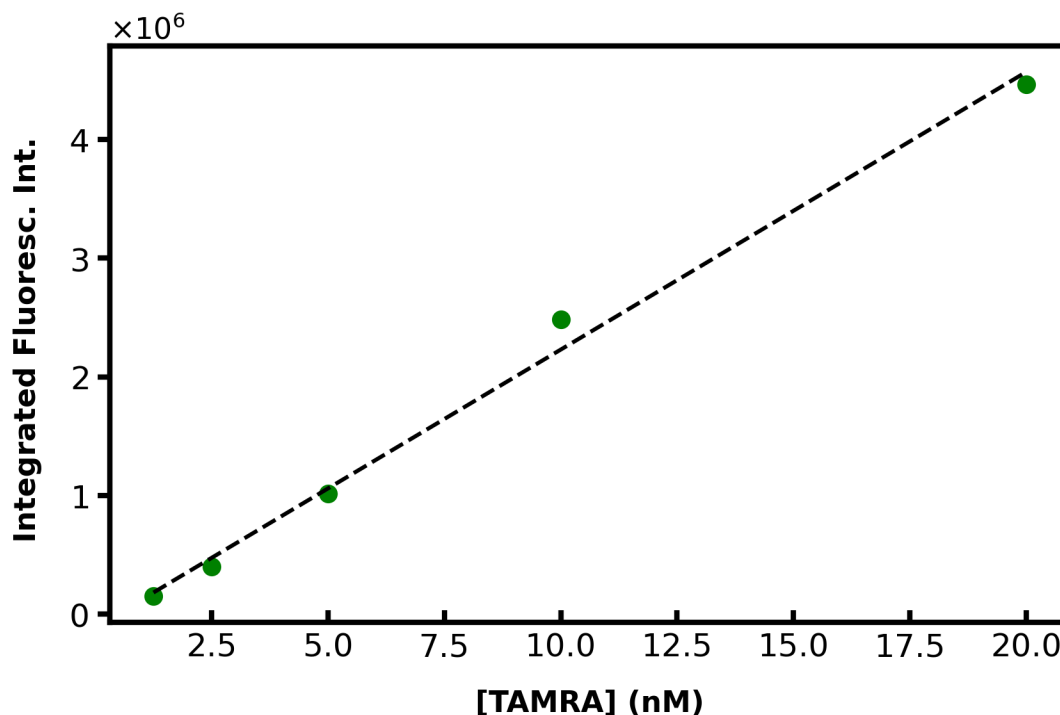
Figure 2.9. Fluorescence calibration curve of TAMRA. Excitation wavelength = 500 nm. Linear regression equation: y=233945x+239544 and R^2 = 0.9935.

2.2.8 SEM Characterization

3.0 µL of purified trimer was deposited onto Argon (Ar) plasma treated silicon wafers for ~2 minutes then washed with 20 µL water and dried in a vacuum chamber for 24 hours before SEM (Scanning Electron Microscopy) characterizations. The sample was imaged by Zeiss Gemini 500 FEG-SEM system with EHT 5.0 kV to 10 kV. The statistical analysis of gap sizes and bond angles were conducted using AutoCAD 2019 (Fig.2.10).
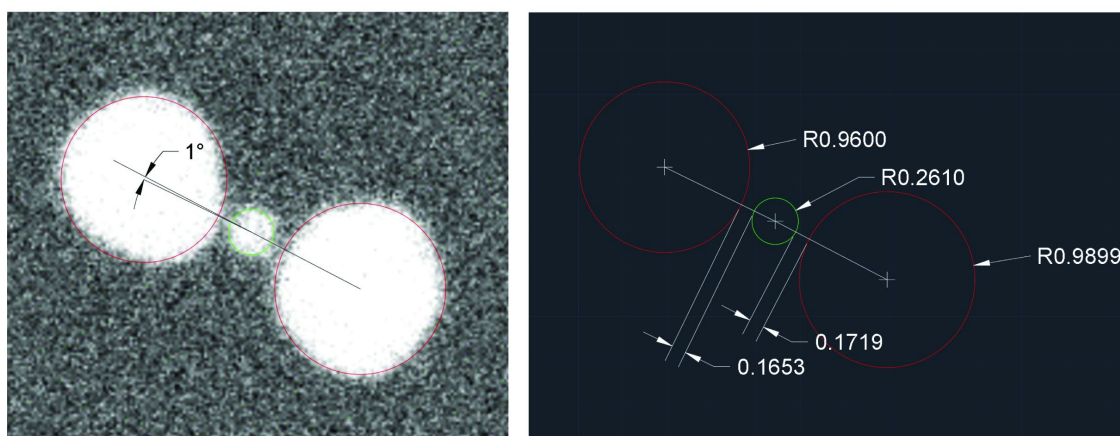
Figure 2.10. Bending angle and gap size analysis. Masks were placed on SEM image (shown as green and red circles on the left) using AutoCAD 2019. The bending angle was measured using the measuring tool in AutoCAD 2019. The size of AuNPs and gap sizes were measured in AutoCAD (right) and converted to actual values using SEM scale bar.

2.2.9 Raman Measurements

All the Raman and SERS spectra were measured using a Renishaw inVia™ Raman spectrometer with both a 633 nm and 785 nm excitation wavelengths. The laser was focused onto the sample using a 20× objective for all samples. The average power at the sample surface was 2.8 mW the samples collected at 633 nm. For the samples collected at 785 nm, the power used for TAMRA was 55 mW and the power for the trimer sample was 11 mW. The integration times were 30 seconds for the pure TAMRA measurements at both laser wavelengths. For SERS measurement of heterotrimeric chain with TAMRA tagged in the central particle, integration times were 30 seconds at 633 nm laser and 10 seconds at 785 nm laser. Normalizations were conducted to calculate SERS enhancement factors (EFs). Each sample was prepared for Raman and SERS measurements by drying ~10.0 µL of solution on a glass slide (wrapped by aluminum foil to reduce interference from glass Raman signals) for 10 min.

2.2.10   FDTD Simulations

All electrodynamics simulations were performed using Lumerical Finite Difference Time Domain (FDTD) Solutions software (Ansys, Inc.). The mesh size was set to 0.5 nm for all electric field simulation, and 1 nm for absorption simulation (Fig 2.11). Trimeric structures (including DNA origami and ligand shell) were modeled in AutoCAD 2019 as .stl file and exported to FDTD Solutions. The frequency-dependent optical constants of gold nanoparticles were adapted from Johnson and Christy. The DNA ligands were depicted as 2.5 nm thick shell (wireframe) with a refractive index of 1.7.[38] The DNA origami cage (wireframe) had a refractive index of 2.3.[38] The background refractive index was set as 1.3 for electric field simulation and 1.33 as absorption simulation. Custom MATLAB code was used to process exported electric field values from FDTD simulations of the trimers (Fig.A.11).
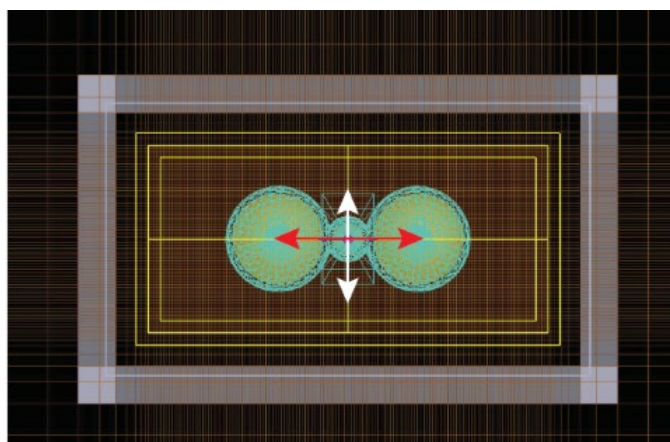
Figure 2.11. Set-up of FDTD simulation. Red and white double arrows indicated the longitudinal and transverse electric field polarization angles used for simulations.

2.3   Results and Discussions

The section will be organized into six subsections. Unlike the one-pot synthesis used in previous studies, our trimers require intricate multi-step synthesis to have controllable bond angle and gap distances. Section 2.3.1 will include a systematic investigation of each step where agarose gel electrophoresis and DLS results and the statistical analyses will be presented. 30 nm-10 nm-30 nm trimer, the analogue of CO_2, is the model trimer of which we will perform

detailed structural determinations in section 2.3.2 using SEM. Plasmonic characterizations of 30 nm-10 nm-30 nm trimers will be presented in section 2.3.3 accompanied by detailed FDTD simulations in section 2.3.4. In accordance with simulation, our 30 nm-10 nm-30 nm trimers were found to have about enhancement factors (EFs) on the order of 10^5 when excitation wavelength is 633 nm (a common laser wavelength), however, our simulation results predict that at 633 nm, a 50 nm-10 nm-50 nm trimer has over 10^8 EF, if true, it could enable single molecule detection. We therefore investigated the synthesis of 50 nm-10 nm-50 nm trimers using our cage in section 2.3.5 together with SEM and plasmonic characterizations. Preliminary data of 30 nm-10 nm-50 nm trimer is included to test the programmability of our cage in section 2.3.6.

2.3.1 Multi-Step Synthesis of 30 nm-10 nm-30 nm Trimer

Existing studies that use a DNA template to organize nanoparticles typically bind the nanoparticles to the addressable sites on the exterior of the template.[23] Therefore, the binding can be carried out in a single step. Our approach binds a nanoparticle to the interior of a 3D template. Hence, the nanoparticles need to be incorporated in separate steps after the formation of 3D DNA origami cage: encapsulation of the central small gold nanoparticle within the cage, and the binding of the terminal large nanoparticles to the two openings. A potential challenge is that such multistep synthesis/assembly requires more purification steps that diminish the overall yield. In particular, the driving force of all the three steps in our synthesis is non-covalent interactions (base-paring),[39] which may be disrupted during the purification steps. To produce trimers a high yield and better reproducibility, we carried out a systematic investigation that evaluated each of steps of self-assembly and purification. Here, we first synthesized the 30 nm-10 nm-30 nm trimer in three steps, and the first two steps are identical for all three trimers (30-10-30,50-10-50, and 30-10-50), and the final step only has minor differences.

2.3.1.1   Folding of 3D DNA Origami Cage

The whole trimer synthesis starts with the folding of the 3D DNA origami cage, and the overall yield of trimer synthesis largely depends on the cage folding yield. To optimize folding conditions, we investigated the two main factors that determine the cage folding: thermal annealing ramp, divalent-cation (Mg^{2+}) concentration.[40] To find the most effective annealing temperature range, we first used nearest-neighbor model to calculate the theoretical melting temperature (T_m) of each staple binding domain (Fig.2.12).[41] The statistical results showed that 81% staple binding domains have T_m in between 40-60 °C

inferring the slow thermal annealing ramp is needed at this temperature range. Folding of 3D DNA origami structures required much slower annealing ramp than their 2D counterparts. We used agarose gel to examine the products annealed at two different ramping rates, -1.5 °C/hr vs -0.2 °C/hr from 60 °C to 40 °C. We found the -1.5 °C/hr ramping rate produced smear in gel (Fig.2.13a) indicating mis-folded or unfolded structures. When -0.2 °C/hr ramping rate was used, two bands were present in lane 1 in Fig.2.13b: a narrow band on top and a broad band at the bottom. The bottom band was assigned to the shorter excess staples with a much higher electrophoretic mobility and the band on top was assigned to the folded cage. There was no smear in lane 1, indicating our cage was properly folded without noticeable amounts of mis-folded structures. It is interesting to note that the folded cage showed similar mobility as scaffold DNA in lane 2 in a low-percentage gel, in accordance with a previous study.[32] In contrast to 2D DNA tiles, more divalent cations are needed to assist 3D origami folding and stabilize the folded nanostructures. For the annealing ramp tests, we used 12.0 mM Mg^{2+}, a divalent cation concentration commonly used for 3D origami folding, but it was still pertinent to explore the effects of Mg^{2+} concentrations, which might facilitate the ionic strength adjustments for the succeeding steps.[40] Surprisingly, the range of Mg^{2+} concentration for effective folding was found to be narrow (Fig.2.14), when $[Mg^{2+}] \geq 16.0$ mM, annealed products were either completely stuck in the loading well (lanes 1-2) or only formed a very faint folded band (lane 3), when $[Mg^{2+}] \leq 14.0$ mM, a well-defined band emerged with (lane 4) or without (lane 5) a faint slowest-migrating band. The extra slow-migrating band was assigned to be a multimer, which is common in origami folding. To reduce the interference of multimer and other unwanted structures, we used 12.0 mM $MgCl_2$ to fold cage at -0.2 °C/hr from 60 °C to 40 °C.
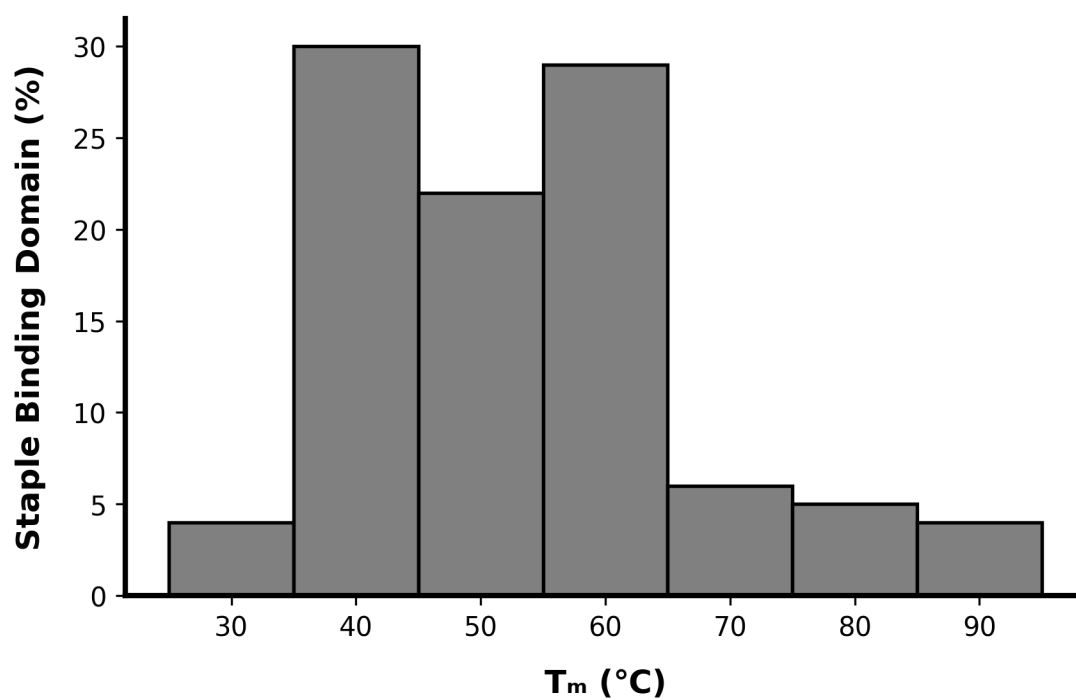
Figure 2.12. Distributions of theoretical melting temperatures of staple binding domains. The calculation method is described in ref 41.
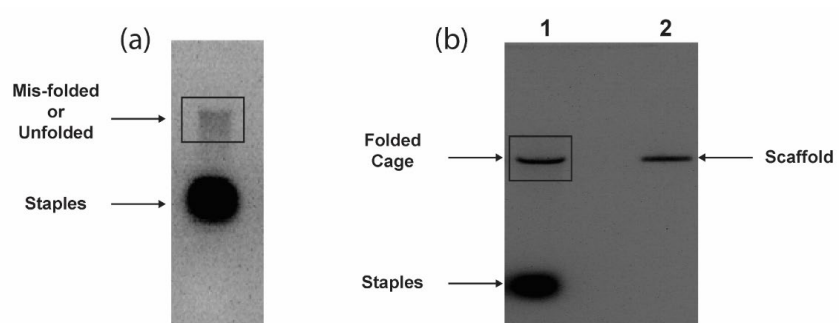
Figure 2.13. Agarose gel results of cage folding.(a) Ramping rate: −1.5 °C/hr. (b) Ramping rate: –0.2 °C/hr.
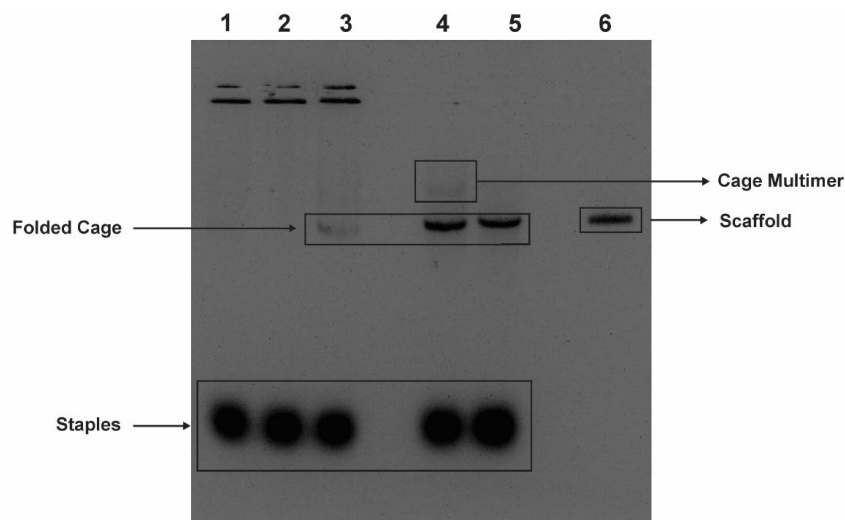
Figure 2.14. Mg^{2+}-dependence of cage folding. Lanes 1: 20.0 mM MgCl$_2$. Lane 2: 18.0 mM MgCl$_2$. Lane 3: 16.0 mM MgCl$_2$. Lane 4: 14.0 mM MgCl$_2$. Lane 5: 12.0 mM MgCl$_2$. Lane 6: Neat scaffold.

2.3.1.2 Investigations of 3D DNA Origami Cage Purification

An important question is whether the cages needed to be purified. On one hand, the more purification steps are involved, the lower the overall yield of multi-step synthesis; on the other hand, some of the excess staples in unpurified cage might interfere with the encapsulation step by binding to the nanoparticles. There is also no consensus in the literature.[32,42] Thus, we first sought to find a purification method that has consistent high yield with minimal structural damages.

We tested four conventional methods, PEG precipitation, gel extraction, Amicon ultrafiltration and gel filtration, to purify our cage, and the purification yields were calculated and included in Fig.2.15. The purification yield of PEG precipitation needs high origami concentration and depends on the shape of the DNA origami,[34] our cage probably is not concentrated enough and have unfavorable shape resulting a ~10% purification yield; gel extraction method not only had low yield (~10%) but also produced considerable contaminations (Fig.2.16).[35] As a result, PEG precipitation and gel extraction were not ideal for cage purification. Amicon ultrafiltration is the most convenient purification method and produced reasonable yield (47.3±4.8%), however, the purification yield largely depends on the ionic strengths of the replenish buffer (Fig2.15b), the higher the Mg^{2+} concentrations, the lower the purification yield as Mg^{2+} bridged column membrane and the cages making the

sample recovery difficult. We later found that the cages could be damaged using 1× TE or buffer with 5 mM $MgCl_2$ as replenish buffer (Fig.A.2). Therefore, Amicon ultrafiltration was not proper for cage purification. Gel filtration method, albeit having the highest average yield (58.0%), resulted in large batch to batch variations (SD=22.3%), possibly due to the use of self-packed spin columns. In addition, gel filtration often had low recovery concentration (~2.0 nM) with large volume, and the extra concentrating step would cause severe sample loss. Taken together, none of these four conventional purification methods met our requirements. Hence, whether the cages should be purified remain unclear. As currently there is no perfect answer to this question, and the best compromise was then explored using the encapsulation step.
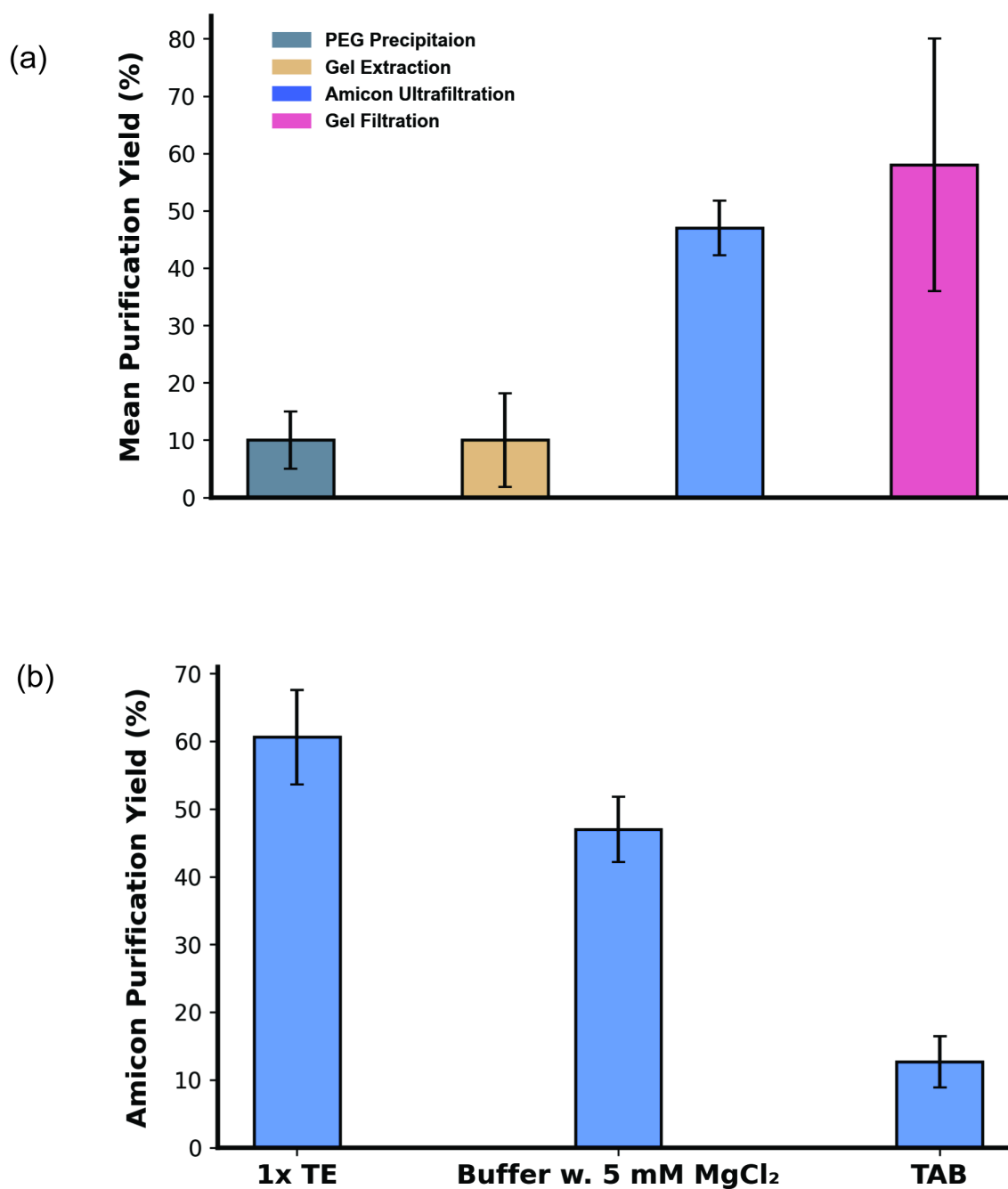
Figure 2.15. Cage purification yields. (a) Purification yields using four conventional methods. Yields from left to right: 10.5%±5.1, 10.3%±8.2, 47.3%±4.8, 58.0%±22.3. (b)Purifications yield of Amicon ultrafiltration using different replenish buffers. Yields from left to right: 60.6%±7.0, 47.1%±4.8, 12.7%±3.8.
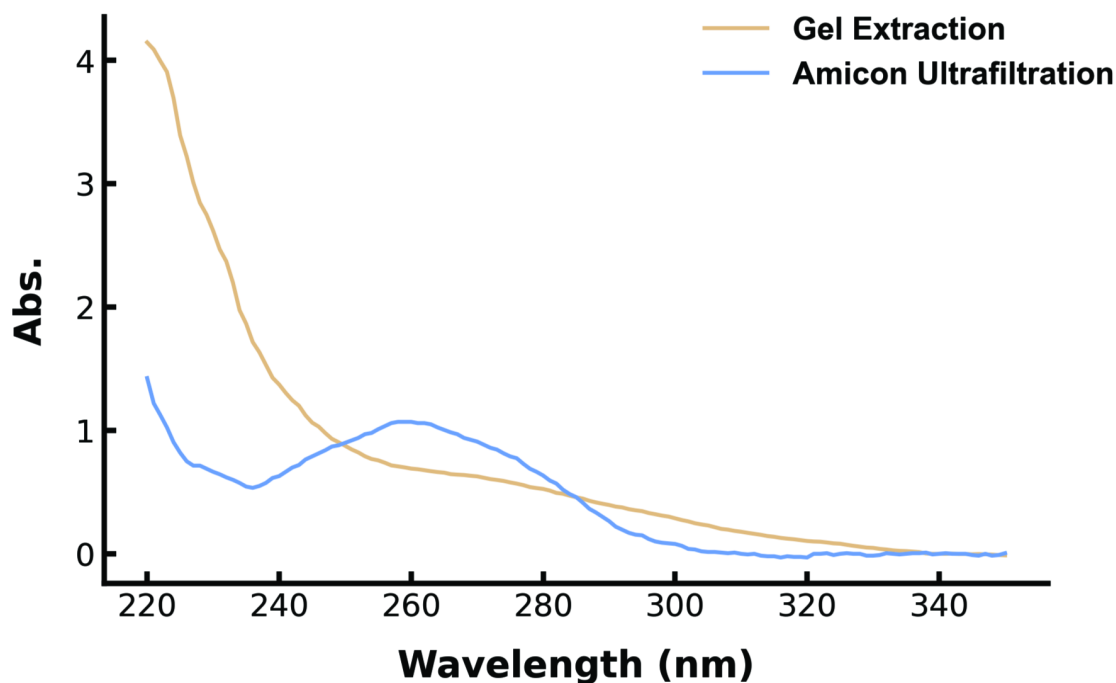
Figure 2.16. UV-Vis absorption spectra of purified cages. Cages purified by Amicon ultrafiltration showed clear DNA absorption peak at 260 nm, while cages purified by gel extraction lacked a distinctive peak at 260 nm indicating the presence of contaminations likely from agarose.

2.3.1.3 Encapsulation of the Central Nanoparticle

To carry out the second step of the trimer synthesis, we mixed 10 nm fAuNP with purified and unpurified cage respectively and subjected the mixtures to thermal annealing. Like previous studies by Yan et al.[32] and Seidel et al.[42], thermal annealing was used to promote encapsulation possibly to overcome the electrostatic repulsion between the 10 nm fAuNP and the cage cavity where DNA density is high. The annealed mixtures were examined in agarose gel and the exemplary results were in Fig.2.17.

Two pink bands without smear showed up for both mixtures (Fig.2.17). The fast-migrating band was assigned to unreacted 10 nm fAuNP, and the slow-migrating band the cage-encapsulated 10 nm fAuNPs. The well-defined, fast-migrating band suggested 10 nm fAuNPs were uniform in both size and ligand density. The slow-migrating pink band also overlapped with the cage band under UV (Fig. 2.18), which further confirmed the successful encapsulation of the 10 nm fAuNPs. The slow-migrating band on the right was more intense

than that on the left (Fig.2.17), indicating the encapsulation yield was higher using purified cage. To have a quantitative comparison, we used gel molecular weight analyzer in OriginPro 2022 (Fig.2.19) to analyze gel results and calculated the encapsulation yield using equation (1), where n is the molar ratio between 10 nm fAuNP and cage, $I_{top\,band}$ is the integrated area of the slow-moving pink band, $I_{bottom\,band}$ is the integrated area of the fast-moving pink band.

$$Encapsulation\ yield = \frac{I_{top\,band}}{I_{bottom\,band} + I_{top\,band}} . n \qquad (1)$$

The encapsulation yield of the purified cage was about twice as high as that of the unpurified cage (Fig.2.20). We suspected the excess staples attached to the surface of some 10 nm fAuNP reduced the encapsulation yield. Although the purification of the cages improved the yield of encapsulation step, 50% or more of the cages were lost in the purification step. Therefore, the overall yield was about the same whether the cages are purified or not. To simplify the process and reduce uncertainty in the overall yield, encapsulation using unpurified cages was the best compromise for trimer synthesis given the non-optimal cage purification step. The stoichiometric ratio (nominal molar ratio between 10 nm fAuNP and unpurified cage) was also investigated in the encapsulation step. 10 nm fAuNP has much lower absorption/scattering efficiency than its larger counterparts, therefor, gel electrophoresis often cannot produce clear a detectable band at low concentrations (<4.0 nM). To find the best stoichiometric ratio,[42] we then implemented DLS,[43] a more sensitive technique for spherical nanoparticle detection. Though our cage is not spherical, it is suitable for DLS measurements because of its high sphericity ($\Psi \approx 0.8$) calculated using equation (2) where Ψ is sphericity, V_p is actual volume of an object, and V_{cs} is the volume of circumscribing sphere

$$\Psi = \sqrt[3]{\frac{V_p}{V_{cs}}} \qquad (2)$$

We first tested whether the excess staples in the unpurified cage could alter the hydrodynamic diameter of the 10 nm fAuNP. 10 nm fAuNP, with (solid blue) or without staples (dashed blue), showed (Fig.2.21a) same peak about 22 nm that agreed well with its nominal D_h values of 20 nm (5 nm DNA ligand thickness), and the results indicated that excess staples did not cause a size change of 10 nm fAuNP. We then monitored the size changes when mixing cage and 2× 10 nm fAuNPs (Fig 2.21b). DLS was able to discern three major species with distinct D_h, including neat 10 nm fAuNPs (22 nm, blue curve, Fig.2.21b), neat unpurified cages (57 nm, red curve, Fig.2.21b), and mixture of cages and 2× 10 nm fAuNPs (black curve, Fig.2.21b). After the mixture at RT (solid black) was annealed, the peaks associated with pure fAuNPs and cages disappeared,

and a slightly broader new peak emerged at 44 nm (dashed black, Fig.2.21b). It is noted that the new peak at 44 nm was likely a mixture of unreacted 10 nm fAuNP and the cage-encapsulated 10 nm fAuNPs. The decrease of cage D_h value after encapsulation implied that the binding of 10 nm fAuNP to the four capture strands in the interior of the cage restricted the free expansion of the cage in water, leading to a smaller D_h. To find the optimal stoichiometric ratio, we annealed mixtures of different stoichiometric ratios, and subjected the mixtures for DLS measurements (Fig.2.22). An apparent trend was when more 10 nm fAuNP was used, the peak of the thermal annealed mixture became wider and more shifted to ~22 nm. We hypothesized as AuNP is a much more efficient scatter than DNA origami, the excess unbound 10 nm fAuNP contributed significant scattering signals, widening the mixture peak. It is noted that the peak of the lowest stoichiometric ratio (light brown line in Fig.2.22) didn't indicate all 10 nm fAuNP was encapsulated, there might still be free 10 nm fAuNP whose concentration was too below to be detected. Nevertheless, low stoichiometric ratio leads to low overall yield, and the best compromise for trimer synthesis is to use 1× 10 nm fAuNP with respect to the unpurified cage.

Prior to attaching the terminal large fAuNPs, we tested the stability and shelf life of the cage-encapsulated 10 nm fAuNPs. Larger fAuNPs tended to self-aggregate in high ionic strength, therefore, it is important to know the stability of the cage-encapsulated 10 nm fAuNPs. in a lower ionic strength buffer. We diluted the cage-encapsulated 10 nm fAuNPs by water and used DLS to monitor the size changes (Fig.2.23a). When the ionic strength decreased by 4-fold, cage-encapsulated 10 nm fAuNPs degraded quickly, the sole peak at ~44 nm broke into two peaks (purple curve) of which the ~22 nm peak overlapped with the neat 10 nm AuNP, and the peak at ~75 nm partially overlapped with the neat cage. To maintain stability of the cage-encapsulated 10 nm fAuNPs, it is necessary to store it in a buffer with high ionic strength such as TAB. The self-assembled nanostructures are prone to decomposition over time; therefore, it is important to explore the shelf-life of the cage-encapsulated 10 nm fAuNPs stored in TAB at 4 °C (Fig.2.23b). The gel results of freshly made and 12-day-old the cage-encapsulated 10 nm fAuNPs showed no difference indicating shelf-life of the cage-encapsulated 10 nm fAuNPs was at least 12 days with proper storage conditions.

We anticipated that our cage could localize the terminal large fAuNPs via multiple cage/fAuNP interactions, which required some cage mechanical flexibility. One way to probe the cage mechanical flexibility is to test the maximum fAuNP size our cage can encapsulate.[32] We mixed and annealed 30 nm, and 50 nm fAuNPs with the unpurified cage at the molar ratio 2:1

respectively. Gel electrophoresis (Fig.2.24) was used to analyze the annealed mixtures as large fAuNPs are better light scatters, and their much higher polydispersity making DLS measurements inaccurate. We anticipated that 30 nm fAuNP could be ultimately encapsulated but not 50 nm fAuNPs. 50 nm fAuNPs experienced severe steric hindrance and were either too large to fit in the cage or only enter the cage partially indicated by a pink smear in lane 2. For the 30 nm fAuNP, two pink bands appeared in lane 1: a slow-migrating pink band associated with the cage-encapsulated 10 nm fAuNPs and a fast-moving unreacted 30 nm fAuNP band, which implied that our cage has mechanical flexibility to accommodate fAuNPs slightly larger than the designed inner cavity.
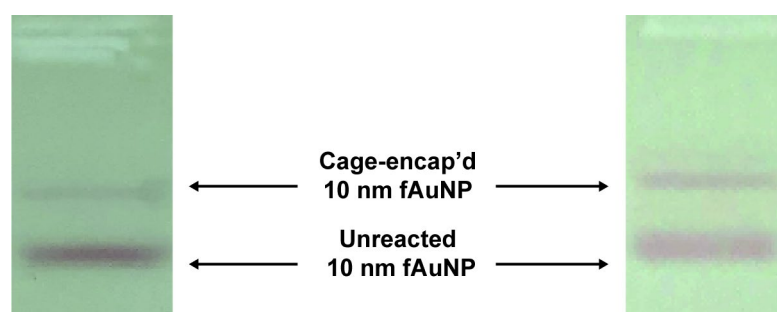
Figure 2.17. Unstained agarose gel results of encapsulation step. Left: Unpurified cage with 2× 10 nm fAuNPs. Left: Purified cage with 2× 10 nm fAuNPs.
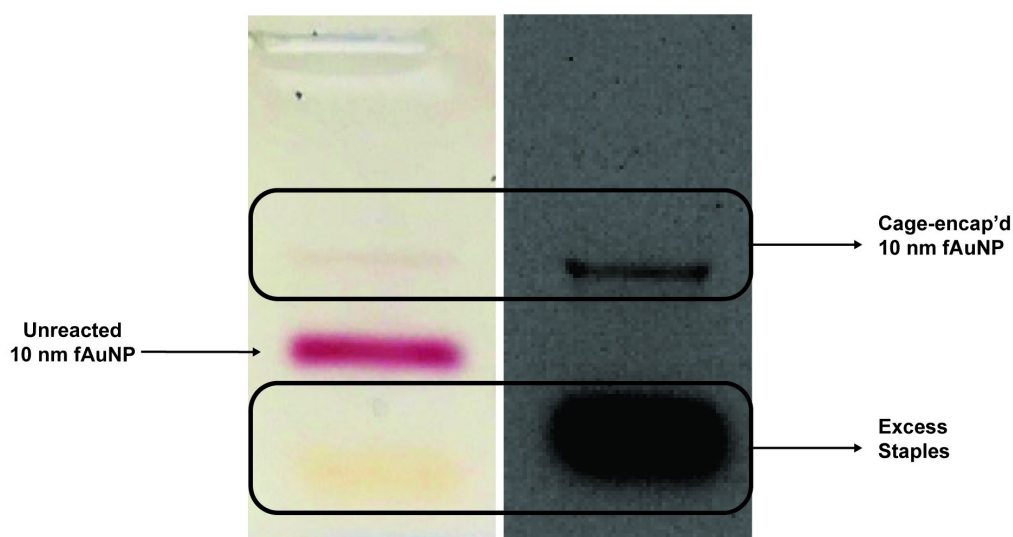
Figure 2.18. Stained agarose gel results of encapsulation step. Thermal annealed unpurified cages and 4× 10 nm fAuNPs showed two well-defined pink bands (left) and a broad yellow band at bottom (left), the

faint pink band on top lined up with the fluorescence signal of the cage (right). It was surprising to observe a broad yellow band at bottom (left) that overlaps with fluorescence signal of staples (right), and it was used as the reference to visualize the band overlap of the cage-encapsulated 10 nm fAuNPs.
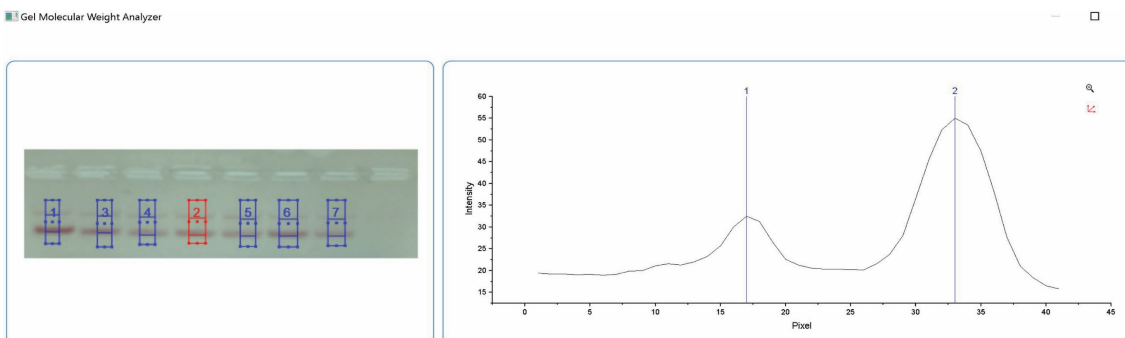
Figure 2.19. Schematic of encapsulation yield analysis. Lane 2 on the left was selected where two pink bands were visible, the slow-moving pink band was peak 1 on the right, peak 2 was the fast-moving band. The two peaks were exported and integrated for encapsulation yield calculations.
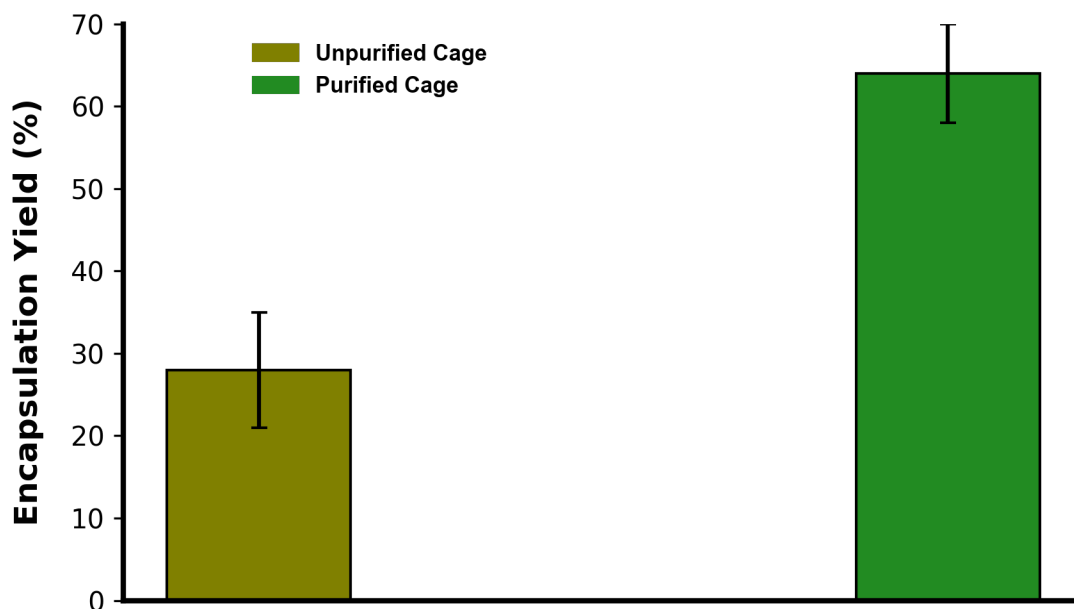
Figure 2.20. Encapsulation yields of DNA origami cages with and without purifications. Yields from left to right: 28.2%±7.2, 64.3%±6.0.

(a)

(b)
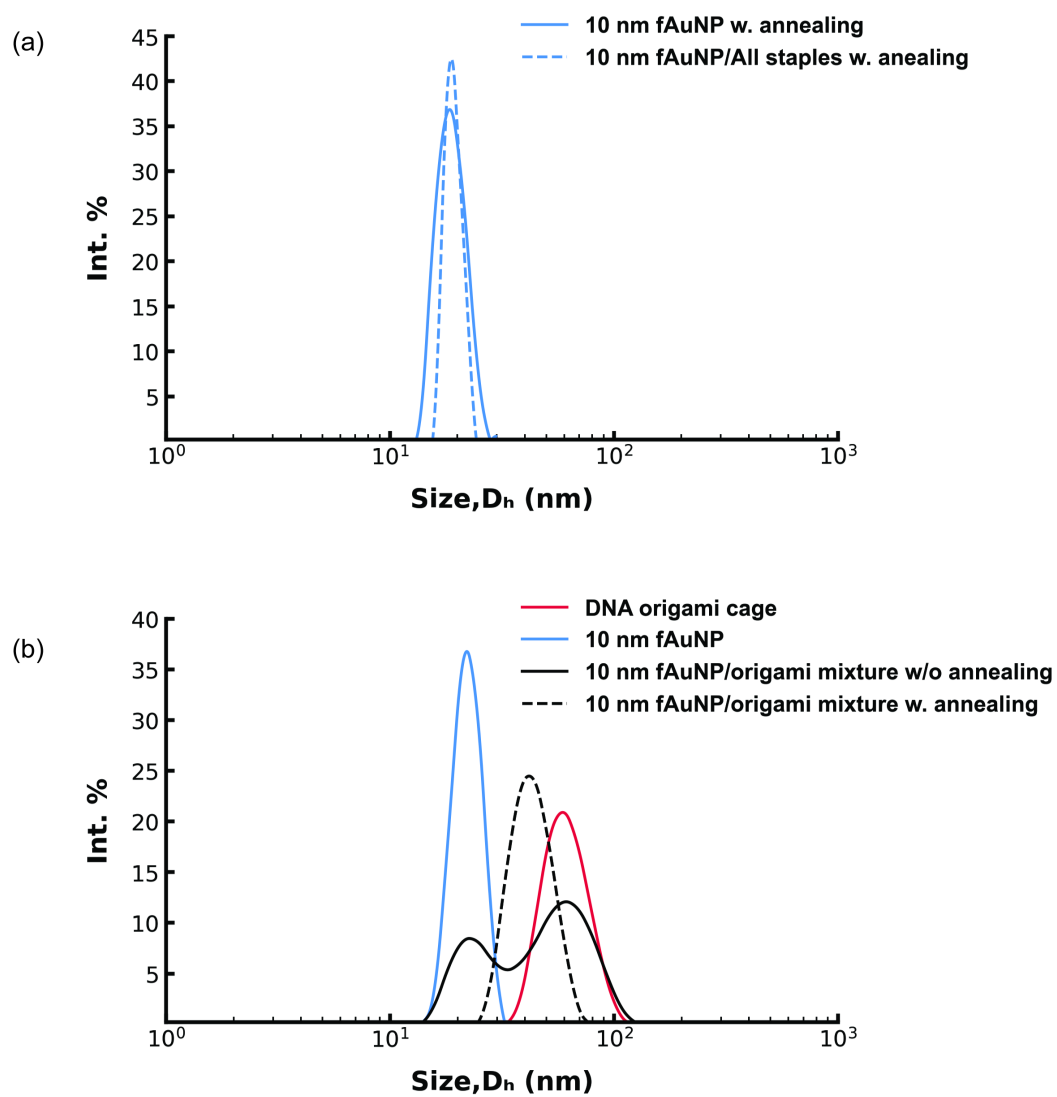
Figure 2.21. DLS analysis of 10 nm fAuNPs encapsulation in cage cavity. Neat DNA origami cage and neat 10 nm fAuNPs were annealed.
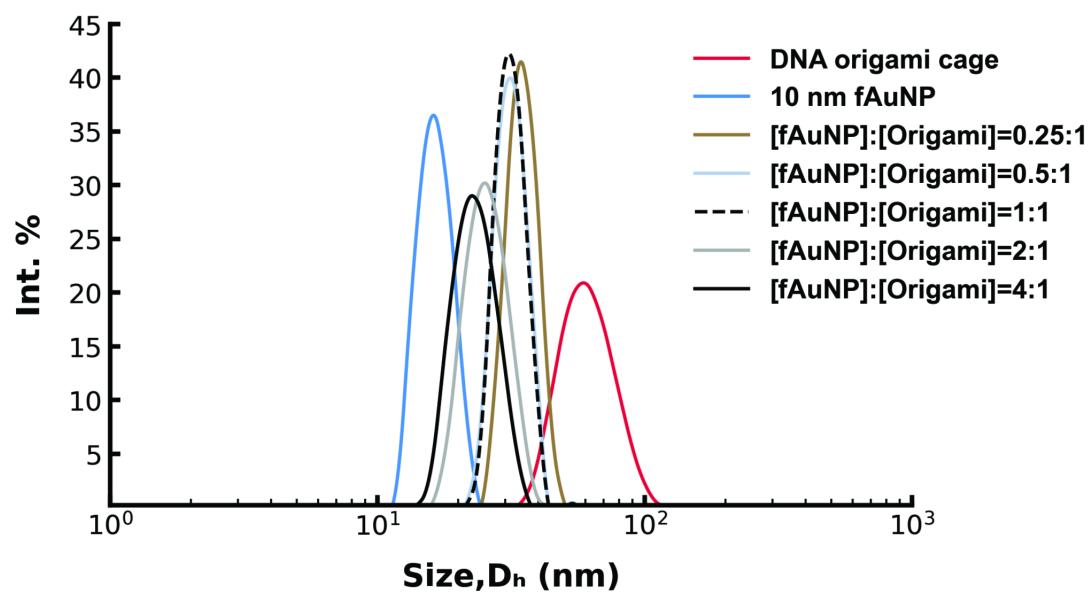
Figure 2.22. DLS titration of encapsulation. All samples were annealed.
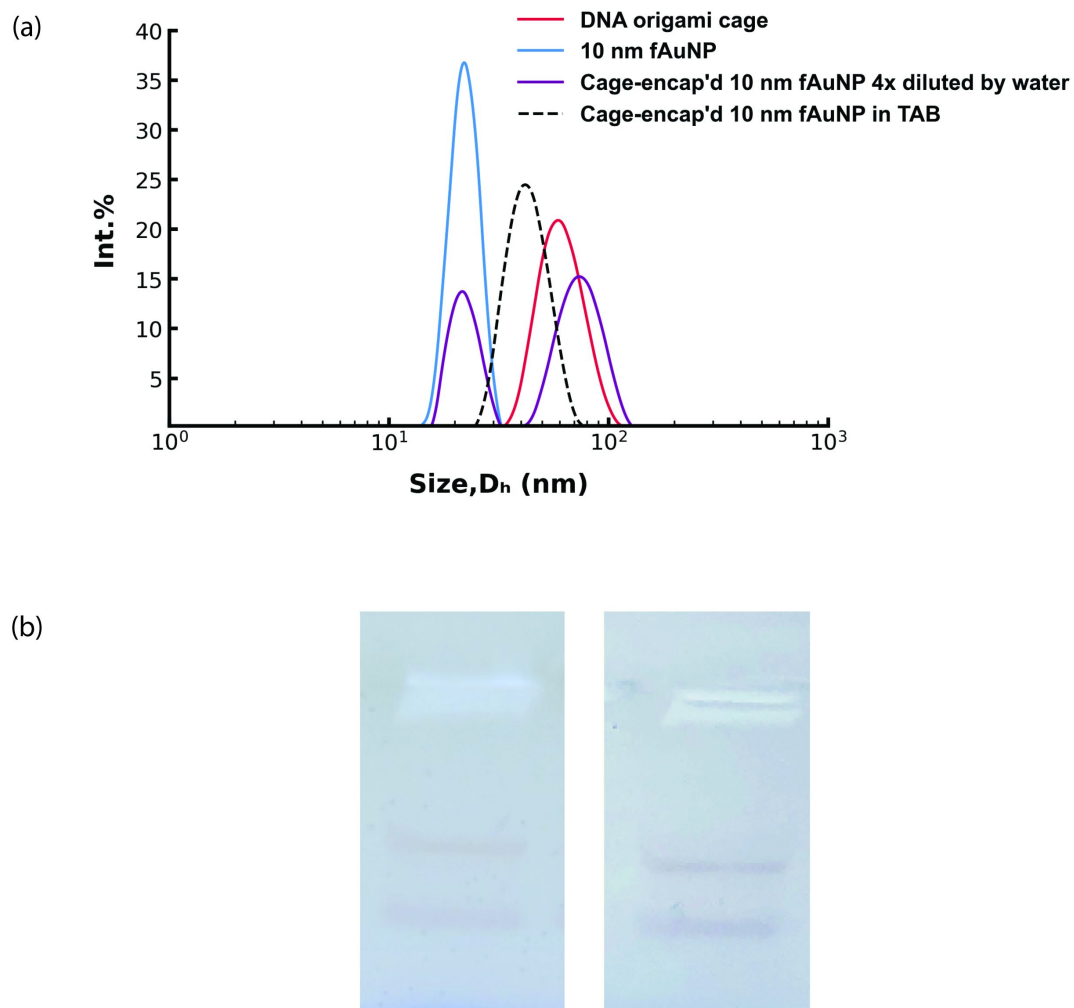
Figure 2.23. Stability analysis of the cage-encapsulated 10 nm fAuNPs. (a) DLS analysis of stability in buffers with different ionic strengths. Neat DNA origami cages and neat 10 nm fAuNPs were also annealed (b) Agarose gel results of cage-encapsulated 10 nm fAuNPs shelf-life. Left: the freshly-made cage-encapsulated 10 nm fAuNPs. Right: the cage-encapsulated 10 nm fAuNPs stored in 4 °C for 12 days.
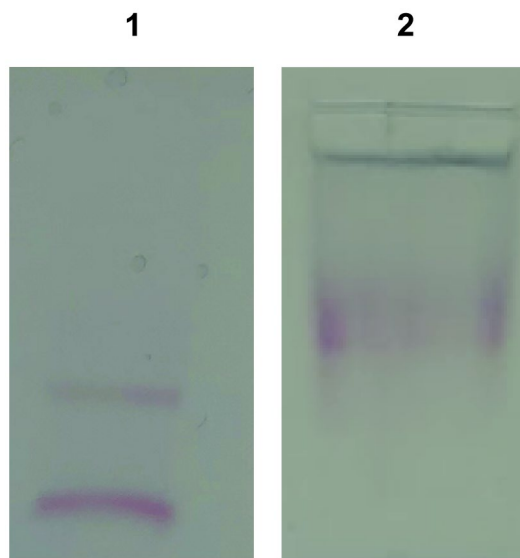
Figure 2.24. Encapsulation of larger fAuNPs. Lane 1: Annealed mixture of cages and 30 nm fAuNPs, where the fast-moving band is unreacted 30 nm fAuNPs, and the slow-moving band the cage-encapsulated 30 nm fAuNPs. Lane 2: Annealed mixture of cages and 50 nm fAuNPs. The absence of well-defined band indicated that the encapsulation was unsuccessful.

2.3.1.4 Binding of the Terminal 30 nm fAuNPs

When 30 nm fAuNPs were mixed with the cage-encapsulated 10 nm fAuNPs, it is pertinent to know if thermal annealing was necessary as repeated annealing might cause structural damages to the cage or the loss of the encapsulated 10 nm fAuNP. We therefore used gel electrophoresis to examine the two mixtures, annealed vs not annealed, and the gel results of the two mixtures were similar (Fig.A3), indicating that thermal annealing was not necessary to bind 30 nm fAuNPs. The relative facile binding might be due to high accessibility of the outside capture strands to the fAuNPs. Moreover, 30 nm fAuNPs captured by the outside capture strands likely experience much less electrostatic repulsions.[32] As the outside and inside strands are orthogonal, there was also no need to purify the cage-encapsulated 10 nm fAuNPs. However, it is pertinent to curb the unwanted aggregations because the outside capture strands were fully exposed to the large fAuNPs (Fig. 2.25). The gel results revealed the importance of adjusting NaCl to 0.30 M after mixing to reduce the aggregations induced by $MgCl_2$. We then mixed 2× large fAuNPs with the cage-encapsulated 10 nm fAuNPs in TAB at room temperature for ~4 hours and characterized the products by gel electrophoresis (Fig.2.26). Like the encapsulation step, large fAuNPs bound to the cage-

encapsulated 10 nm fAuNPs showed slower mobility than the unreacted large fAuNPs, and this slow-moving band also lined up with the fluorescence signal of cage (Fig. A4b); the unreacted 30 nm fAuNP in lane 1 moved a bit slower than neat 30 nm fAuNP in lane 2 due to the staple/fAuNP interactions (Fig.A4a). It is noted that the molar ratio here may not be quantitatively accurate (Fig. 2.27a) because of the assumed cage synthesis yield or inaccurate 30 nm fAuNP concentrations. Nevertheless, it produced qualitative trends as shown in Fig 2.27b where the distribution of resulting species shifted as the nominal molar ratio of the 30 nm fAuNPs to the cage-encapsulated 10 nm fAuNPs was varied from 0.3:1 to 2:1.No unreacted 30 nm AuNPs were observed at a nominal molar ratio of 0.3: 1. Instead, we observed multiple slower moving bands that indicated a heterogenous mixture of species, including possibly a heterodimer species and multimer species that contained four or more fAuNPs (Fig.2.27b). To have additional evidence of the trimer formation, two control experiments were then conducted, including (1) mixing 30 nm fAuNPs and 10 nm fAuNPs (2) adding 30 nm fAuNPs to cages lacking the complementary capture strands (Fig.2.28). Both control experiments showed a single band that is associated with free 30 nm fAuNPs. The band associated with 10 nm fAuNPs, which have much lower extinction coefficient, is too faint to be visible. The gel result in Fig.2.28 showed that (a) in the absence of the DNA origami cage, there was no or very weak interaction between the 30 nm fAuNPs and 10 nm fAuNPs; (b) our design has high binding specificity. Lastly, we performed stability test and the results suggested that our trimer degraded if stored at RT > 2 days, and by accident, we were surprised to find frozen/thawing cycle had little effects on the trimer stability (Fig.2.29), suggesting the trimers may be quickly frozen after synthesis to prolong the shelf life. Nevertheless, to minimize sample degradation, the trimer band in agarose gel was quickly purified and subjected to electron microscopic and plasmonic characterizations.

Figure 2.25. Agarose gel result of 30 nm-10 nm-30 nm trimer assembly without NaCl adjustment.
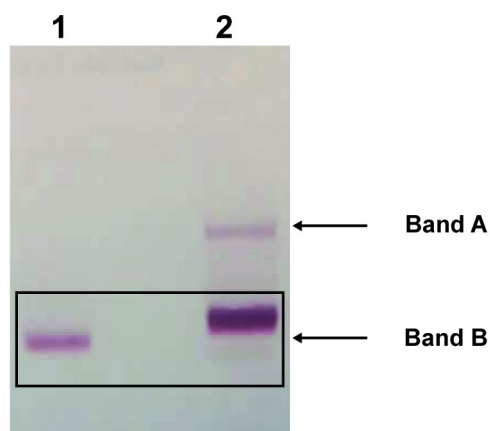
Figure 2.26. Agarose gel results of 30 nm-10 nm-30 nm trimer assembly. Lane 1: Neat 30 nm fAuNPs. Lane 2: Mixture of 30 nm fAuNPs and the cage-encapsulated 10 nm fAuNPs after incubation at RT.
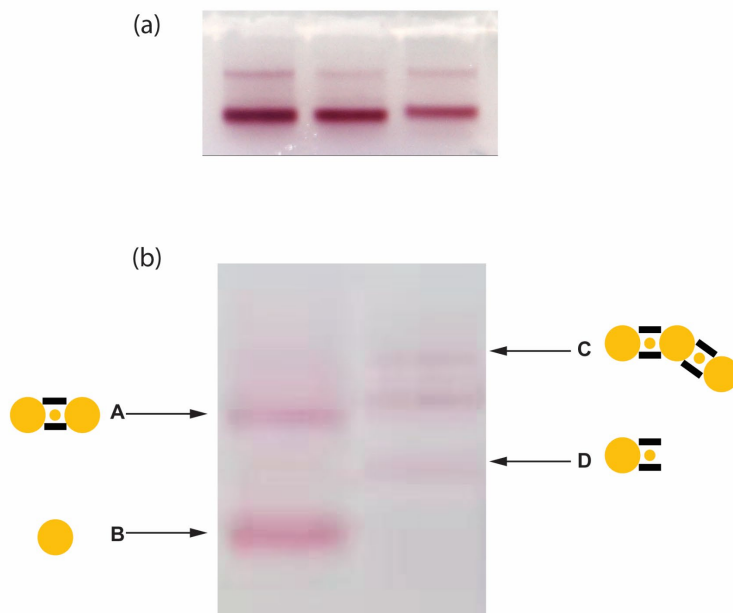
Figure 2.27. Agarose gel results of stoichiometric ratio investigations in trimer assembly.(a) Stoichiometric ratio between 30 nm fAuNPs and the cage-encapsulated 10 nm fAuNPs from left to right: 4:1, 2:1, 1:1. The total amount of 30 nm fAuNP is held constant in each lane. (b) Stoichiometric ratio between 30 nm fAuNPs and cage-encapsulated 10 nm fAuNPs from left to right: 2:1, 0.3:1.
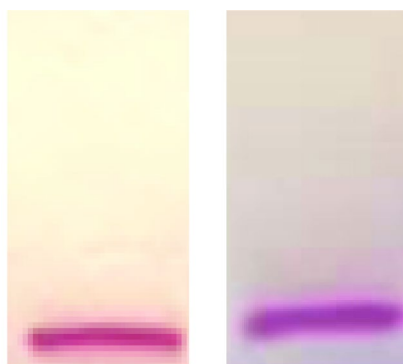
Figure 2.28. Agarose gel results of control experiments in 30 nm- 10 nm -30 nm trimer assembly. Left: Mixture of 10 nm and 30 nm fAuNPs in TAB at molar ratio of 1:2, only 30 nm fAuNPs were visible. Right: Mixture of DNA origami with a different 30 nm fAuNPs that cannot hybridize with outside capture strands, only one unreacted 30 nm fAuNP band was visible.
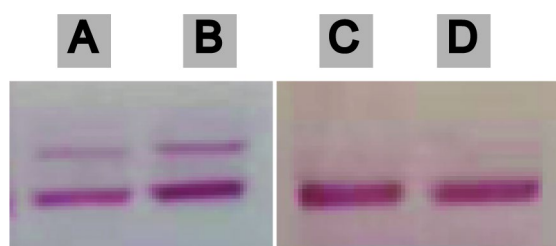
Figure 2.29. Agarose gel results of 30 nm- 10 nm -30 nm trimer stability test. Lanes A,B: 30 nm-10 nm-30 nm trimer subjected to repeated freeze/thaw cycles. Interestingly, the slow-moving were present indicating the trimer was intact. Lanes C,D: 30 nm-10 nm -30 nm trimer at RT for > 48 hours, only 30 nm fAuNP bands were visible indicating the losses of the attached 30 nm fAuNPs.

2.3.2 Structural Analyses of 30 nm-10 nm-30 nm Trimer

Gel electrophoresis showed our trimers were made but provided little structural information of the synthesized trimers. We then used SEM to image the purified 30 nm-10 nm-30 nm trimer and used these SEM micrographs to perform structural analyses. SEM micrograph of a representative structure revealed two large AuNPs (~31 nm) flanking a smaller AuNP (~9 nm) (Fig. 2.30a, more SEM images and size measurements in Fig.A.6 and Table A.5). The surface-sensitive secondary electron image revealed a shell, possibly DNA ligands, DNA origami or residual water, around the heterotrimer structure. The backscattering electron mode resolved the central AuNP more clearly due

to its higher sensitivity to heavy elements. An analysis of 30 nm-10 nm -30 nm trimers found an average 2D projected bending angle (defined as θ in the inset of Fig.2.30b, and the supplementary angle of bond angle) of 9.7°± 6.9. It should be noted that the true bending angles, θ_{3D}, may differ from the 2D projected bending angles, θ. According to equation 3, θ is identical to θ_{3D} only when the plane of the three particles and the plane of the solid support are parallel, i.e., φ, the angle between the two planes is zero.

$$\sin \frac{(180° - \theta)}{2} = \cos \varphi \sin \frac{(180° - \theta_{3D})}{2} \tag{3}$$

Indeed, it is difficult to ascertain the linearity of nanoparticle chains assembled on a 2D DNA origami template as even if the centers of AuNP are not positioned at the same heights above the template (Fig.A.12), [24,42] θ measured by conventional 2D imaging may be zero because the plane of the particles is largely perpendicular to the solid support, i.e., φ =90°, as the deposited 2D template is parallel to the support. In contrast, the small bending angles observed can confirm the linearity of nanoparticle chains assembled by our 3D cage because the structures land on the solid support with a random φ and the nonlinearity is not obscured by a fixed adsorption orientation of the template. Numerical simulation based on equation (3) reproduced the θ distribution by assuming random φ and two populations of $\theta_{3D,}$ one centered at ~6° and the other at ~18° (Fig.A.4). Though most 30 nm-10 nm-30 nm trimers had small bending angles, there were a small fraction of distorted and irregular structures (Fig.A.6). It remains an open question if the distortion was caused by deposition or purification or something else. To obtain accurate bending angles analyses, cryo-EM tomography will be needed to reconstruct the less-damaged structures in 3D.

We then investigated the interparticle gap sizes in our assembled 30 nm-10 nm-30 nm heterotrimers. Our DLS results (Fig.2.21a) and previous simulation suggested the DNA ligand shells of isolated fAuNPs were ~2.5 nm in thickness. As a result, we anticipate the ligand shell-to-ligand shell contact would result in a ~5 nm interparticle gap size. The measured interparticle gap was 3.6±1.5 nm which was close to our prediction and small enough to produce effective plasmonic coupling. Correlation analyses were also performed to investigate how bending angles and sizes of fAuNPs affects the interparticle gap.[44] The spearman's correlation coefficients (ρ) are −0.273, −0.0159, −0.218, −0.130 for Fig.2.31(a)-(d), respectively. The small absolute ρ values here suggested gap size was either weakly correlated (0.2<|ρ|<0.3) or uncorrelated (0.01<|ρ|<0.2) to the bending angle and size of fAuNPs.

Taken together, these SEM results suggest that our cage-mediated approach that uses the synergy of base pairing, size complementarity, and ligand-to-ligand contact can tightly confine constituent nanoparticles. Our new assembly strategy has successfully aligned the centers of constituent nanoparticles of large size differences and minimized the dependence of gap sizes on nanoparticle sizes.

It should be noted that the limited resolution of the SEM (~1 nm at best) and deformation by surface deposition in our measurement may lead to an overestimation of the actual variability in the gap size. Cryo electron tomography would be ideally suited for more accurate determination of the gap size as well as bond angles due to the three-dimensional nature of structural determination, the higher spatial resolution of transmission electron microscopy and minimization of deformation due to flash freezing of the sample.[45] In conclusion, our cage-mediated synthesis approach could produce a linear plasmonic molecule, providing an ideal plasmonic test bed.
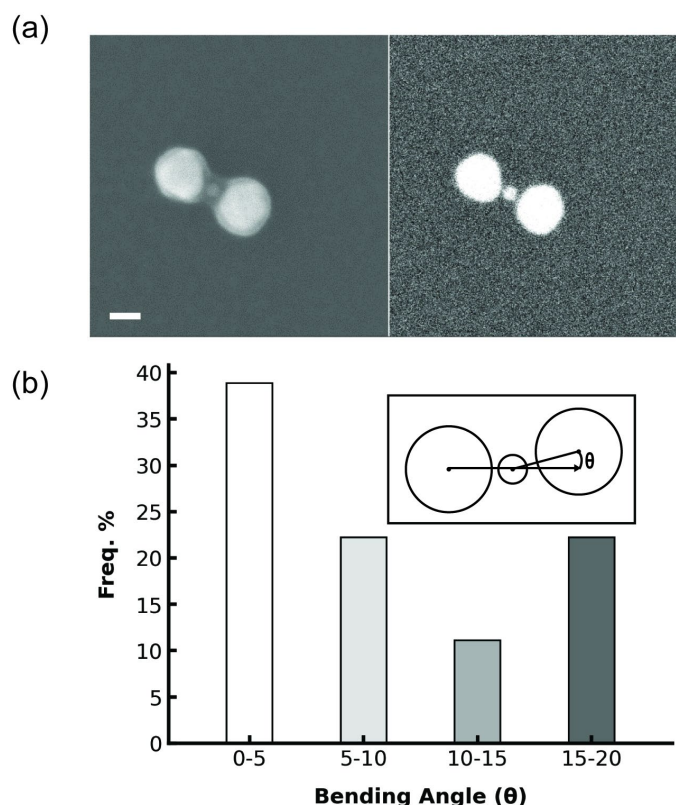
Figure 2.30. Typical SEM images of 30 nm -10 nm -30 nm trimer and bending angle analysis. (a) SEM image. Left: SE (secondary electron) detector Right: BSE (backscattering electron) detector. Scale bar: 20 nm (b) Bending angle distributions. Inset: schematic of the bending angle θ.
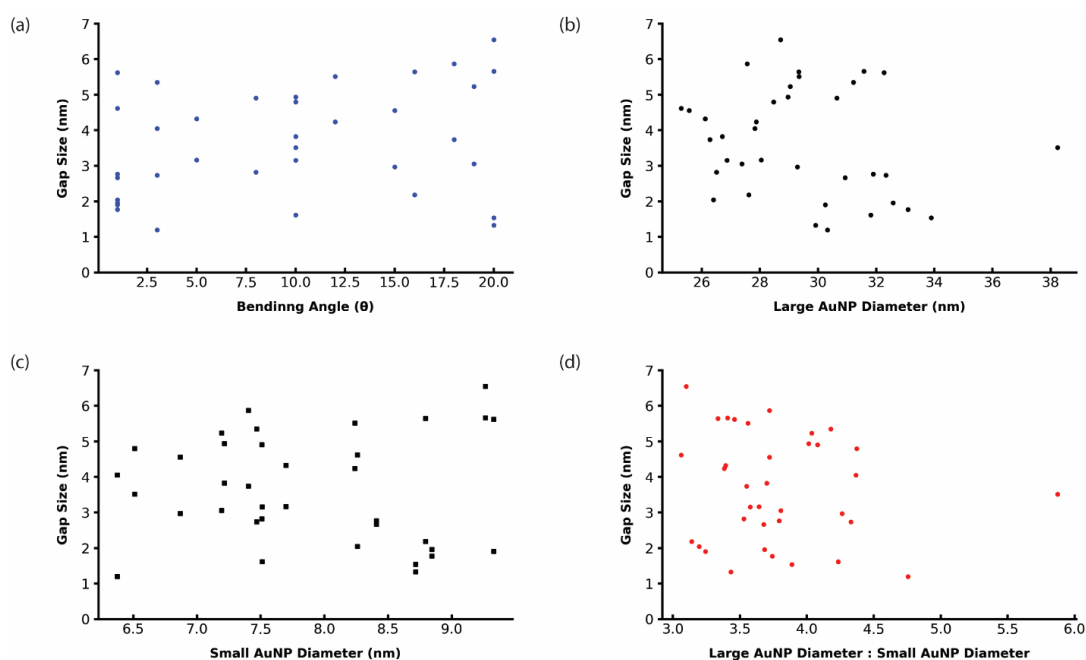
Figure 2.31. Correlation analyses of 30 nm-10 nm-30 nm trimer gap sizes. (a) Gap size versus bending angle. (b) Gap size versus large AuNP diameter. (c) Gap size versus small AuNP diameter. (c) Gap size versus the ratio between large AuNP diameter and small AuNP diameter. All values were extracted from trimer SEM images.

2.3.3 Plasmonic Properties of 30 nm-10 nm-30 nm Trimer

To verify the plasmonic properties of 30 nm-10 nm-30 nm trimers, we performed UV-Vis absorption spectroscopy and SERS measurements. The UV-vis absorption spectrum of the purified 30 nm-10 nm-30 nm trimers in TAB displayed a peak at ~540 nm, as well as a shoulder at ~604 nm, which is not resolved in the spectrum of the unpurified trimer sample (Fig.2.32a) or in the previous studies.[24-25] FDTD simulations of the trimer structures showed that one of LSPR bands originated from the transverse mode (~540 nm) of the heterotrimers, and the other from a longitudinal mode (~610 nm) due to interparticle dipolar plasmonic coupling (Fig.2.32a). The longitudinal LSPR peak in the experimental spectrum is weaker than that in the simulated spectrum (Fig.2.32a), as the trimers in TAB assume random polar and azimuthal angles and only a small fraction are oriented for selective excitation of the longitudinal mode. To determine SERS EF of the heterotrimers, the 10 nm AuNPs were functionalized with DNA ligands that are tagged with a

Raman reporter carboxytetramethylrhodamine (TAMRA). The TAMRA is positioned approximately 2 nm away from the central AuNP to minimize chemical enhancement (Fig.2.33).[11] It is well-known that molecules in the gaps experience the most intense field concentration and SERS enhancements. [10,12,46] Hence, TAMRA molecules in the gap dominate the SERS spectrum. Fig.2.32b showed a typical SERS spectrum of 30 nm-10 nm-30 nm trimers deposited on a solid support using 633 nm excitation laser. Two characteristic TAMRA peaks, 1642 cm^{-1} and 1366 cm^{-1}, can be observed, as highlighted by dashed green lines. A few lower intensity peaks were attributed to the Raman modes of DNA,[47] which have smaller cross sections than TAMRA. After Raman measurements, the amount of TAMRA on the hetero-trimers was determined by fluorimetry.[25,31] The enhancement factors were calculated using equation (4), where I_{SERS} is the SERS intensity of matched TAMRA mode, I_{Raman} is the corresponding Raman intensity of unenhanced bare TAMRA, CSERS is the TAMRA concentration on hetero-trimers, C_{Raman} is the concentration of unenhanced TAMRA.

$$EF = \frac{I_{SERS}}{I_{Raman}} \cdot \frac{C_{Raman}}{C_{SERS}} \qquad\qquad (4)$$

The average hetero-trimer SERS EF, 3.5×10^5, agreed well with the EF simulated by FDTD (2.3×10^5) at 633 nm (Fig.2.32c). While the EF at 633 nm is modest, FDTD simulation predicts a much higher average EF (up to 10^{10}) (Fig.2.37) if the laser wavelength is tuned to the LSPR λ_{max} near 613 nm. We also used 785 nm incident wavelength to excite our 30 nm-10 nm-30 nm trimers, and our average experimental EF at 785 nm was 1.12×10^3 that agreed well with mean simulated EF (Appendix). The small difference between the experimental and simulated plasmonic properties further indicate that our cage enables tailored plasmonic molecule assembly with the desired geometrical arrangement.
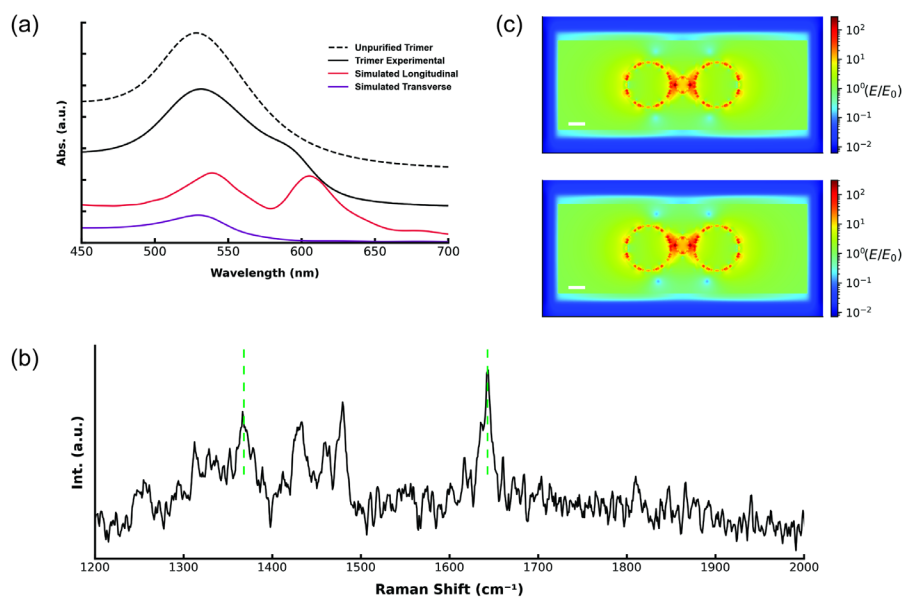
Figure 2.32. Plasmonic properties of 30 nm-10 nm-30 nm trimer. (a) UV-vis absorbance spectra experimental and simulated trimer. (b) SERS spectrum of TAMRA on trimer using 633 nm excitation. (c) FDTD simulations showing the distributions of the local electric field enhancement (E/E_0) of trimers at 633 nm. Top: Trimer with bending angle $\theta=0°$, average SERS EF about 2 nm away from central particle is 5.9×10^5. Bottom: Trimer with bending angle $\theta=10°$, average SERS EF about 2 nm away from central particle is 8.5×10^5. Scale bar: 10 nm.
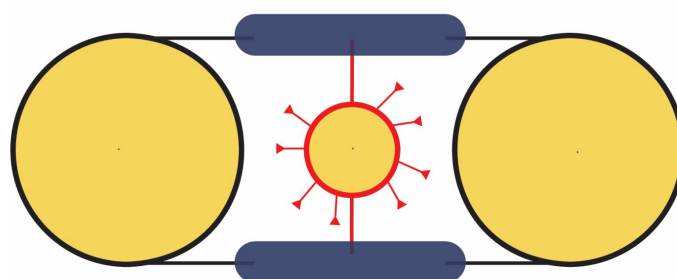
Figure 2.33. Schematic of trimer contains TAMRA-tagged central nanoparticle. Black line: Outside capture strands; Blue round corner square: Origami cage; Red lines with triangle-end: TAMRA-tagged thiolated DNA ligands; Red lines without triangle end: inside capture strands, only two are shown for simplicity.

2.3.4 FDTD Simulations of 30 nm-10 nm-30 nm Trimer

To better understand the plasmonic properties of 30 nm -10 nm -30 nm trimers, a systematic absorption and EF simulations were performed. The simulated transverse absorption spectra were independent of bending angles and gap sizes (Fig.2.34a-b). The trimer with a 10° bending angle only slight deviated from perfectly aligned trimer in simulated longitudinal absorption, while greater deviation and blue shift occurred to the trimer with a 25° bending angle (Fig.2.34c). The longitudinal peak blue-shifted up to 10 nm as gap sizes increased from 3 nm to 5 nm (Fig.2.34d). Besides various polarization angles in experimental measurements, minor gap and bending angle variations in trimer could also produce an absorption spectrum as shown in Fig.2.34a. Custom MATLAB code was used to process exported electric field values from FDTD simulations of the trimers for EF calculations. The mean EF values of 633 nm and 785 nm incident wavelengths were used to plot Fig.2.35. As shown in Fig.2.35a, the trimers with θ of 0° and 10° showed same trends: mean EF decreases as distance to central AuNP surface increases, while the trimer with $\theta = 25°$ had different trend indicating larger deviation from collinearity could alter plasmonic properties of trimer. Interestingly, three trimers show similar trends in Fig.2.35b inferring such trend is sensitive to incident wavelength. The polarization angle of incident light could have large impacts on simulated mean EF as shown in Fig.2.36. While Fig.2.37 revealed that incident wavelengths affected simulated EF values of trimers: mean EF reached the maximum value ($>10^{10}$) at the longitudinal LSPR wavelength (613 nm for $\theta = 0°$ and 10°, 604 nm for $\theta = 25°$) and dropped quickly as the incident wavelength moves away from the LSPR. In contrast, Kleiman et al. [48] observed that the maximum EFs of dimers and multimers with similar-sized AuNPs separated by sub-nanometer gaps are not correlated to the spectral position of LSPR. These contrasting results indicate intriguing opportunities for future theoretical and experimental studies of the plasmonic properties of these hetero-multimers, such as the wavelength dependence of EFs.

Our simulation results implied our model 30 nm-10 nm-30 nm trimer only had ultrahigh EF ($\sim 10^{10}$) at the excitation wavelength 613 nm. However, there are two challenges associated with SERS measurement at this wavelength. On one hand, 613 nm laser is not commonly used for SERS; on the other hand, fluorescence background excited by 613 nm laser would interfere with Raman signals more strongly than that by 633 nm laser.[49] To have practical applications, it is important to make a plasmonic heterotrimer that has high EF at conventional 633 nm laser that produces much weaker fluorescence background. The FDTD simulations of a 50 nm-10 nm-50 nm linear heterotrimer reported nearly 10^8 EF at 633 nm. In addition, although our cage-

mediated assembly approach could successfully make 30 nm-10 nm-30 nm linear heterotrimer, it is still unknown whether our cage could still confine nanoparticles > 30 nm and produce defined gap size and bond angle. As a result, we were eager to see our approach could be extended to make linear 50 nm-10 nm-50 nm trimers, a promising candidate for practical ultrasensitive SERS sensing.
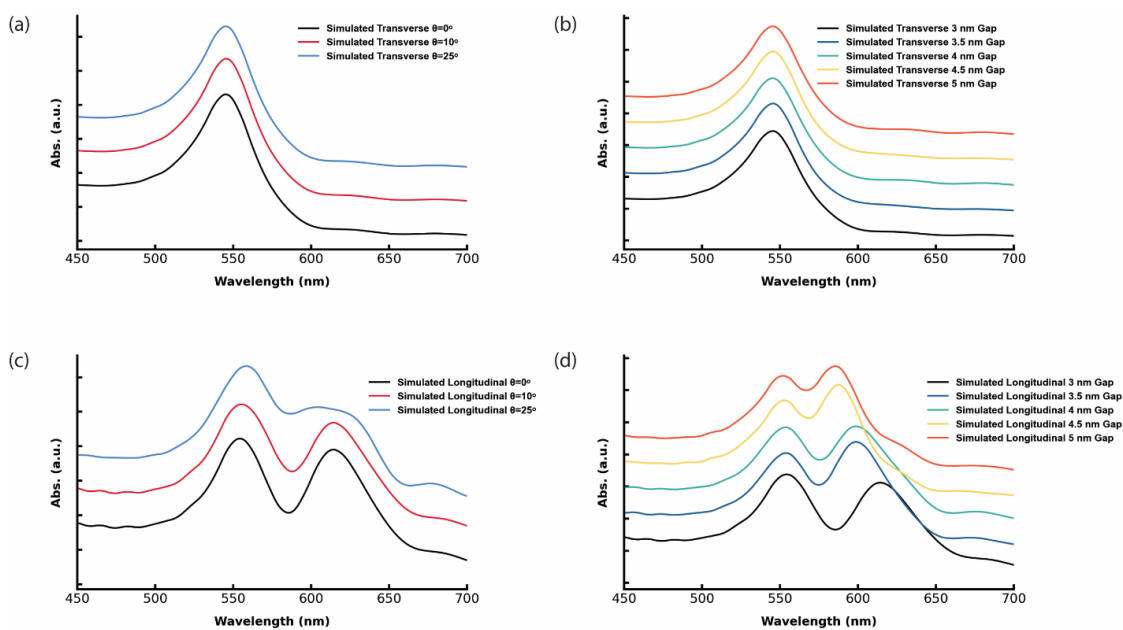
Figure 2.34. Simulated absorption spectra of trimers. (a) Simulated transverse mode of 30 nm-10 nm-30 nm trimers (3 nm gap) with different bending angles. (b) Simulated transverse mode of 30 nm-10 nm-30 nm trimers ($\theta=0°$) with different gaps. (c) Simulated longitudinal mode of 30 nm-10 nm-30 nm trimers (3 nm gap) with different bending angles.
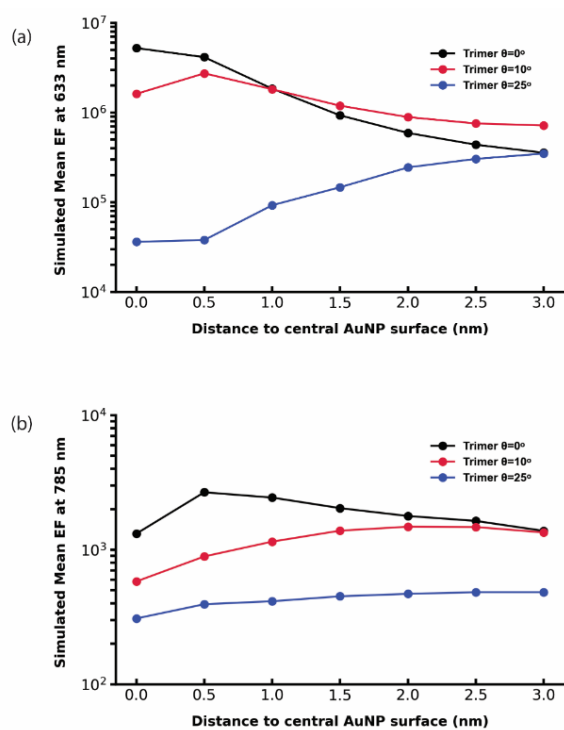
Figure 2.35. Bending angle dependence of simulated EF of trimers. (a) longitudinal excitation at 633 nm. (b) longitudinal excitation at 633 nm. For (a)-(b): 3 nm gap was used for simulations of 30 nm-10 nm-30 nm trimers.
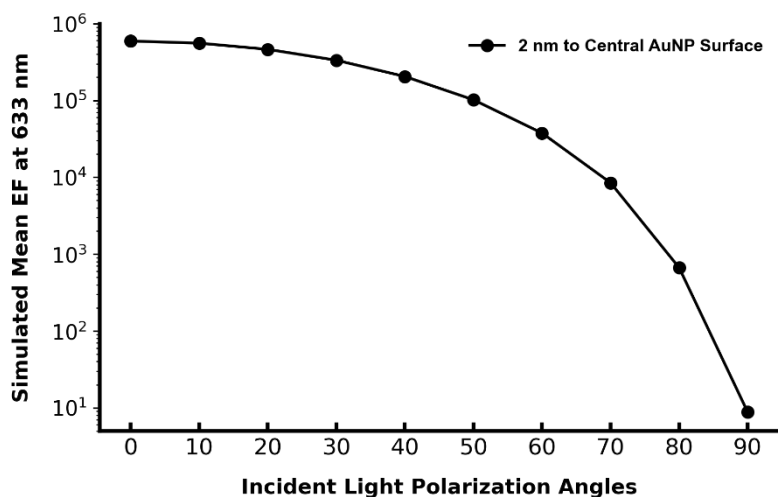
Figure 2.36. Simulated mean EF of trimer versus incident light polarization angles. 3 nm gap was used for simulations of 30 nm-10 nm-30 nm trimer with θ = 0°.
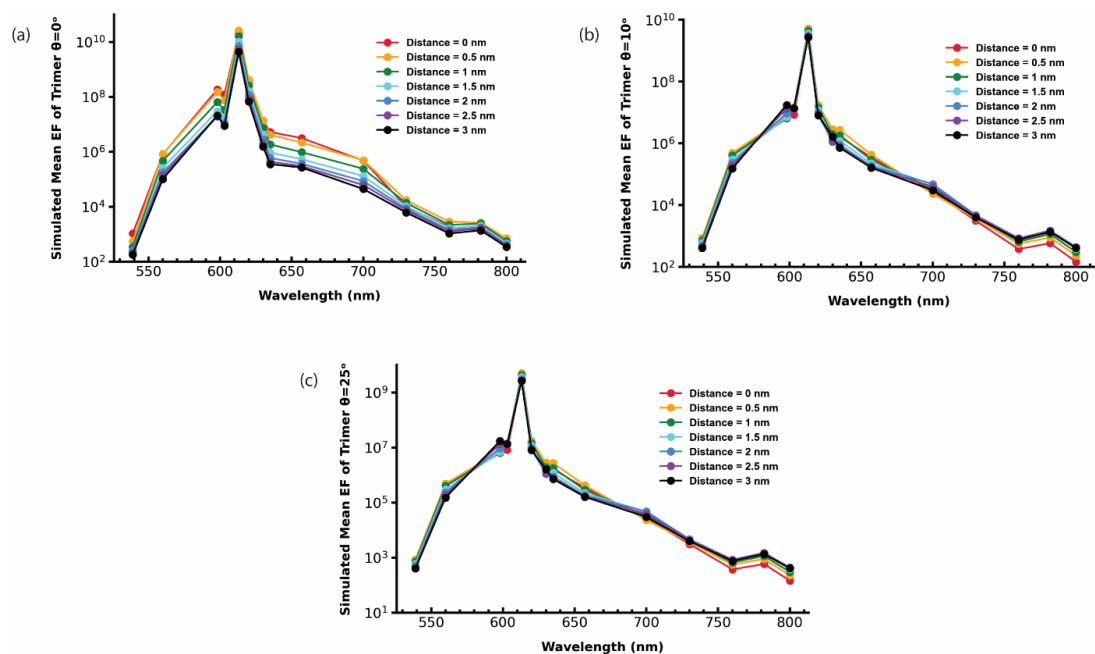
Figure 2.37. Simulated mean wavelength-dependence of EF of trimer. (a) θ = 0° (b) θ=10° (c) θ=25° at different distances from surface of 10 nm AuNP. Electric field polarization is parallel to the longitudinal axis. For (a)-(c): 3 nm gap was used for simulations of 30 nm-10 nm-30 nm trimers.

2.3.5 Synthesis and Analyses of 50 nm-10 nm-50 nm Trimer

The main hurdle for 50 nm-10 nm-50 nm trimer synthesis is to produce proper 50 nm fAuNPs. Unlike its smaller counterparts (10 nm, 30 nm etc.), surface functionalization of 50 nm AuNPs is more challenging. We first used the exact salt-aging protocol for the smaller AuNPs to functionalize 50 nm AuNP, and the resultant fAuNPs showed multiple pink bands in gel (Fig.2.38a), which not only complicated the result interpretations but also made gel characterization and purification of 50 nm-10 nm-50 nm trimer impossible. Therefore, we optimized the salt-aging method for 50 nm AuNPs (Section 2.2.2), [30] and the new 50 nm fAuNPs showed a single band in the gel (Fig.2.38a) and a much smaller electrophoretic mobility than the smaller counterparts (Fig. A.10). It is pertinent to know the species to which the multi-bands correspond, hence, we performed UV-Vis and DLS measurements to analyze the 50 nm fAuNPs using the previous and optimized salt-aging method. If the multi-bands were 50 nm fAuNP multimers, then its UV-Vis spectra would have large red-shifts, and the size-sensitive DLS would display multiple peaks >100 nm. The two 50 nm fAuNP samples had identical UV-Vis absorption spectra (Fig.2.38b); DLS results of 50 nm fAuNP having multi-band showed slightly larger D_h (Fig.2.38c), but no peaks > 100 nm. Therefore, multi-bands are unlikely to be 50 nm fAuNP multimers. We hypothesized 50 nm AuNPs, if not properly functionalized, would have populations with various DNA ligand surface densities giving rise to multi-bands in gel. After 50 nm fAuNPs showing mono-band in gel were made, we could synthesize 50 nm-10 nm-50 nm trimers and perform purification and characterizations.

The gel results (Fig.2.39) of the mixture of 50 nm fAuNPs and the cage-encapsulated 10 nm fAuNPs showed a clear slow-migrating pink band lined up with the fluorescence signal of the DNA origami cage, indicating the successful assembly of the 50 nm-10 nm-50 nm trimer. The band of interest was selected for purification and the purified samples were examined by SEM. SEM micrographs of representative structures are shown in Fig 2.40. Structural analyses revealed that 50 nm-10 nm-50 nm trimers had large bending angles 60.7°± 20.0 and ~4 nm interparticle gap size (More size measurements in Table. A.6). It is noted that the gap size determinations may be inaccurate because of the significant distortion of 50 nm-10 nm-50 nm trimers.

In contrast to our anticipations, the bending angle was in fact affected by the size of nanoparticles. Drying effects of sample deposition could alter the nanostructures,[50] however, such distortions were not seen in our model 30 nm -10 nm-30 nm trimers indicating drying effects were at least not the main culprit of structural distortions. As nanoparticles get larger, the van der Waals

attractions between nanoparticles increase.[19] We hypothesized the strong van der Waals attractions between large 50 nm fAuNPs caused significant cage deformations. The deformed cage, however, couldn't keep the assembled nanoparticle in a straight line. We also performed SERS measurements of dried 50 nm-10 nm-50 nm trimer at 633 nm. The SERS spectrum differed from that of our model 30 nm-10 nm-30 nm trimers (Fig2.32c). The characteristic TAMRA peak at1642 cm^{-1} was absent in Fig.2.41a, two TAMRA peaks, 1223 cm^{-1} and 1366 cm^{-1} (marked by dashed red lines), could be observed, and the calculated EF was about 10^4, which was over 4 magnitudes lower than the simulated EF (Fig.2.41b). The low EF further confirmed the dried 50 nm -10 nm -50 nm trimer were highly distorted. We last conducted UV-Vis absorption spectroscopy of 50 nm-10 nm-50 nm trimers in TAB. Surprisingly, the absorption spectra of neat 50 nm fAuNP and purified 50 nm-10 nm-50 nm trimers showed nearly identical feature (Fig.2.41c), which differed greatly from the simulated liner 50 nm-10 nm-50 nm trimer spectra (Fig.2.40d). The absence of strong plasmonic coupling in the 50 nm-10 nm-50 nm trimers suggested the structural distortions might also present in solution. Taken together, the distortions of 50 nm-10 nm-50 nm trimers were likely present with or without drying. The distorted 50 nm-10 nm-50 nm trimers infer that our cage needs to be redesigned to minimize the impacts of the van der Waals attraction. The high programmability of DNA makes the cage re-design straightforward;[51] the distortion might be reduced by adding more DNA layers, changing opening sizes, and/or incorporating more outside capture strands. To initiate rational cage re-design to minimize such deformation, cryo-EM will be needed to assess the nanostructures without the drying process.
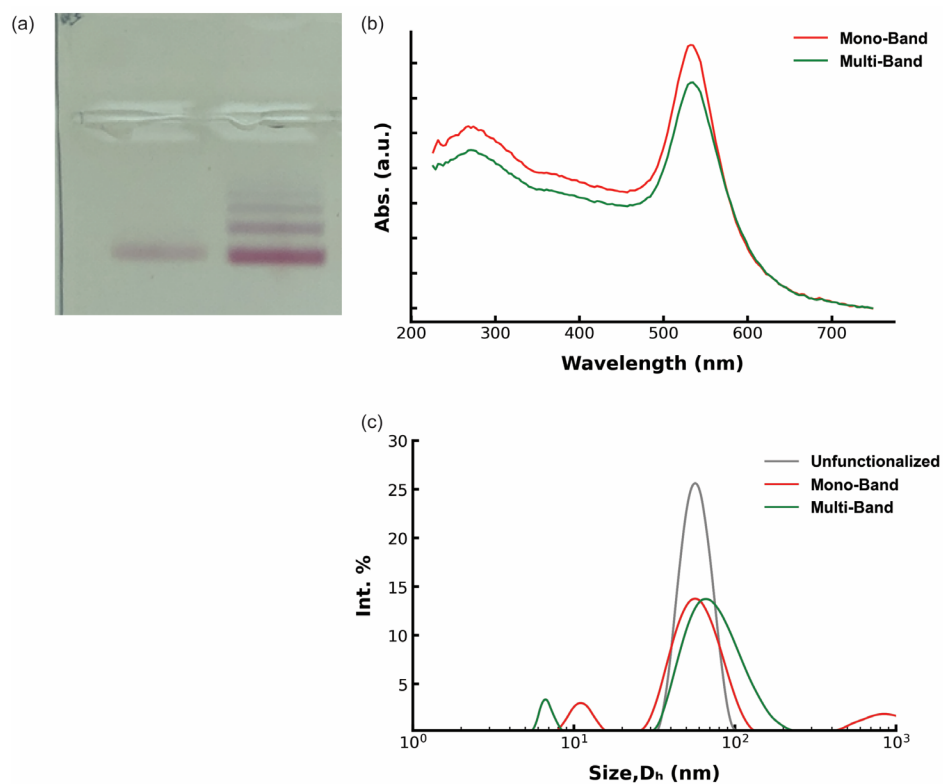
Figure 2.38. Characterizations of 50 nm fAuNPs. (a) Agarose gel results of 50 nm fAuNP using different salt-aging methods. Left: Optimized salt-aging method. Right: Non-optimized salt-aging method. (b) UV-vis absorption spectra of 50 nm fAuNP showing one band or multiple bands. (c) DLS results of unfunctionalized 50 nm AuNPs and 50 nm fAuNPs showing one band or multiple bands.
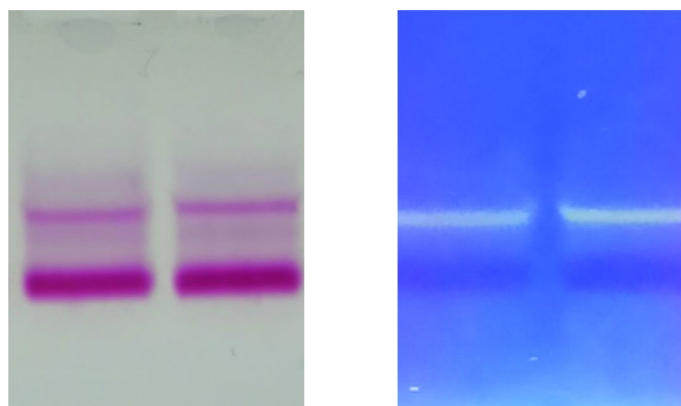
Figure 2.39. Agarose gel characterization of 50 nm-10 nm-50 nm trimers. Left: Mixture of 50 nm fAuNPs and the cage-encapsulated 10 nm fAuNPs, the fast-migrating band is unreacted 50 nm fAuNP and the slow-moving band the assembled trimer. Right: Same as left but under UV-vis excitation, the fluorescence signal (yellow-green band) of cage on the right lined up with the slow-moving pink band on the left.
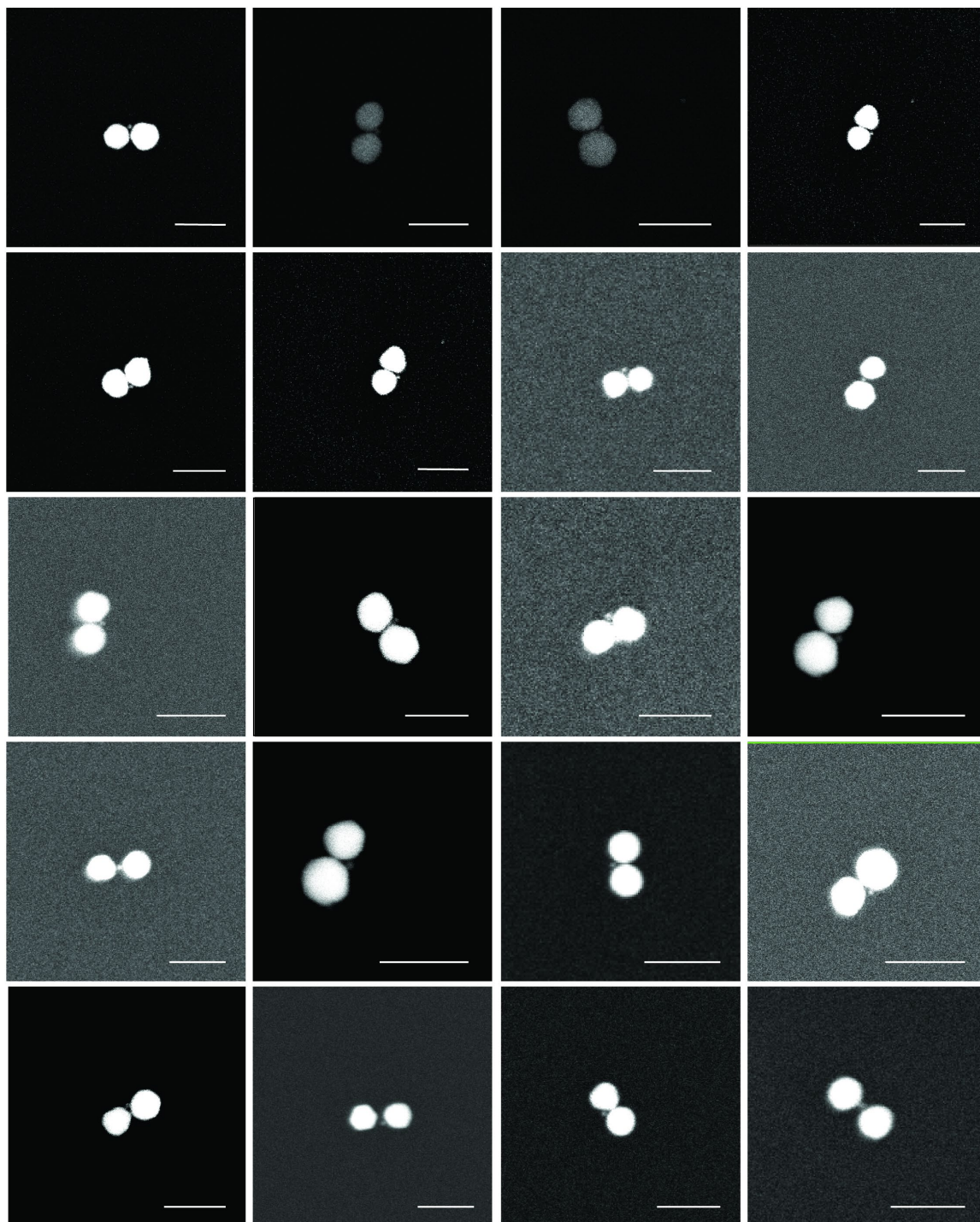
Figure 2.40. SEM images of 50 nm-10 nm-50 nm trimers. Backscattering detector was used. Scale bar: 100 nm.
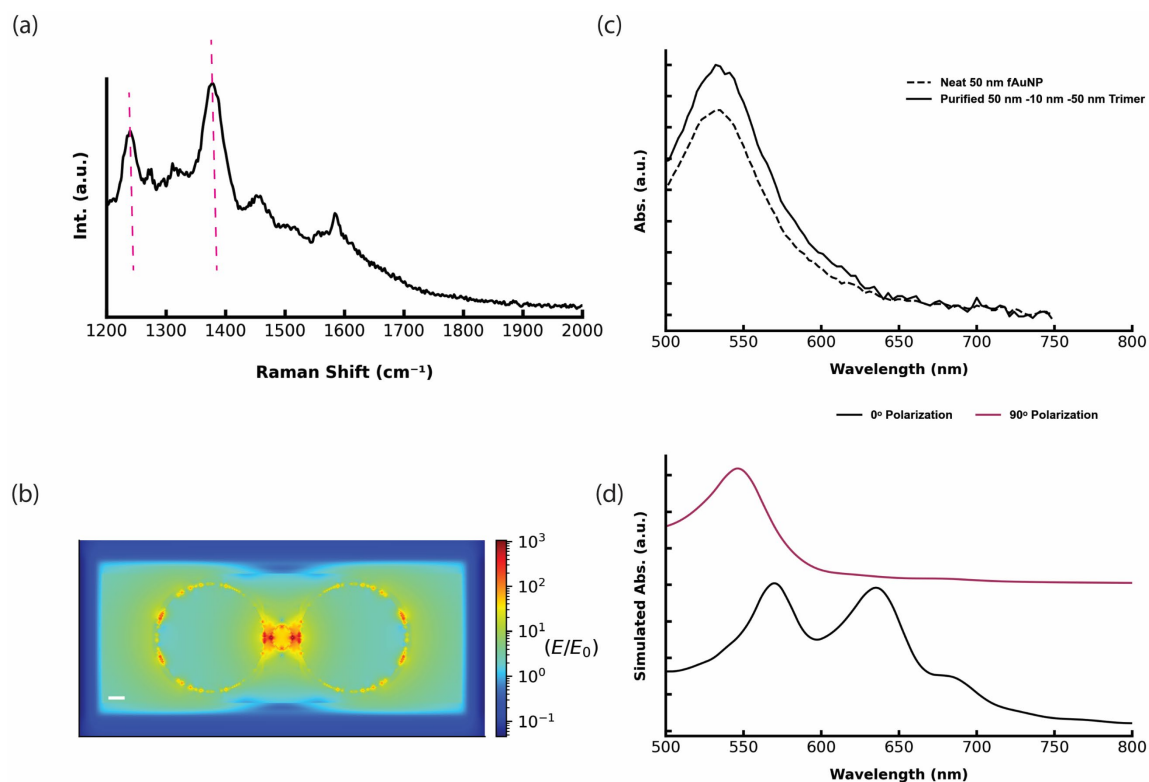
Figure 2.41. Plasmonic properties of 50 nm-10 nm -50 nm trimer. (a) SERS spectrum of TAMRA on 50 nm-10 nm-50 nm trimer using 633 nm excitation. (b) FDTD simulations showing the distributions of the local electric field enhancement (E/E$_0$) of trimers at 633 nm, bending angle θ=0°, gap size= 4 nm, average SERS EF about 2 nm away from central particle is ~10^9. (c) UV-vis absorbance spectra of neat 50 nm fAuNP and purified 50 nm -10 nm -50 nm trimer. (d) Simulated absorption spectra of 50 nm-10 nm-50 nm trimer with 0° and 90° polarization angles.

2.3.6 Preliminary Data of 30 nm-10 nm-50 nm Trimer

After our attempts on two symmetric trimers, the next goal was to test the programmability of our D-DOC assembly strategy by assembling asymmetric 30 nm-10 nm-50 nm trimers through re-designing the outside captures strands. It is worth mentioning that our 30 nm-10 nm-50 nm trimer showed an average nearly 10^{10} simulated average EF at 633 nm excitation wavelength, such high EF, if true, could enable single molecule detection (Fig.2.43). The asymmetric trimer requires the two terminal fAuNPs, the overall synthesis steps might differ from those of the other two trimers. Fig.2.42 contained preliminary data of gel and SEM characterizations of 30 nm-10 nm -50 nm asymmetric trimers. The synthesis of asymmetric trimer was not optimized

shown as smear in Fig. 2.42a. The lack of enough SEM micrographs limited the structural analysis of the asymmetric trimers. Nonetheless, the preliminary SEM images (Fig.2.42b) showed such asymmetric trimer with large bending angles, which suggest that the presence of 50 nm fAuNP may be responsible for the observed large distortions. Further optimization of trimer synthesis is required for systematic structural and plasmonic analyses. cryo-EM/tomography will provide insight into the cause of the deformation and inform the optimization of the assembly process and DNA origami cage design.

(a)

(b)
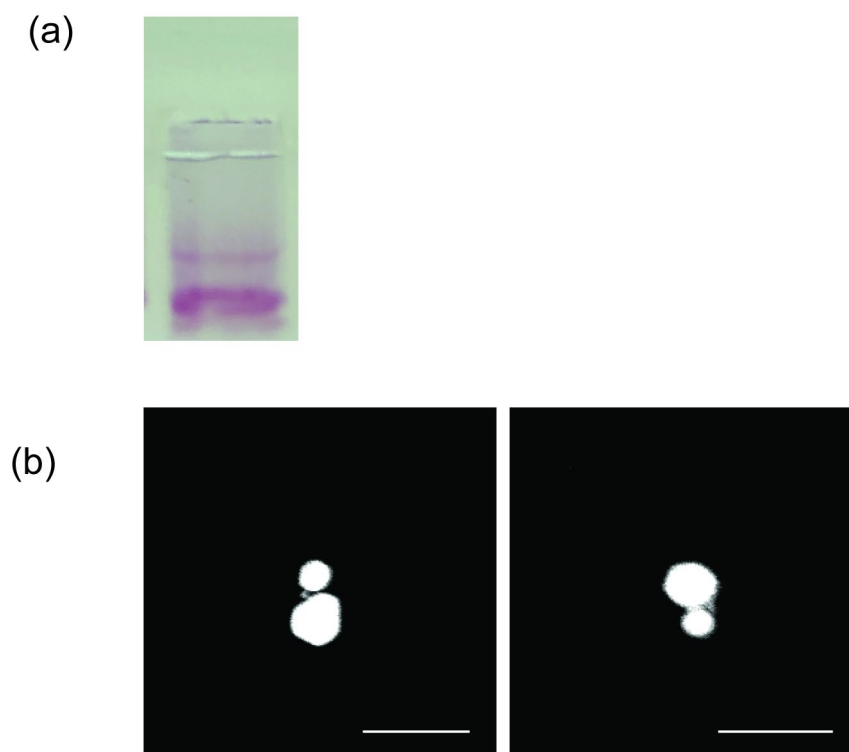
Figure 2.42. Characterizations of 30 nm-10 nm -50 nm trimers. (a) Agarose gel result of mixture of 30 nm, 50 nm fAuNPs and the cage-encapsulated 10 nm fAuNPs. (b) SEM images of 30 nm-10 nm-50 nm trimers. Backscattering detector was used. Scale bar: 100 nm.
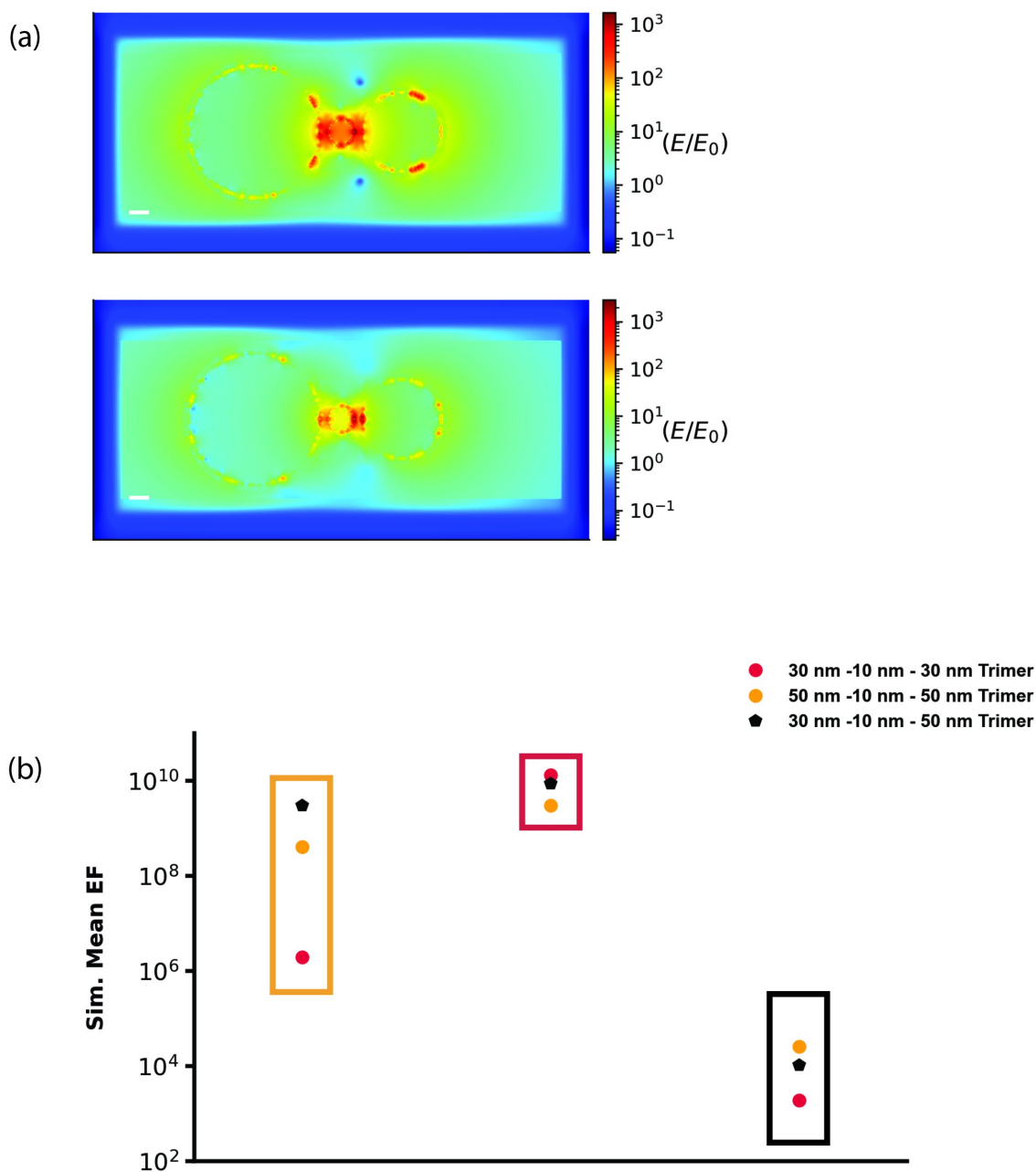
Figure 2.43. Compiled FDTD simulations of three trimers. (a) Simulated electric fields of 30 nm-10 nm-50 nm trimer (θ=0°, gap size= 3 nm) at 620 nm (top) and 633 nm (bottom) excitation wavelengths, both showed the maximum EF over 10^{12} EF. Scale bar: 10 nm. (b) Simulated mean EF comparisons. Inside yellow square: Simulated EF values at excitation wavelength 633 nm. Inside black square: Simulated EF values at excitation wavelength 785 nm. Inside red square: The maximum simulated EF values. All simulations have longitudinal electric field polarization.

2.4　Conclusion and Future Directions

In conclusion, our new D-DOC binding strategy and cage-mediated approach could precisely define with bond angle and gap sizes of alternating 10 nm and 30 nm fAuNPs making linear plasmonic trimeric molecules. Furthermore, our assembled model plasmonic molecules displayed plasmonic properties matching the simulation results, which were unobtainable using the other existing approaches. Current research is underway to create more complex plasmonic molecules such as a plasmonic nanolens (Fig.2.44a) that has proposed cascading enhancements,[28,52] and a plasmonic heterotrimer comprising of hollow gold nanospheres (HGN) showing octopolar plasmonic modes in simulations (Fig. 2.44b,[53] more experimental data of HGN are in Fig.A.9).[54-55] Such plasmonic molecules could not only be good candidates for practical ultrasensitive detections and but also potent tools for fundamental plasmonic theory validations. We anticipate optimized synthesis and cage design with the aid of cryo-EM and tomography will enable better confinements of nanoparticles >30 nm. Moreover, another way to improved signal reproducibility in ultrasensitive sensing is to localize target analytes near the inter-particle gap,[12,56-58] which could be achieved using our programmable trimers. In principle, binding sites can be added to the relatively wide gaps (hot spots) in our assembled trimers (Fig.2.45a). A current limitation of these plasmonic molecules is their low mechanical, chemical and thermal stability. Recently methods have been developed to encapsulate these DNA templated structures in mesoporous silica. [59-61] Therefore, we expect that the assembled trimers could also be coated with mesoporous silica to enhance the overall structural stability while allowing analytes to enter the hot spots (Fig.2.45b). Ultimately, our work presented here laid the groundwork for synthesis of plasmonic molecules with defined bond angle and gap size, paving the way for practical plasmonic ultrasensitive sensing and beyond.
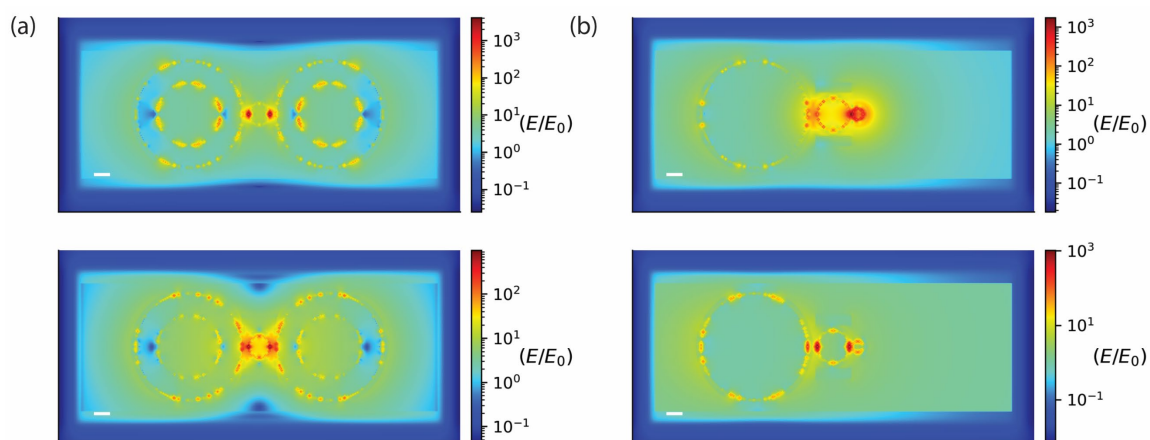
Figure 2.44. FDTD simulations of other linear plasmonic heterotrimers. (a) 10 nm fAuNP flanked by two 50 nm HGNs (shell thickness = 10 m), excitation wavelengths of 646 nm (top) and 633 nm (bottom). Octupole modes appear when excited at 646 nm. (b) 30 nm-10 nm-5 nm nanolens excited at 603 nm (top) and 633 nm (bottom), from left to right: gap sizes are 6 nm and 3 nm respectively. All simulations have longitudinal electric field polarization.
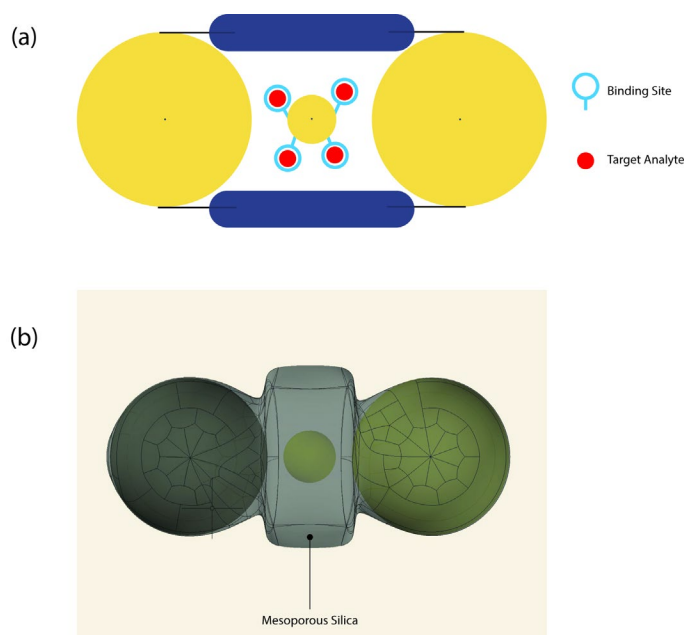
Figure 2.45. Schematic of future designs.(a) Incorporate binding sites to the central particle, black line: outside capture strands, blue round corner square: origami cage. Inside capture strands are omitted for simplicity. (b) Coating trimer with mesoporous silica to enhance structural stability.

Reference

(1) Prodan, E.; Radloff, C.; Halas, N. J.; Nordlander, P. A Hybridization Model for the Plasmon Response of Complex Nanostructures. *Science* **2003**, *302* (5644), 419-422.

(2) Nordlander, P.; Oubre, C.; Prodan, E.; Li, K.; Stockman, M. I. Plasmon hybridization in nanoparticle dimers. *Nano Letters* **2004**, *4* (5), 899-903.

(3) Jain, P. K.; El-Sayed, M. A. Plasmonic coupling in noble metal nanostructures. *Chemical Physics Letters* **2010**, *487* (4-6), 153-164.

(4) Haran, G.; Chuntonov, L. Artificial Plasmonic Molecules and Their Interaction with Real Molecules. *Chemical Reviews* **2018**, *118* (11), 5539-5580.

(5) Willets, K. A.; Van Duyne, R. P. Localized Surface Plasmon Resonance Spectroscopy and Sensing. *Annual Review of Physical Chemistry* **2007**, *58* (1), 267-297.

(6) Brown, L. V.; Sobhani, H.; Lassiter, J. B.; Nordlander, P.; Halas, N. J. Heterodimers: plasmonic properties of mismatched nanoparticle pairs. *ACS nano* **2010**, *4* (2), 819-832.

(7) Xu, Z.; Hou, Y.; Sun, S. Magnetic core/shell Fe3O4/Au and Fe3O 4/Au/Ag nanoparticles with tunable plasmonic properties. *Journal of the American Chemical Society* **2007**, *129* (28), 8698-8699.

(8) Merg, A. D.; Boatz, J. C.; Mandal, A.; Zhao, G. P.; Mokashi-Punekar, S.; Liu, C.; Wang, X. T.; Zhang, P. J.; van der Wel, P. C. A.; Rosi, N. L. Peptide-Directed Assembly of Single-Helical Gold Nanoparticle Superstructures Exhibiting Intense Chiroptical Activity. *Journal of the American Chemical Society* **2016**, *138* (41), 13655-13663.

(9) Unser, S.; Bruzas, I.; He, J.; Sagle, L. Localized Surface Plasmon Resonance Biosensing: Current Challenges and Approaches. *Sensors* **2015**, *15* (7), 15684-15716.

(10) Stranahan, S. M.; Willets, K. A. Super-resolution Optical Imaging of Single-Molecule SERS Hot Spots. *Nano Letters* **2010**, *10* (9), 3777-3784.

(11) Le Ru, E. C.; Etchegoin, P. G. Single-Molecule Surface-Enhanced Raman Spectroscopy. *Annual Review of Physical Chemistry* **2012**, *63* (1), 65-87.

(12) Langer, J.; de Aberasturi, D. J.; Aizpurua, J.; Alvarez-Puebla, R. A.; Auguié, B.; Baumberg, J. J.; Bazan, G. C.; Bell, S. E. J.; Boisen, A.; Brolo, A. G.; et al. Present and future of surface-enhanced Raman scattering. *ACS Nano* **2020**, *14* (1), 28-117.

(13) Cheng, Y.; Stakenborg, T.; Van Dorpe, P.; Lagae, L.; Wang, M.; Chen, H.; Borghs, G. Fluorescence near gold nanoparticles for DNA sensing. *Analytical Chemistry* **2011**, *83* (4), 1307-1314.

(14) Giannini, V.; Fernandez-Dominguez, A. I.; Heck, S. C.; Maier, S. A. Plasmonic Nanoantennas: Fundamentals and Their Use in Controlling the Radiative Properties of Nanoemitters. *Chemical Reviews* **2011**, *111* (6), 3888-3912, Review.

(15) Lee, S.; Sim, K.; Moon, S. Y.; Choi, J.; Jeon, Y.; Nam, J.-M.; Park, S.-J. Controlled Assembly of Plasmonic Nanoparticles: From Static to Dynamic Nanostructures. *Advanced Materials* **2021**, *33* (46), 2007668.

(16) Fan, J. A.; Wu, C.; Bao, K.; Bao, J.; Bardhan, R.; Halas, N. J.; Manoharan, V. N.; Nordlander, P.; Shvets, G.; Capasso, F. Self-Assembled Plasmonic Nanoparticle Clusters. *Science* **2010**, *328* (5982), 1135-1138.

(17) Lloyd, J. A.; Ng, S. H.; Liu, A. C. Y.; Zhu, Y.; Chao, W.; Coenen, T.; Etheridge, J.; Gomez, D. E.; Bach, U. Plasmonic Nanolenses: Electrostatic Self-Assembly of Hierarchical Nanoparticle Trimers and Their Response to Optical and Electron Beam Stimuli. *Acs Nano* **2017**, *11* (2), 1604-1612.

(18) Wang, Y.; Wang, Y.; Breed, D. R.; Manoharan, V. N.; Feng, L.; Hollingsworth, A. D.; Weck, M.; Pine, D. J. Colloids with valence and specific directional bonding. *Nature* **2012**, *491* (7422), 51-55.

(19) Barrow, S. J.; Funston, A. M.; Wei, X.; Mulvaney, P. DNA-directed self-assembly and optical properties of discrete 1D, 2D and 3D plasmonic structures. *Nano Today* **2013**, *8* (2), 138-167.

(20) Alivisatos, A.; Johnsson, K.; Peng, X.; Wilson, T.; Loweth, C.; Bruchez, M.; Schultz, P. Organization of 'nanocrystal molecules' using DNA. *Nature* **1996**, *382* (6592), 609-611.

(21) Lee, H.; Kim, G. H.; Lee, J. H.; Kim, N. H.; Nam, J. M.; Suh, Y. D. Quantitative Plasmon Mode and Surface-Enhanced Raman Scattering Analyses of Strongly Coupled Plasmonic Nanotrimers with Diverse Geometries. *Nano Letters* **2015**, *15* (7), 4628-4636.

(22) Yao, G.; Li, J.; Li, Q.; Chen, X.; Liu, X.; Wang, F.; Qu, Z.; Ge, Z.; Narayanan, R. P.; Williams, D.; et al. Programming nanoparticle valence bonds with single-stranded DNA encoders. *Nature Materials* **2020**, *19* (7), 781-788.

(23) Endo, M. *DNA Origami: Structures, Technology, and Applications | Wiley*.

(24) Ding, B.; Deng, Z.; Yan, H.; Cabrini, S.; Zuckermann, R.; Bokor, J. Gold Nanoparticle Self-Similar Chain Structure Organized by DNA Origami. *Journal of the American Chemical Society* **2010**, *132* (10), 3248-3249, Article.

(25) Heck, C.; Prinz, J.; Dathe, A.; Merk, V.; Stranik, O.; Fritzsche, W.; Kneipp, J.; Bald, I. Gold Nanolenses Self-Assembled by DNA Origami. *ACS Photonics* **2017**, *4* (5), 1123-1130.

(26) Nelson, P. C.; Zurla, C.; Brogioli, D.; Beausang, J. F.; Finzi, L.; Dunlap, D. Tethered Particle Motion as a Diagnostic of DNA Tether Length. *The Journal of Physical Chemistry B* **2006**, *110* (34), 17260-17267.

(27) Wei, X.; Nangreave, J.; Jiang, S.; Yan, H.; Liu, Y. Mapping the Thermal Behavior of DNA Origami Nanostructures. *Journal of the American Chemical Society* **2013**, *135* (16), 6165-6176.

(28) Li, K. R.; Stockman, M. I.; Bergman, D. J. Self-similar chain of metal nanospheres as an efficient nanolens. *Physical Review Letters* **2003**, *91* (22), Article.

(29) Castro, C. E.; Kilchherr, F.; Kim, D. N.; Shiao, E. L.; Wauer, T.; Wortmann, P.; Bathe, M.; Dietz, H. A primer to scaffolded DNA origami. *Nature Methods* **2011**, *8* (3), 221-229.

(30) Liu, B.; Liu, J. Methods for preparing DNA-functionalized gold nanoparticles, a key reagent of bioanalytical chemistry. *Anal. Methods* **2017**, *9* (18), 2633-2643.

(31) Hurst, S.; Lytton-Jean, A.; Mirkin, C. Maximizing DNA loading on a range of gold nanoparticle sizes. *Analytical Chemistry* **2006**, *78* (24), 8313-8318.

(32) Zhao, Z.; Jacovetty, E.; Liu, Y.; Yan, H. Encapsulation of Gold Nanoparticles in a DNA Origami Cage. *Angewandte Chemie-International Edition* **2011**, *50* (9), 2041-2044.

(33) Sinden, R. R. *DNA Structure and Function*; Elsevier Science, 1994.

(34) Stahl, E.; Martin, T. G.; Praetorius, F.; Dietz, H. Facile and scalable preparation of pure and dense DNA origami solutions. *Angewandte Chemie - International Edition* **2014**, *53* (47), 12735-12740.

(35) Shaw, A.; Benson, E.; Högberg, B. Purification of Functionalized DNA Origami Nanostructures. *ACS Nano* **2015**, *9* (5), 4968-4975.

(36) Wagenbauer, K. F.; Engelhardt, F. A. S.; Stahl, E.; Hechtl, V. K.; Stömmer, P.; Seebacher, F.; Meregalli, L.; Ketterer, P.; Gerling, T.; Dietz, H. How We Make DNA Origami. *ChemBioChem* **2017**, *18* (19), 1873-1885.

(37) Bellot, G.; McClintock, M.; Lin, C.; Shih, W. Recovery of intact DNA nanostructures after agarose gel-based separation. *Nature Methods* **2011**, *8* (3), 192-194, Letter.

(38) Thacker, V. V.; Herrmann, L. O.; Sigle, D. O.; Zhang, T.; Liedl, T.; Baumberg, J. J.; Keyser, U. F. DNA origami based assembly of gold nanoparticle dimers for surface-enhanced Raman scattering. *Nature Communications* **2014**, *5*, 3448-3448.

(39) Hermans, T. M. Multi-step non-covalent pathways to supramolecular systems. Phd Thesis 1 (Research TU/e / Graduation TU/e), Technische Universiteit Eindhoven, Eindhoven, 2010.

(40) Martin, T. G.; Dietz, H. Magnesium-free self-assembly of multi-layer DNA objects. *Nature Communications* **2012**, *3*, 1103-1106.

(41) Kopielski, A.; Schneider, A.; Csáki, A.; Fritzsche, W. Isothermal DNA origami folding: avoiding denaturing conditions for one-pot, hybrid-component annealing. *Nanoscale* **2015**, *7* (5), 2102-2106.

(42) Helmi, S.; Ziegler, C.; Kauert, D. J.; Seidel, R. Shape-Controlled Synthesis of Gold Nanostructures Using DNA Origami Molds. *Nano Letters* **2014**, *14* (11), 6693-6698.

(43) Ke, Y.; Sharma, J.; Liu, M.; Jahn, K.; Liu, Y.; Yan, H. Scaffolded DNA origami of a DNA tetrahedron molecular container. *Nano Letters* **2009**, *9* (6), 2445-2447.

(44) Daniel, W. W. *Applied Nonparametric Statistics*; PWS-KENT Pub., 1990.

(45) Zhang, L.; Lei, D.; Smith, J.; Zhang, M.; Tong, H.; Zhang, X.; Lu, Z.; Liu, J.; Alivisatos, A.; Ren, G. Three-dimensional structural dynamics and fluctuations of DNA-nanogold conjugates by individual-particle electron tomography. *Nature Communications* **2016**, *7*, 11083, Article.

(46) Jiang, J.; Bosnick, K.; Maillard, M.; Brus, L. Single molecule Raman spectroscopy at the junctions of large Ag nanocrystals. *Journal of Physical Chemistry B* **2003**, *107* (37), 9964-9972.

(47) Barhoumi, A.; Zhang, D.; Tam, F.; Halas, N. J. Surface-Enhanced Raman Spectroscopy of DNA. *Journal of the American Chemical Society* **2008**, *130* (16), 5523-5529.

(48) Kleinman, S.; Sharma, B.; Blaber, M.; Henry, A.; Valley, N.; Freeman, R.; Natan, M.; Schatz, G.; Van Duyne, R. Structure Enhancement Factor Relationships in Single Gold Nanoantennas by Surface-Enhanced Raman Excitation Spectroscopy. *Journal of the American Chemical Society* **2013**, *135* (1), 301-308, Article.

(49) Le Ru, E. C.; Etchegoin, P. G. Quantifying SERS enhancements. *MRS Bulletin* **2013**, *38* (8), 631-640.

(50) Rudolph, A. R.; Jungjohann, K. L.; Wheeler, D. R.; Brozik, S. M. Drying Effect Creates False Assemblies in DNA-Coated Gold Nanoparticles as Determined Through In Situ Liquid Cell STEM. *Microscopy and Microanalysis* **2014**, *20* (2), 437-444.

(51) Rothemund, P. W. K. Folding DNA to create nanoscale shapes and patterns. *Nature* **2006**, *440* (7082), 297-302.

(52) Li, K.; Stockman, M. I.; Bergman, D. J. Enhanced second harmonic generation in a self-similar chain of metal nanospheres. *Physical Review B - Condensed Matter and Materials Physics* **2005**, *72* (15), 1-4.

(53) Genç, A.; Patarroyo, J.; Sancho-Parramon, J.; Bastús, N. G.; Puntes, V.; Arbiol, J. Hollow metal nanostructures for enhanced plasmonics: Synthesis, local plasmonic properties and applications. *Nanophotonics* **2017**, *6* (1), 193-213.

(54) Schwartzberg, A. M.; Olson, T. Y.; Talley, C. E.; Zhang, J. Z. Synthesis, characterization, and tunable optical properties of hollow gold nanospheres. *Journal of Physical Chemistry B* **2006**, *110* (40), 19935-19944.

(55) Lindley, S. A.; Cooper, J. K.; Rojas-Andrade, M. D.; Fung, V.; Leahy, C. J.; Chen, S.; Zhang, J. Z. Highly Tunable Hollow Gold Nanospheres: Gaining Size Control and Uniform Galvanic Exchange of Sacrificial Cobalt Boride Scaffolds. *ACS Applied Materials and Interfaces* **2018**, *10* (15), 12992-13001.

(56) Douglas, S. M.; Bachelet, I.; Church, G. M. A logic-gated nanorobot for targeted transport of molecular payloads. *Science* **2012**, *335* (6070), 831-834.

(57) Yang, J.; Palla, M.; Bosco, F. G.; Rindzevicius, T.; Alstrøm, T. S.; Schmidt, M. S.; Boisen, A.; Ju, J.; Lin, Q. Surface-enhanced Raman spectroscopy based quantitative bioassay on aptamer-functionalized nanopillars using large-area Raman mapping. *ACS Nano* **2013**, *7* (6), 5350-5359.

(58) Pang, S.; Labuza, T. P.; He, L. L. Development of a single aptamer-based surface enhanced Raman scattering method for rapid detection of multiple pesticides. *Analyst* **2014**, *139* (8), 1895-1901.

(59) Auyeung, E.; MacFarlane, R. J.; Choi, C. H. J.; Cutler, J. I.; Mirkin, C. A. Transitioning DNA-engineered nanoparticle superlattices from solution to the solid state. *Advanced Materials* **2012**, *24* (38), 5181-5186.

(60) Liu, X.; Zhang, F.; Jing, X.; Pan, M.; Liu, P.; Li, W.; Zhu, B.; Li, J.; Chen, H. Complex silica composite nanomaterials templated with DNA origami. **2018**.

(61) Kim, N. H.; Hwang, W.; Baek, K.; Rohman, M. R.; Kim, J.; Kim, H. W.; Mun, J.; Lee, S. Y.; Yun, G.; Murray, J.; et al. Smart SERS Hot Spots: Single Molecules Can Be Positioned in a Plasmonic Nanojunction Using Host–Guest

Chemistry. *Journal of the American Chemical Society* **2018**, *140* (13), 4705-4711.

Chapter 3: Cage-Constrained Inter-Particle Hybridization

3.1 Introduction

The specific A to T and G to C base-parings make DNA a mighty and versatile tool for programable self-assembly.[1] As early as 1996, Alivisatos et al.[2] and Mirkin et al.[3] independently used base pairing interactions between DNA to assemble nanoparticles into clusters. The large nanoparticles often possess more tantalizing plasmonic effects their smaller counterparts don't have,[4] such as strong LSPR (localized surface plasmon resonance) and retardation effects.[5] Therefore, a critical challenge in DNA-directed self-assembly is to form discrete plasmonic molecules containing large nanoparticles. As described in Chapter 2, two DNA-directed nanoparticle self-assembly strategies are widely used in literature: (1) Direct linkage (2) Binding to DNA origami surface. After two complementary DNA ligands were added to two types of nanoparticles, the ligands in the nanoparticle mixture could hybridize to form direct linkage. However, due to the flexible single duplexes that link the nanoparticles, the bond angle and gap size of these assemblies often display large variability. Moreover, the direct linkage strategy requires nanoparticles decorated with a defined number of DNA ligands, which is not feasible for large nanoparticles >20 nm (Fig.3.1a).[6-7] In contrast, larger nanoparticles can be more readily coated with a dense layer of DNA ligands (Fig.3.1b),[8] the complementary strands displayed on DNA origami surface could bind nanoparticles via hybridization.

In Chapter 2, to form plasmonic molecules with well-defined valences, bond angles and gap sizes, we introduced a new nanoparticle assembly strategy termed docking to DNA origami cage (D-DOC), which uses multiple spatially separated capture strands to bind constituent nanoparticles and at the same time utilizes shape complementarity and physical contacts between ligand shells to further confined these nanoparticles. While our strategies produced 30 nm-10 nm-30nm linear trimers with well-defined gap sizes, the assembled trimer consisting of two terminal 50 nm fAuNPs suffered from large distortions. The strong van der Waals attractions between 50 nm fAuNPs caused strong cage deformations, which created misalignments of bound nanoparticles due to diminished nanoparticle-to-template interactions and ligand-to-ligand contacts. Our distorted 50 nm-10 nm-50 nm trimers also suggested even with the implementation of a rigid DNA origami cage, a few capture strands couldn't resist van der Waals attractions between large fAuNPs.

To address this problem, we proposed a new approach (Fig.3.2a), cage-constrained inter-particle hybridization (CCIPH). Instead of using outside capture strands to bind the terminal nanoparticles as in D-DOC, CCIPH relies on the openings of the DNA origami cage that encapsulates a central particle to control where the ligands on the terminal particles can hybridize with the

ligands on the central particles. We hypothesize that CCIPH could effectively resist van der Waals attractions between 50 nm fAuNPs to produce well-defined bond angle:[9] the merging of two ligand shells via inter-particle hybridization in combination with shape complementarity between the cage openings and the terminal practices may significantly improve the rigidity of the resulting 50 nm IPTs (inter-particle trimers). Moreover, DNA duplex has a more well-defined length and could reduce variations in gap size.[10] Our CCIPH is a hybrid of the main strategies for DNA directed self-assembly of nanoparticles, direct linkage and DNA origami templated assembly. It allows the interactions between nanoparticles as well as those between nanoparticles and the DNA template to work synergistically to define the 3D spatial arrangements of the constituent nanoparticles. Therefore, it represents a conceptual breakthrough that can aid the synthesis of complex 3D plasmonic molecules with precise geometrical arrangements.
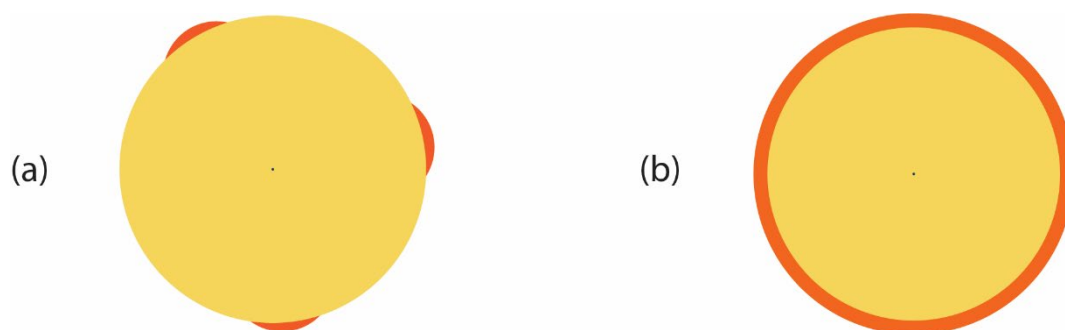
Figure 3.1. Schematic of gold nanoparticle surface functionalization. (a) Adding a defined number of DNA ligands at defined positions. (b) Coat the whole surface by DNA ligands.Yellow circles are nanoparticles. Red protrusions: spatial-defined DNA ligands on nanoparticle surface, red circumference: DNA ligands covering the whole surface.
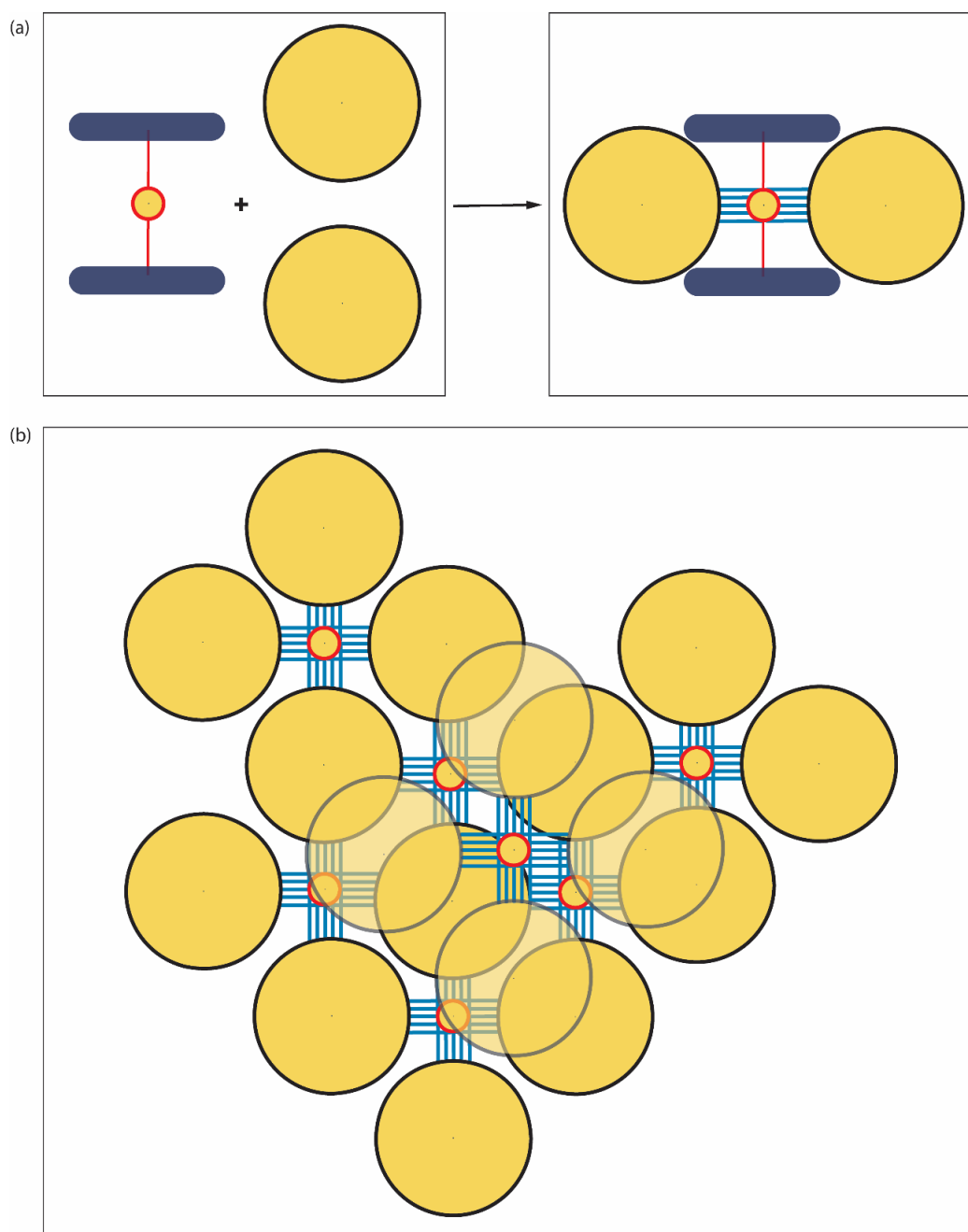
Figure 3.2. Schematic of inter-particle hybridizations. (a) Cage-constrained (b) Unconstrained. Blue rectangle with rounded corner: DNA origami cage. Red line: Inside capture strands. Yellow spheres: Gold nanoparticles. Black circumference: DNA ligands covered the whole surfaces of large gold nanoparticles. Red circumference: Complementary ligands covered the whole surfaces of small gold nanoparticles. Blue lines: DNA duplexes formed by inter-particle hybridization.

3.2   Materials and Method

Materials are included in section 3.2.1. Thiolated DNA functionalization of gold nanoparticles are included in section 3.2.2, and the design and folding DNA origami cage are in section 3.2.3 together with the general trimer assembly protocol. Assembled 50 nm IPTs are separated from unreacted nanoparticles by gel electrophoresis (section 3.2.4). To perform structural characterizations, trimers are examined SEM (section 3.2.5). Furthermore, FDTD simulations are performed and included in section 3.2.6.

3.2.1 Materials

M13mp18 ssDNA (scaffold) was purchased from New England Biolabs (NEB), resuspended in ultrapure water, and used without further purification. All staple strands were purchased from Integrated DNA Technologies (IDT), diluted with 1× Tris-EDTA (TE) buffer without further purification. Regular 3' thiol-modified DNAs were purchased from IDT (Fig.1.8), resuspended in ultrapure water without further purification. DNA loading dye was purchased from Fischer Scientific. SYBR green (I) DNA stain was purchased from ThermoFisher. agarose, TE and Tris-Borate-EDTA(TBE), and EDTA (Ethylenediaminetetraacetic acid) buffers, Tris, sodium dodecyl sulfate (SDS), sodium chloride (NaCl), magnesium chloride ($MgCl_2$), tri(carboxyethyl) phosphine hydrochloride (TCEP) were purchased from MilliporeSigma, USA. Colloidal solutions of unconjugated (bare) 10 nm and 50 nm AuNPs were purchased from Ted Pella. All DNA sequences are summarized in Table A.1-A.4 (Appendix).

3.2.2 Functionalization of Gold Nanoparticles

The protective disulfide bond of thiolated DNAs was cleaved to form monothiol using TCEP (stock concentration of 100 mM) at room temperature (RT) in water, and the molar ratio of thiolated DNA to TCEP was 1:1000. The reduced thiolated DNAs were purified using Amicon ultra centrifugal filters (MilliporeSigma) with a molecular weight cut-off (MWCO) value of 3k Da twice to remove the small molecules. The purified mono-thiolated DNAs were added to bare AuNP with a DNA to AuNP molar ratio of 660:1 for 10 nm AuNPs in ultra-pure water containing 0.1% (w/v) SDS, then incubated with gentle shaking on a vortex mixer overnight at room temperature (RT). To functionalize 50 nm AuNP,[11] there are two other requirements: (1) the total volume for each batch needs to be 0.2 mL or less (2) the final DNA concentration needs to be > 3.0 μM. After overnight incubation, a slow salt-

aging method was used to promote the attachment of thiolated DNA to AuNP surfaces.[12] A concentrated NaCl stock solution (5 M) was added to AuNP and thiolated DNA mixture to increase the [NaCl] by 0.050 M. The mixture was then backfilled with N_2, sonicated for 5 seconds, and incubated at least 1 hour with gentle shaking at RT. Such salt-additions were repeated until reaching a final NaCl concentration of 0.30 M for 10 nm AuNP, 0.50 M for 50 nm AuNP then the mixture was left on RT to incubate overnight with gentle shaking. The 10 nm fAuNPs were washed with ultra-pure water in 100k Da Amicon filters eight times to remove excess thiolated DNAs. The 50 nm fAuNPs were purified by centrifugation at 14,000×g for 3 minutes in a 2 mL Eppendorf Microcentrifuge tube three times. After each centrifugation, the supernatant was removed and then resuspended in ultra-pure water. Purified fAuNPs were backfilled with N_2 and stored in a refrigerator at 4 °C before use. The concentrations of fAuNPs were determined from the optical absorbances at 520 nm (10 nm AuNP) and 530 nm (50 nm AuNP) assuming no change in molar extinction coefficients after DNA functionalization. All fAuNPs were stable in the trimer assembly buffer (TAB) containing 1.0 mM EDTA, 5.0 mM Tris, 12.0 mM $MgCl_2$ and 0.30 M NaCl at RT or subject to prolonged thermal annealing, which is ideal for the directed assembly by DNA origami.

3.2.3 Design of 3D DNA Origami Cage and Syntheses

Our 3D origami cage with a cuboid cavity (20 nm × 20 nm × 17 nm), a modification of Yan's nanocage, was designed with honeycomb lattice using caDNAno (http://cadnano.com/).[13] The software generated 192 staple strand sequences that are complementary to that of single-stranded M13mp18 scaffold DNA. The cage has 124 DNA helices and an overall dimension of 47 nm × 40 nm × 17 nm (Fig.2.6-7) estimated by using 0.34 nm per base pair and 2 nm DNA helix height.[10] To avoid blunt-end stacking, [13] either two bases are left unpaired or two extra thymines (T) are added at the ends of each helix.

To bind the small nanoparticle in the cavity, and four inside capture strands all have 5' end extensions and protrude from the centers of helices # 31,41,96,73 respectively (Fig.2.7c). Outside strands are removed from cage design.

The molar ratio of the scaffold to capture strands was 1:1, while 10× other staples with respect to scaffold were used. The mixture of the scaffold (10 nM) and staples was placed in a folding buffer (1 mM EDTA, 5 mM Tris, 12 mM $MgCl_2$) and slowly cooled from 90 °C to 25 °C over 2 days in a thermal cycler. The cooling rate at effective folding temperatures 60 °C to 40 °C was reduced

to 0.2 ℃/hr. The concentration of unpurified origami was estimated by assuming a 100% folding yield.

The unpurified origami cage was mixed with purified 2× 10 nm fAuNP in TAB with 0.05% SDS, backfilled with N_2. The mixture was first slowly heated from 20 ℃ to 42 ℃ and then thermal annealed from 42 ℃ to 20 ℃ over 34 hours in total to encapsulate 10 nm fAuNP in the origami cage cavity. The cage-encapsulated 10 nm fAuNPs were purified by gel filtration and then mixed purified 50 nm fAuNPs in TAB with 0.05% SDS, backfilled with N_2, and incubated at RT in the dark for ~4 hours to form the target 50 nm IPT, the synthesized 50 nm IPTs were stored at 4 ℃ prior to purification.

3.2.4 Purification of 50 nm IPT

After incubation at RT, the mixture of cage-encapsulated 10 nm fAuNPs and 50 nm fAuNP was loaded with the help of a DNA loading dye in an agarose double gel layer system (running buffer: 0.5× TBE) at constant 65 V for 1 hour over ice. [14] The bottom gel layer was a 4% agarose gel to prevent leakage of the sample in the top layer, and a 0.8% or 1% top layer was poured directly on the bottom layer. After band separation appeared, the unwanted band was cut out, and a small pocket in front of the band of interest was dug through the top layer and filled with TAB. Then, the band of interest was electroeluted to the pocket and collected by micropipette. If needed, the purified 50 nm IPT could be concentrated by centrifugation (14,000×g, 5 minutes) in a 2 mL microcentrifuge tube (Eppendorf).

3.2.5 SEM Characterizations

3.0 µL of purified 50 nm IPT was deposited onto Ar plasma treated silicon wafers for ~2 minutes then washed with 20.0 µL water and dried in a vacuum chamber for 24 hours before SEM (Scanning Electron Microscopy) characterization. The sample was imaged by Zeiss Gemini 500 FEG-SEM system with EHT 5.0 kV to 10.0 kV. The statistical analysis of gap sizes and bond angles were conducted using AutoCAD 2019 (Fig. 2.10).

3.2.6 FDTD Simulations
3.3 Results and Discussion

The section will be divided into six subsections. Prior to 50 nm IPT synthesis, section 3.3.1 will first present the results of unconstrained inter-particle hybridization (Fig.3.2b) as a control experiment. The most critical and unique

step in 50 nm IPT synthesis is the inter-particle hybridization between 50 nm fAuNPs and the cage-encapsulated 10 nm fAuNP. Therefore, section 3.3.2 will include the detailed investigations of the cage-constrained interparticle hybridization step using color comparisons, agarose gel electrophoresis and SEM. Detailed structural determinations of 50 nm IPT will be presented in section 3.3.3 using SEM together with statistical analyses to assess the effectiveness of our CCIPH approach on aligning the centers of all nanoparticle constituents of 50 nm IPT. FDTD simulations of 50 nm IPTs will be included in section 3.3.4 to show the possible plasmonic effects and potential applications of 50 nm IPT.

3.3.1 Unconstrained Inter-Particle Hybridizations

Inter-particle hybridization is the driving force of 50 nm IPT synthesis.[16-18] Hence, we first performed a control experiment by mixing 10 nm fAuNP and 50 nm fAuNP with complementary DNA ligands in TAB. In less than 10 seconds, the mixture became blue (Fig.3.3a), an indicator of large aggregates. We then examined the mixture using gel electrophoresis (Fig.3.3b). The gel result showed the blue mixture were stuck in the loading well, confirming the formation of large aggregates. It is noted the aggregates are thermodynamic product and cannot be reversed by thermal agitations. As a result, inter-particle hybridization is a double-edged sword. For one thing, it quickly formed irreversible aggregates indicated the facile hybridization and strong binding between fAuNPs. For another, it formed the random large aggregates leaving practical applications to chance. To leverage the benefits of IPT while minimizing the drawbacks, we used our cage to constrain the inter-particle hybridizations to synthesize discrete 50 nm IPTs.
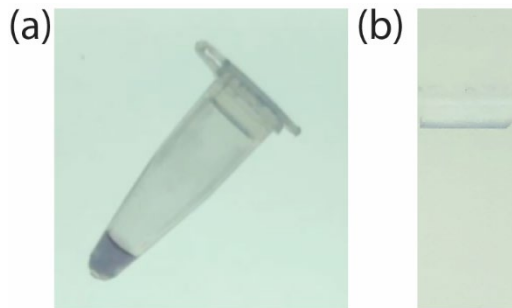

Figure 3.3. Unconstrained DNA hybridization as a control experiment.(a). Picture of mixing 10 nm fAuNP and 50 nm fAuNP having complementary ligands in TAB. (b) Agarose gel result of the purple mixture in (a).

3.3.2 Synthesis of 50 nm IPT

The 50 nm IPT synthesis consists of three steps: folding cage, encapsulation of the 10 nm fAuNP, and inter-particle hybridization between the cage-encapsulated 10 nm fAuNP and 50 nm fAuNPs having complementary ligands. The first two steps were the same as in our model trimer synthesis, and the only minor adjustments concerned the purification of the cage-encapsulated 10 nm fAuNPs. We first performed the inter-particle hybridizations using the unpurified and purified cage-encapsulated 10 nm fAuNPs respectively. Within a few minutes, the mixtures of 2× 50 nm fAuNPs and the unpurified cage-encapsulated 10 nm fAuNPs in TAB turned purple, while the mixture of purified cage-encapsulated 10 nm fAuNPs and 50 nm fAuNPs stayed pink for hours in TAB (Fig.3.4a). We then ran gel electrophoresis to characterize the two mixtures (Fig.3.4a). The purple mixture had severe smear in gel, an indicator of smaller aggregates formed by unconstrained interparticle hybridization between non-encapsulated 10 nm fAuNPs and 50 nm fAuNPs, while the mixture using purified encapsulated product showed two bands: fast-moving unreacted 50 nm fAuNP band and the 50 nm IPT band moving at a slower pace, which indicated that our cage effectively constrained the inter-particle hybridizations to form discrete structures.

A potential concern is that the finite yield of the purification of the cage-encapsulated 10 nm fAuNPs reduces the overall yield.[19] Therefore, we explored an alternative approach that may allow us to skip the purification step. To minimize the concentration of unbound 10 nm fAuNPs, we investigated the possibility of using purified cage for the encapsulation step and varied the stoichiometric ratio between 10 nm fAuNP to the purified cage. By reducing the stoichiometric ratio from 1:1 to 0.25:1, the unbound nanoparticle band was invisible in gel at the cost of extremely faint band of the cage-encapsulated 10 nm fAuNPs. However, severe smear still appeared in the gel, making 50 nm IPT purification infeasible (Fig.3.4b). The result suggests there were still a non-negligible fraction of the 10 nm fAuNPs that remain unbound even when 10 nm fAuNPs were the limiting reagent in the encapsulation step. We hypothesized the unbound 10 nm fAuNPs were caused by (1) a small fraction of cages that had no or fewer than nominal capture strands (2) some DNA ligands were removed from 10 nm fAuNP surface and hybridized with inside capture strands. A further reduction in stoichiometric ratio might reduce unbound 10 nm fAuNP at a cost of lowering of the already minimal overall yield. Therefore, we chose to first encapsulate 10 nm fAuNPs inside unpurified cages and then purify the cage-encapsulated 10 nm fAuNPs. We found that this purification step must be performed with gel filtration. None of the other methods we explored could effectively remove unbound 10

nm fAuNPs without incurring heavy contamination. However, the gel filtration had a low purification yield, and the concentration of purified encapsulated product could not be determined accurately because DNA ligands and DNA origami cage both absorbed at 260 nm and the 10 nm fAuNP concentration was too low to be detected by UV-Vis. All the uncertainties in purifications resulted in large batch to batch variations in interparticle hybridization rate. To improve interparticle hybridization rate, we attempted a latch and merge method (Fig.3.5a) in which the 50 nm fAuNP was first bound by outside capture strands at the cage openings, and then the ligands of the neighboring particles would undergo cage-constrained inter-particle hybridization. Our preliminary data showed it was feasible to back-insert outside capture strands into the folded cage (Fig.3.5b). However, this latch and merge method requires deliberate sequence design. If the outside capture strands are fully complementary to the ligands of 50 nm fAuNP, the bound 10 nm fAuNP in the cavity could be displaced by outside capture strands, or the outside and inside capture strands could hybridize reducing the encapsulation rate if outside capture strands are included in cage folding. Systematic investigations on synthesis optimizations will be needed to improve the overall yield of 50 nm IPT.

The overall yield (~5%), however, was enough for structural analyses owing to the sensitivity of electron microscopy. It is noted sometimes multiple slower-moving bands could be seen in gel even when the purified cage-encapsulated 10 nm fAuNPs were used (Fig.3.6). The gel bands of interests were purified and visualized by SEM.
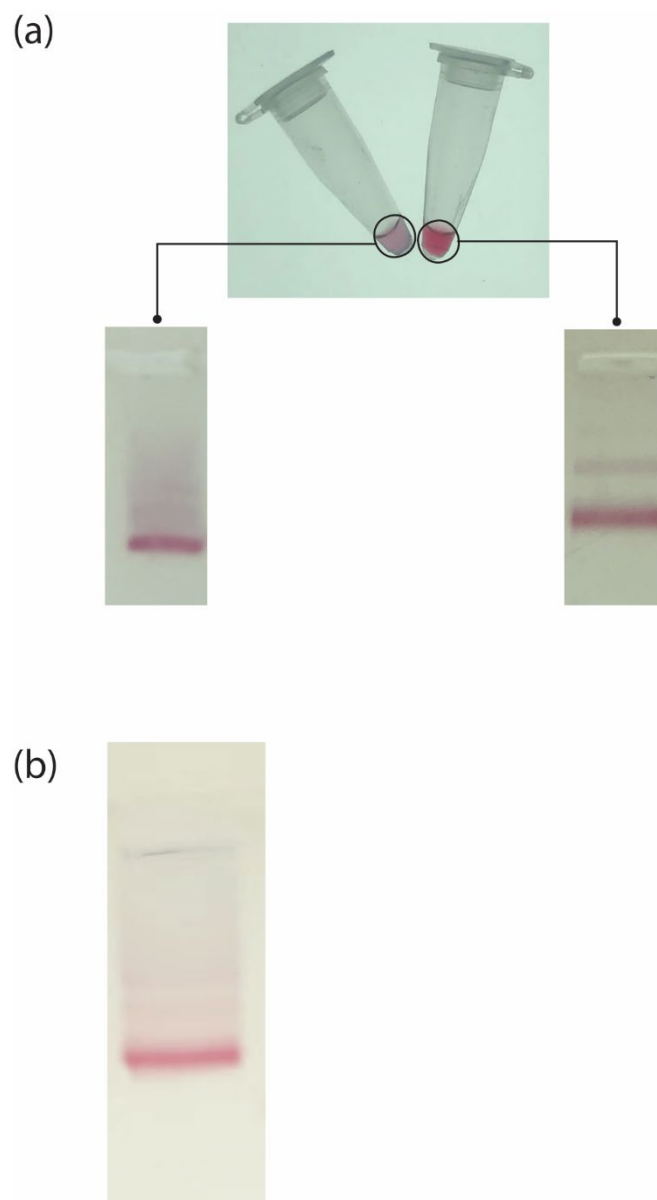
Figure 3.4. Agarose gel results of 50 nm IPT. (a) Left: Synthesis using unpurified encapsulated product (2×10 nm fAuNP); Right: Synthesis using purified encapsulated product. (2×10 nm fAuNP used). (b) 50 nm IPT Synthesis using unpurified encapsulation product (0.25× 10 nm fAuNP used).
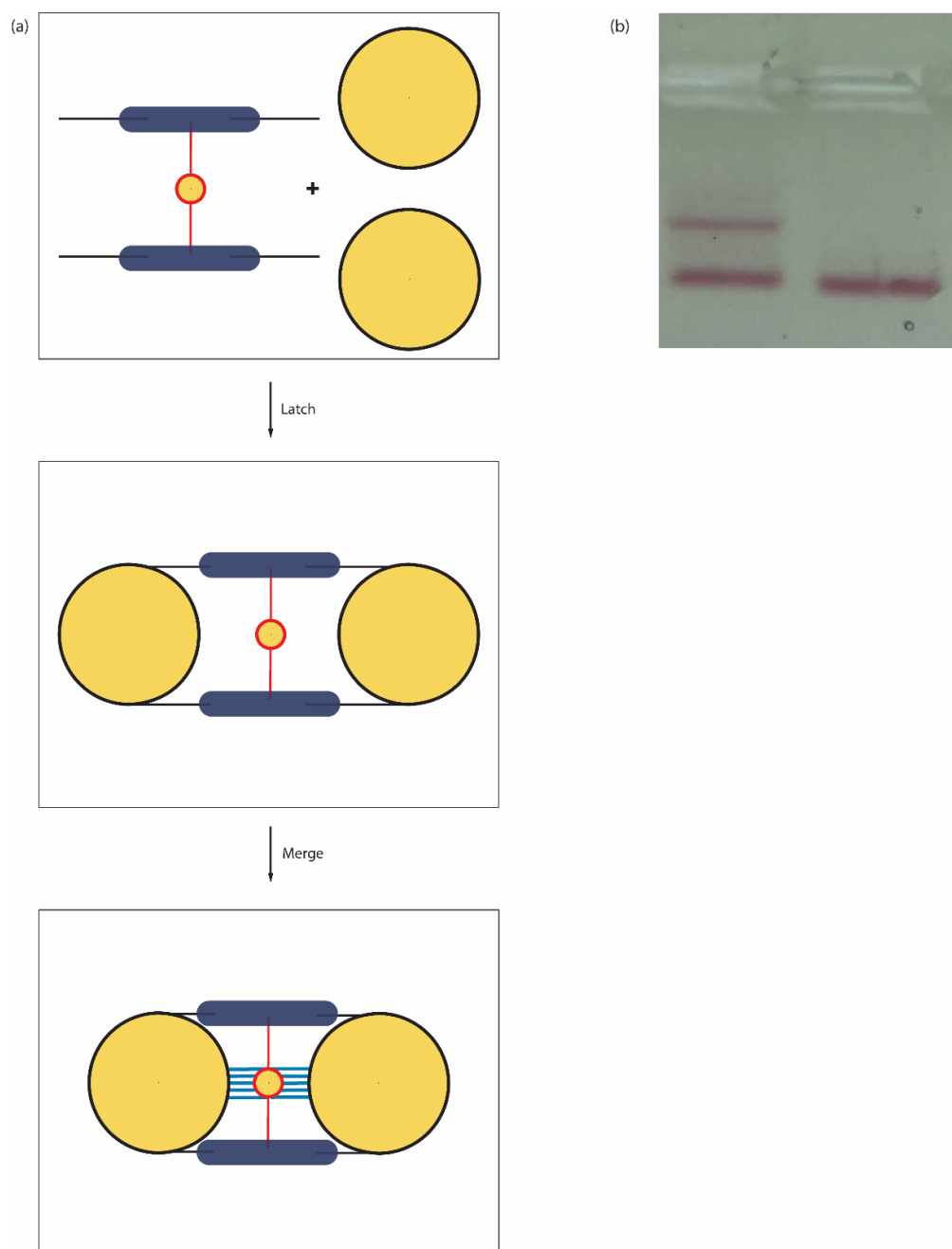
Figure 3.5. Latch and merge method. (a) Schematic. Blue rectangle with rounded corner: DNA origami cage. Red line: inside capture strands. Black line: outside capture strands. Yellow sphere: gold nanoparticles. Red circumference: Complementary ligands covered the whole nanoparticle surfaces of small gold nanoparticle. Blue lines: DNA duplexes formed by unconstrained inter-particle hybridization. (b) Agarose gel results of 30 nm fAuNP mixed with cage without outside capture strands (Right). Folded cage with back-inserted outside capture strands and 30 nm fAuNP that has complementary ligands (Left).
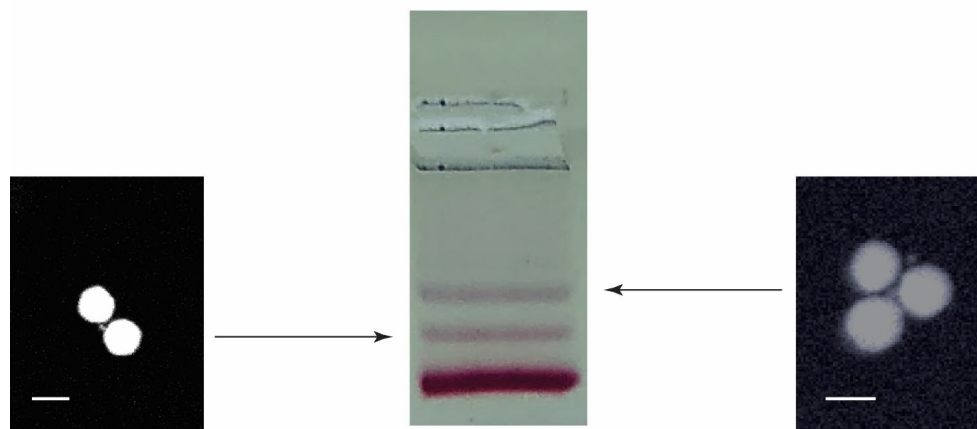
Figure 3.6. Characterizations of agarose gel showing two slow-moving bands. Back-scattering detector used. Scale bar: 50 nm. The thick pink band at bottom is unbound 50 nm fAuNPs.

3.3.3 SEM Analyses of 50 nm IPT

We first investigated samples having two slow-moving bands in gel. A representative micrograph of each band was included in Fig.3.6. Interestingly, the slowest-moving band on top was small aggregate, while the other slow-moving band corresponded to 50 nm IPTs. The formation of small aggregates might be due to a trace amount of unbound 10 nm fAuNP or a damaged cage overexposing the encapsulated 10 nm fAuNP to the 50 nm fAuNP. We then examined the samples with only one slow-moving band in gel, which rendered mainly 50 nm IPTs. The representative SEM micrographs of 50 nm IPTs are in Fig.3.7 and bending angle distribution were in Fig.3.5c. The summary of bending angels of the trimers (50 nm IPT, 30 nm-10 nm-30 nm and 50 nm-10 nm-50 nm trimers) are listed in Table 3.1. Of the three trimers, our model 30 nm-10 nm-30 nm trimer had the smallest bending angle (θ <10°), while the 50 nm-10 nm-50 nm trimer was very distorted (θ >60°), our 50 nm IPT (θ <17°) was only slightly more bent than our linear model trimer, but >3 times less bent than its 50 nm-10 nm-50 nm counterpart. The large differences in bending angle indicated (1) our cage could confine 30 nm fAuNP by utilizing two outside capture strands and other synergistic interactions; (2) two outside capture strands could only bind the 50 nm fAuNP to the cage opening, but the resulting trimers were badly distorted (θ >60°) even with other interactions that favor the linear configurations (3) CCIPH could effectively resist the van der Waals attractions between 50 nm fAuNP producing an average 16.7° bending angle (supplementary angle of bond angle). It should be noted that the

true bending angles, θ_{3D}, may differ from the 2D projected bending angle (θ, defined in the inset of Fig.3.8a) measured in SEM micrographs. Numerical simulations based on equation (1) defined in Chapter 2 where φ is the angle between plane of nanoparticles and plane of the solid support

$$\sin \frac{(180° - \theta)}{2} = \cos \varphi \sin \frac{(180° - \theta_{3D})}{2} \qquad (1)$$

reproduced the experimentally observed θ distribution by assuming random φ and two populations of θ_{3D}, one centered at 18° and the other at 32° (Fig.3.8b). Although most 50 nm IPTs had relatively small bending angles, there were still a small fraction had $\theta > 35°$. It remains unclear whether drying effects or the profound van der Waals attractions distorted 50 nm IPT monomers. To obtain accurate bending angles and minimal loss of structural information, cryo-EM tomography will be needed to reconstruct the structures in 3D without the potential distortion caused by drying.

We hypothesized that cage-constrained inter-particle hybridizations formed multiple DNA duplexes in between fAuNPs, and the nominal length of each 16bp-duplex was ~5.44 nm (0.34 nm/bp in solution) comparable to our measured ~ 3.46 ± 1.77 nm gap size (more size measurements in Table A.7), and this small discrepancy could be due to drying effects and limited resolution of SEM (~10 nm). We then performed correlation analyses to investigate how bending angle and sizes of fAuNPs affects the interparticle gap. The spearman's correlation coefficients (ρ) are 0.0164, 0.308, 0.251, 0.00347 for Fig.3.9(a)-(d), respectively.[20]The small absolute ρ values here suggested gap size was either weakly correlated ($0.2 < |\rho| < 0.3$) or uncorrelated ($0.01 < |\rho| < 0.2$) to the bending angle and fAuNP sizes. It is not feasible to accurately measure gap size using SEM due to limited resolution (~1nm at best) and the required drying process. However, cryo-EM, highest resolution of ~0.6 nm, is a perfect tool for accurate size measurements, tracing the origins for small aggregates, and possible visualizations of DNA duplexes between fAuNPs. Lastly, we performed FDTD simulations to investigate the potential plasmonic properties of our 50 nm IPT.

Trimers	Bending Angles
30 nm -10 nm -30 nm	9.7° ± 6.9
50 nm -10 nm -50 nm	60.7° ± 20.0
50 nm IPT	16.3° ± 9.4

Table 3.1. Average bending angles of three trimers.
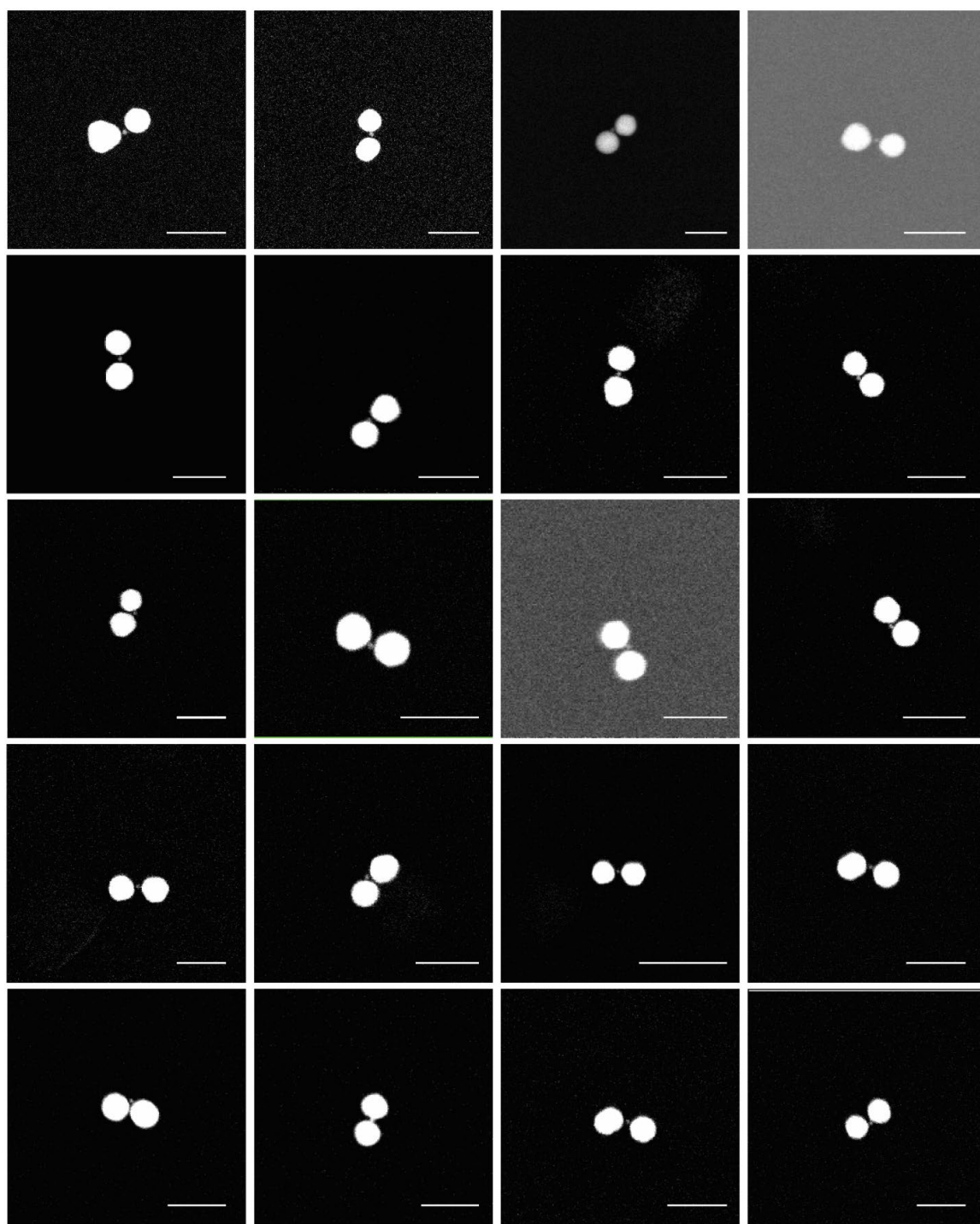
Figure 3.7. SEM images of 50 nm IPTs. Back-scattering detector was used. Scale bar: 100 nm.
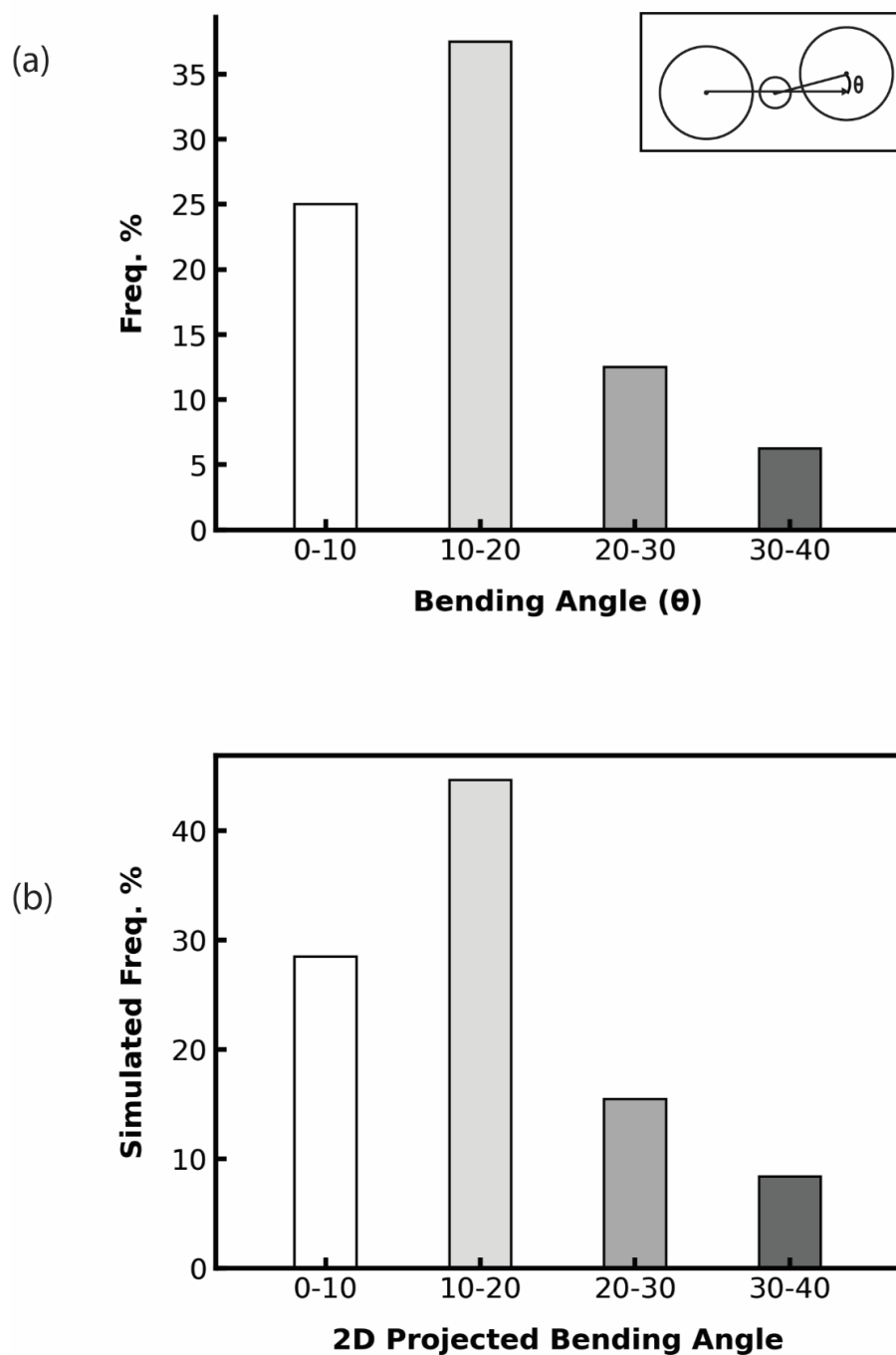
Figure 3.8. Bending angle analyses of 50 nm IPT. (a) Bending angle distribution histogram. Inset: schematic of the bending angle θ. (b) Simulated histogram of 2D projected bending angle of 50 nm IPT. with 3D bending angles that have two populations with normal distribution: 18.0°±0.9 and 32°±0.9 could reproduce the histogram in (a).
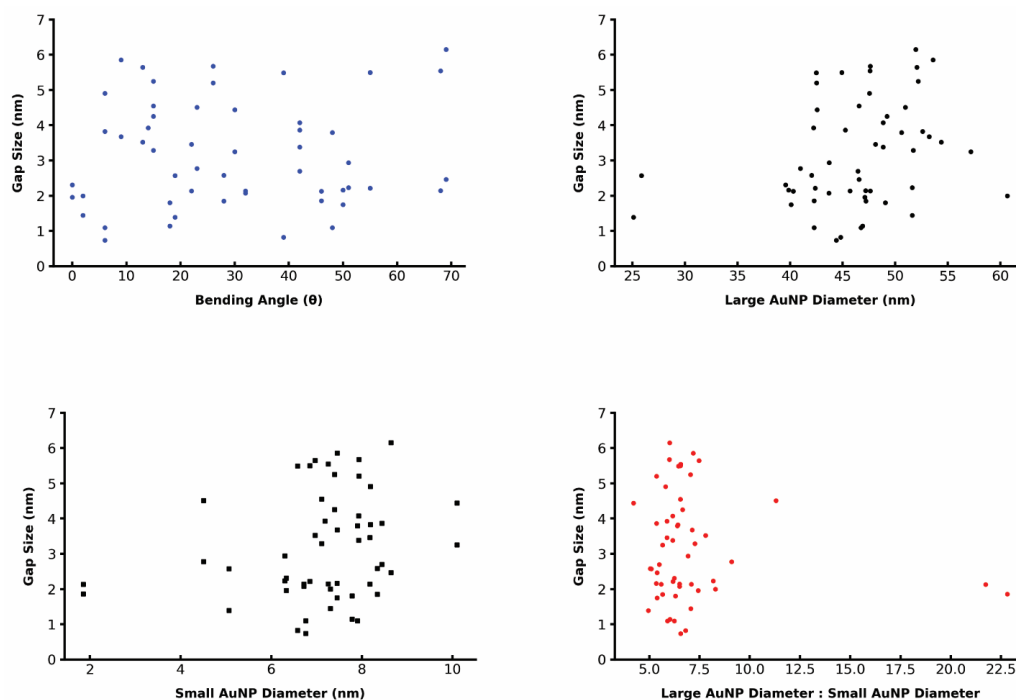
Figure 3.9. Correlation analyses of 50 nm IPT gap sizes. (a) Gap size versus bending angle. (b) Gap size versus large AuNP diameter. (c) Gap size versus small AuNP diameter. (c) Gap size versus the ratio between large AuNP diameter and small AuNP diameter. All raw data were collected from trimer SEM images.

3.3.4 FDTD Simulations of 50 nm IPT

The simulated absorption spectra of 50 nm IPT are in Fig. 3.10a. When light propagates along the transverse axis, the plasmonic coupling in 30 nm-10 nm -30 nm trimers was minimal (Fig.2.23) and its peak overlapped with the single 30 nm AuNP. However, the simulated transverse absorption spectrum (λ_{max}=546 nm) of 50 nm IPT showed 10 nm redshift from individual 50 nm fAuNP (Fig.3.10a-b) inferring plasmonic assemblies of large AuNPs have effective plasmon(ic) coupling even at non-optimal excitation angle. Larger AuNPs are known to have multipolar modes that may interact with the LSPR modes of the 10 nm AuNPs. These coupled modes can be excited even when light is not polarized along the long axis of the trimer. Interestingly, 50 nm IPT showed two large peaks (λ_{max}=571 nm, 633 nm) and a shoulder peak (λ_{max}=677 nm) when light propagates along the longitudinal axis. The larger redshifts implied stronger plasmonic coupling between particles, and the extra shoulder peak might be ascribed to phase retardation effects that only exist in larger

nanoparticles.[5] We also conducted electric field simulation using FDTD (Fig. 3.10c-d) and calculated EF. As in the model 30 nm-10 nm-30 nm trimer, the EF of 50 nm IPT is dependent on the excitation wavelength (Fig.3.10d). It is surprising to note that 50 nm IPT showed a lower maximum EF than the model 30 nm-10 nm-30 nm trimer. However, at the excitation wavelength of 633 nm, a conventional laser wavelength, 50 nm IPT showed an average of nearly 10^{10} EF, and if realized experimentally, would enable single molecule detection for not only Raman dyes but also molecules with relatively small Raman cross-sections such as alkynes.[21] SERS measurement prefers longer laser wavelength to reduce the interferences of fluorescence background, and unlike 30 nm-10 nm-30 nm trimers only showing high EF at low excitation wavelength, 50 nm IPT showed nearly 10^6 simulated EF when excitation wavelength is 700 nm. Taken together, FDTD simulations suggest that our 50 nm IPT has significant potential as a SERS substrate for ultrasensitive detection of biomarkers and a model plasmonic molecule to investigate fundamental plasmonic theories.
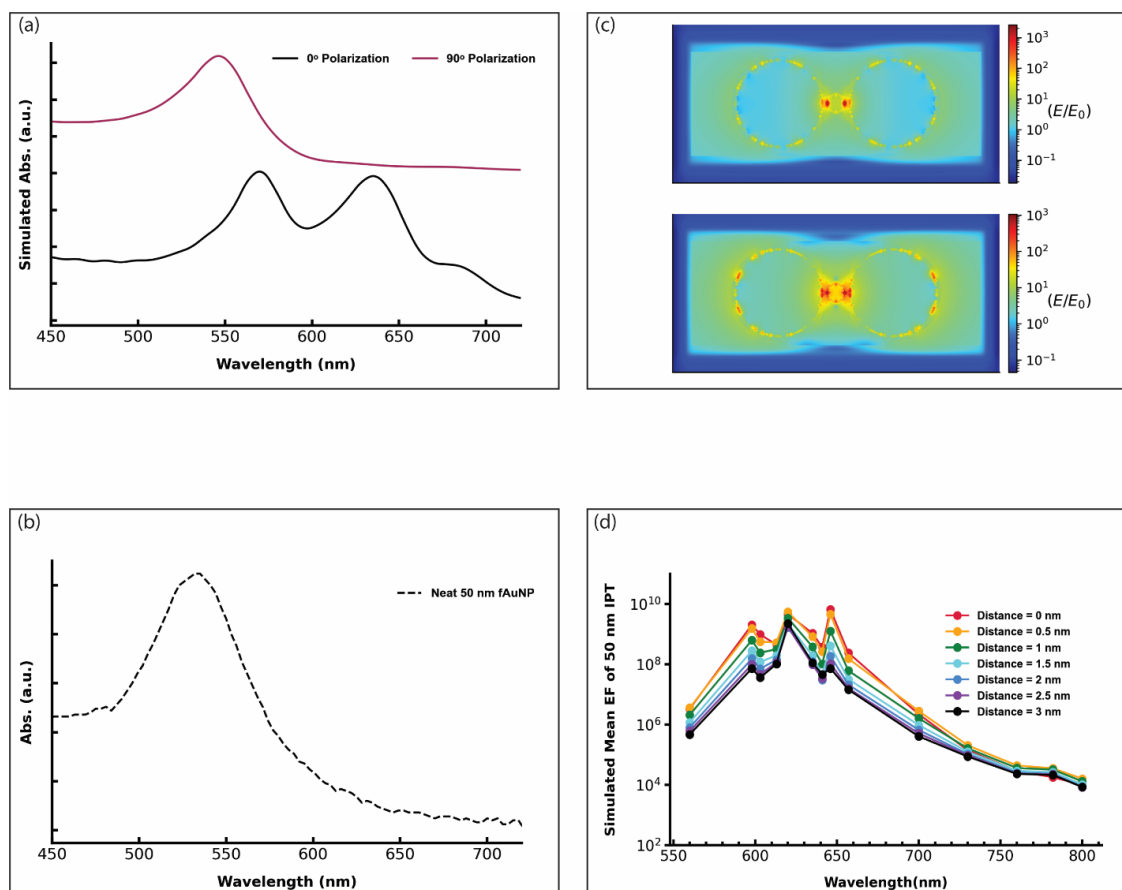
Figure 3.10. FDTD simulation data of 50 nm IPT. (a) Simulated absorption spectra. (b) Experimental absorption spectrum of neat 50 nm fAuNP. (c) Simulated mean wavelength-dependent EF of 50 nm IPT (3 nm gap, $\theta=0°$), distance: the distance from the central nanoparticle surface. (d) Simulated electric field of 50 nm IPT (3 nm gap, $\theta=0°$) using $\lambda_{ex}=$ 646 nm (top), 633 nm (bottom), longitudinal excitations.

3.4 Conclusion and Future Directions

In summary, we demonstrate that our new strategy to use DNA origami cage to direct hybridization between ligands on nanoparticles can precisely control bond angles and gap sizes of 50 nm-10 nm-50 nm linear trimers. The small bending angles observed despite the strong van der Waals attractions between 50 nm fAuNPs may be a consequence of the rigidity afforded by multiple DNA duplexes linking the fAuNPs as well as support provided by the DNA origami cage. Although CCIPH is still in its infancy, we anticipate it has the potential to be extended to make more complex plasmonic molecules containing large nanoparticles of varying shapes. In contrast to their smaller counterparts,

larger plasmonic molecules are predicted to have interesting plasmonic properties including strong EF at longer wavelength, multipolar plasmonic modes, just to name a few. Our ongoing research is to optimize purification and inter-particle hybridization steps in 50 nm IPT synthesis, and our latch and merge method showed some promising preliminary results (Fig.3.5d). Future cryo-EM/tomography experiments will reveal the accurate cage structures, bond angles, gap sizes and even the duplex densities between nanoparticles.[22] We anticipated with the aid of cryo-EM, proper experimental and cage design optimizations could increase the overall yield of 50 nm IPT and enable quantitative plasmonic characterizations. Ultimately, our new strategy, which is a hybrid of two current main strategies for DNA-directed self-assembly of nanoparticles: direct linkage and DNA origami templated assembly, may serve as a new paradigm in the synthesis of plasmonic molecules by enabling the formation of complex plasmonic molecules with precisely tailored geometries.

Reference

(1) Seeman, N. C. *Structural DNA Nanotechnology*; Cambridge University Press, 2015.

(2) Alivisatos, A.; Johnsson, K.; Peng, X.; Wilson, T.; Loweth, C.; Bruchez, M.; Schultz, P. Organization of 'nanocrystal molecules' using DNA. *Nature* **1996**, *382* (6592), 609-611.

(3) Mirkin, C. A.; Letsinger, R. L.; Mucic, R. C.; Storhoff, J. J. A DNA-based method for rationally assembling nanoparticles into macroscopic materials. *Nature* **1996**, *382* (6592), 607-609.

(4) Maier, S.; Brongersma, M.; Kik, P.; Meltzer, S.; Requicha, A.; Atwater, H. Plasmonics - A route to nanoscale optical devices. *Advanced Materials* **2001**, *13* (19), 1501-1505.

(5) Fitzgerald, J. M.; Giannini, V. Battling Retardation and Nonlocality: The Hunt for the Ultimate Plasmonic Cascade Nanolens. *ACS Photonics* **2018**, *5* (6), 2459-2467.

(6) Yao, G.; Pei, H.; Li, J.; Zhao, Y.; Zhu, D.; Zhang, Y.; Lin, Y.; Huang, Q.; Fan, C. Clicking DNA to gold nanoparticles: poly-adenine-mediated formation of monovalent DNA-gold nanoparticle conjugates with nearly quantitative yield. *NPG Asia Materials* **2015**, *7* (1), e159-e159.

(7) Lermusiaux, L.; Funston, A. M. Plasmonic isomers via DNA-based self-assembly of gold nanoparticles. *Nanoscale* **2018**, *10* (41), 19557-19567.

(8) Hurst, S.; Lytton-Jean, A.; Mirkin, C. Maximizing DNA loading on a range of gold nanoparticle sizes. *Analytical Chemistry* **2006**, *78* (24), 8313-8318.

(9) Barrow, S. J.; Funston, A. M.; Wei, X.; Mulvaney, P. DNA-directed self-assembly and optical properties of discrete 1D, 2D and 3D plasmonic structures. *Nano Today* **2013**, *8* (2), 138-167.

(10) Sinden, R. R. *DNA Structure and Function*; Elsevier Science, 1994.

(11) Liu, B.; Liu, J. Methods for preparing DNA-functionalized gold nanoparticles, a key reagent of bioanalytical chemistry. *Anal. Methods* **2017**, *9* (18), 2633-2643.

(12) Hurst, S. J.; Lytton-jean, A. K. R.; Mirkin, C. A. Maximizing DNA Loading on a Range of Gold Nanoparticle Sizes. *Analytical Chemistry* **2006**, *78* (24), 8313-8318.

(13) Zhao, Z.; Jacovetty, E.; Liu, Y.; Yan, H. Encapsulation of Gold Nanoparticles in a DNA Origami Cage. *Angewandte Chemie-International Edition* **2011**, *50* (9), 2041-2044, Article.

(14) Bellot, G.; McClintock, M. A.; Lin, C.; Shih, W. M. Recovery of intact DNA nanostructures after agarose gel-based separation. *Nature Methods* **2011**, *8* (3), 192-194.

(15) Thacker, V. V.; Herrmann, L. O.; Sigle, D. O.; Zhang, T.; Liedl, T.; Baumberg, J. J.; Keyser, U. F. DNA origami based assembly of gold nanoparticle dimers for surface-enhanced Raman scattering. *Nature Communications* **2014**, *5*, 3448-3448.

(16) Hurst, S. J.; Hill, H. D.; Mirkin, C. A. "Three-Dimensional Hybridization" with Polyvalent DNA−Gold Nanoparticle Conjugates. *Journal of the American Chemical Society* **2008**, *130* (36), 12192-12200.

(17) Wang, G.; Akiyama, Y.; Shiraishi, S.; Kanayama, N.; Takarada, T.; Maeda, M. Cross-Linking versus Non-Cross-Linking Aggregation of Gold Nanoparticles Induced by DNA Hybridization: A Comparison of the Rapidity of Solution Color Change. *Bioconjugate Chemistry* **2017**, *28* (1), 270-277.

(18) Chen, C.; Wang, W.; Ge, J.; Zhao, X. S. Kinetics and thermodynamics of DNA hybridization on gold nanoparticles. *Nucleic Acids Research* **2009**, *37* (11), 3756-3765.

(19) Hermans, T. M. Multi-step non-covalent pathways to supramolecular systems. Phd Thesis 1 (Research TU/e / Graduation TU/e), Technische Universiteit Eindhoven, Eindhoven, 2010.

(20) Daniel, W. W. *Applied Nonparametric Statistics*; PWS-KENT Pub., 1990.

(21) Ru, E. L.; Etchegoin, P. *Principles of Surface-Enhanced Raman Spectroscopy: and Related Plasmonic Effects*; Elsevier Science, 2008.

(22) Zhang, L.; Ren, G. IPET and FETR: Experimental approach for studying molecular structure dynamics by cryo-electron tomography of a single-molecule structure. *PLoS ONE* 2012, *7* (1).

Appendix

Cage Thermal Stability Simulation: The cavity in our multi-layered cage cast a shadow over the overall thermal stability. We therefore first conducted CanDo (https://cando-dna-origami.org/) simulations to investigate the thermal stability of our 3D cage. The simulations of our cage and a 2D DNA origami tile (Rothemund tile) were performed at default room temperature without modifications. We found that the root-mean-square fluctuation (rmsf), an index of thermal stability in given structures, of our cage was >4 times smaller than that of a regular 2D DNA origami tile (Fig.A.1). The simulation results suggested that our cage, albeit having a cavity, has superior structural rigidity to regular 2D tile and could enhance the stability of the assembled plasmonic molecules by effectively resisting Brownian motions at room temperature.
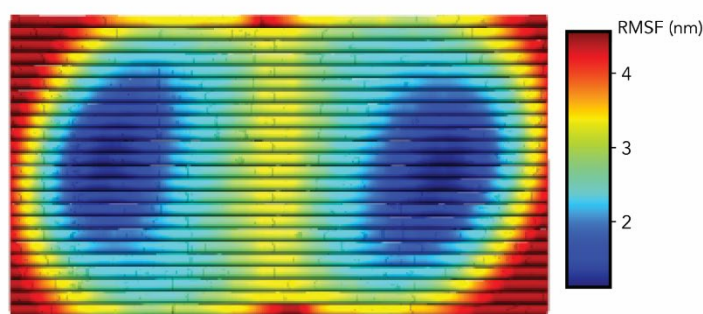
Figure A.1. CanDo simulation results. (a) Rothemund tile has maximum RMSFs value of 6.03 nm, and 95% red region (most flexible) RMSFs ~ 4.12 nm. (b) Our 3D DNA origami cage has maximum RMSFs value of 1.51 nm, and 95% red region (most flexible) RMSFs ~1.05 nm.
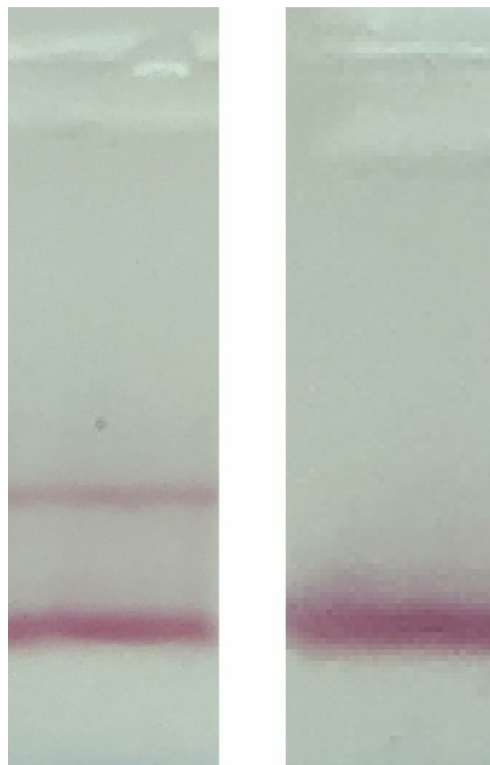
Figure A.2. Agarose gel results of possible cage structural damage after Amicon ultrafiltration. Left: 30 nm fAuNP mixed with purified cage that only has outside capture strands from helices #38 and #106. Right: 30 nm fAuNP mixed with purified cage that only has outside capture strands from helices #39 and #105. The emergence of a slow-moving pink band on the left indicated outside capture strands from helices # 38 and #106 were intact after amicon purification; the absence of a slow-moving pink band on the right, indicated outside capture strands from helices #39 and #105 were partially or entirely lost after amicon purification.
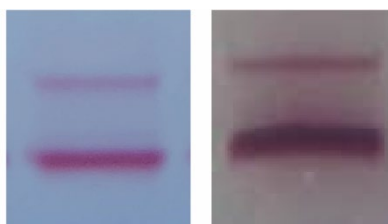
Figure A.3. Effectiveness of thermal annealing in 30 nm fAuNP binding. Left: not thermal annealed. Right: thermal annealed. Both characterized by agarose gel.
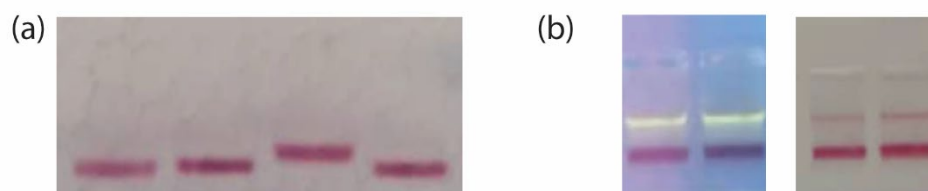
Figure A.4. Extra agarose gel results of 30 nm -10 nm -30 nm trimers. (a) Unstained gel result of 30 nm fAuNP mobilities. From left to right: 30 nm fAuNP in water, 30 nm fAuNP mixed with scaffold DNA in TAB, 30 nm fAuNP mixed with all staples in TAB, 30 nm fAuNP in TAB. The only one that showed slight mobility difference is the 30 nm fAuNP mixed with staples indicating staples might interact with 30 nm fAuNP. (b) Stained gel results 30 nm -10 nm -30 nm trimer, the fluorescence signal (yellow-green band) of cage on the left lined up with the slow-moving pink band on the right.
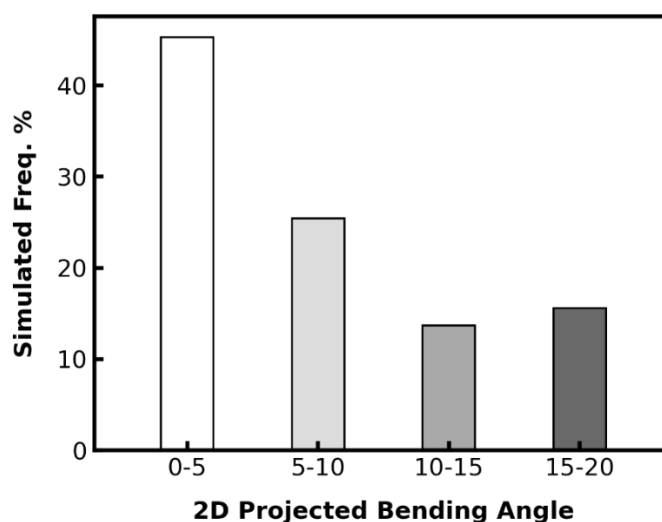
Figure A.5. Simulated histogram of 2D projected bending angle of 30 nm -10 nm -30 nm trimer. Trimers with 3D bending angles that have two populations with normal distribution: $7.0°\pm0.9$ and $18°\pm0.5$ could reproduce the histogram in Fig. 2.31b.
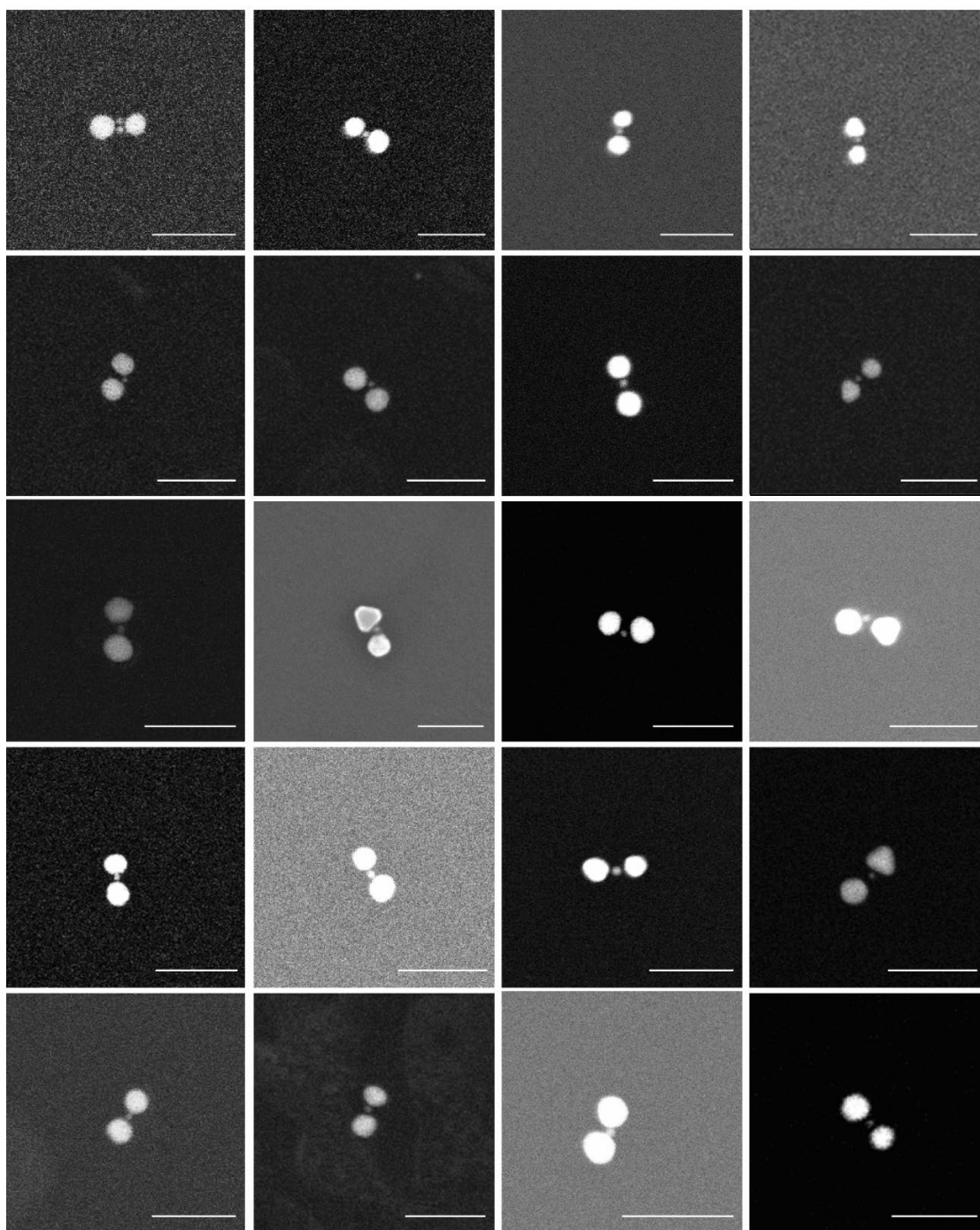
Figure A.6. Additional SEM images of 30 nm-10 nm-30 nm trimers.Scale bar: 100 nm.
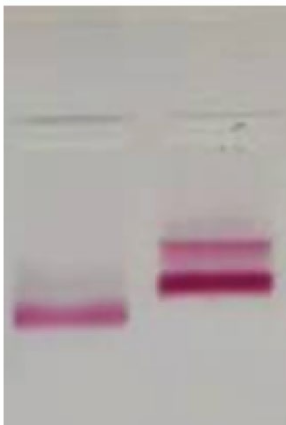
Figure A.7. Extra agarose gel result of 50 nm-10 nm-50 nm trimer assembly. Left: Neat 50 nm fAuNP. Right: Mixture of 50 nm fAuNP and encapsulated product after incubation at RT. The slower-moving band in the right lane is unreacted 50 nm fAuNP and the faster-moving band is 50 nm -10 nm -50 nm trimer. The mobility difference between neat 50 nm fAuNP (left) and unreacted 50 nm fAuNP (right) is likely due to the interaction between staples and 50 nm fAuNP.
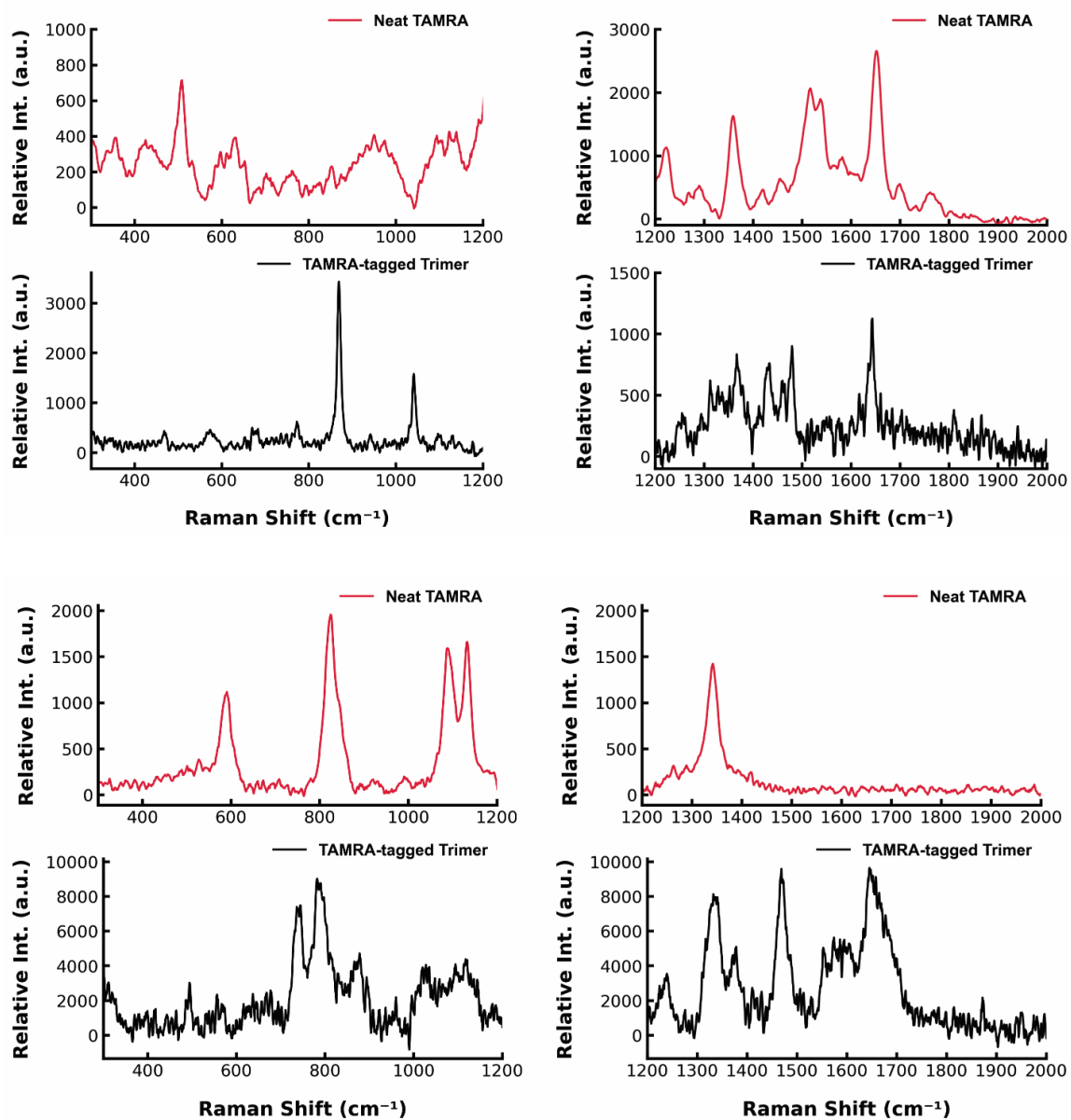
Figure A.8. Extra SERS spectra of 30 nm -10 nm -30 nm trimer. 10 nm fAuNP was tagged with TAMRA. Excitation wavelength: 785 nm.
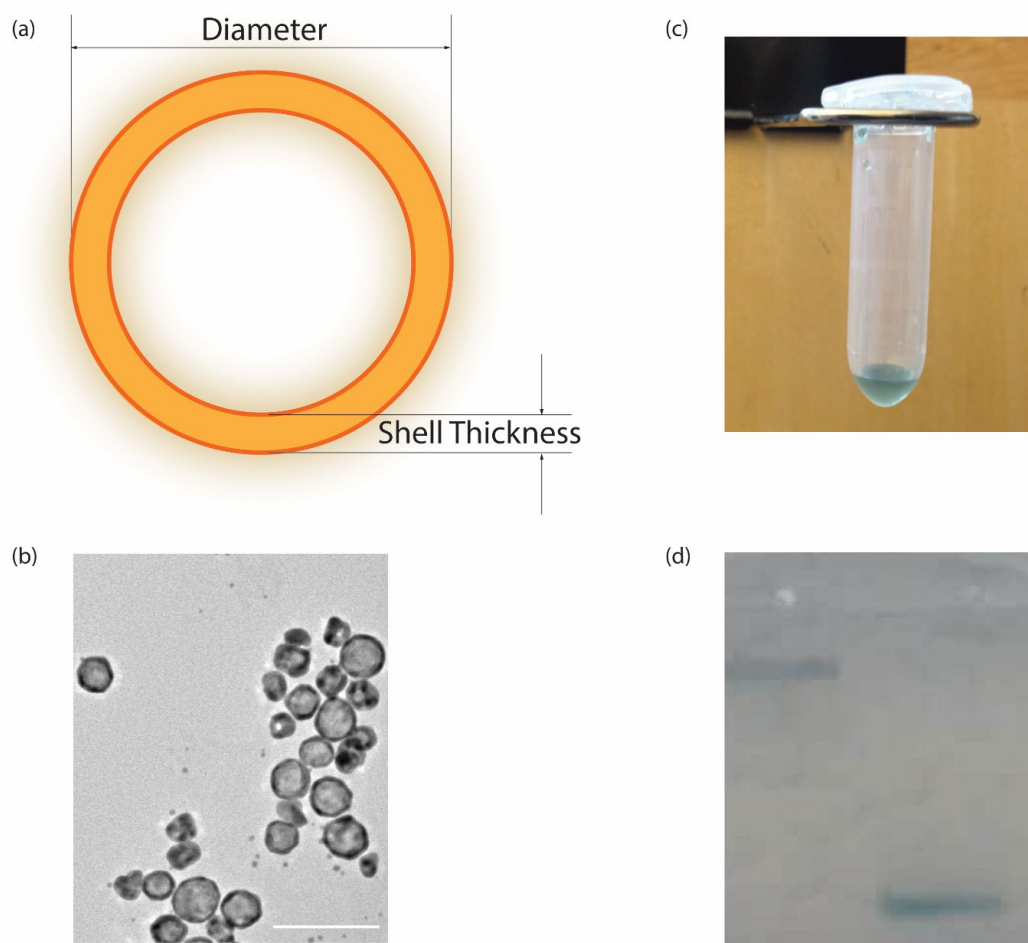
Figure A.9. Hollow gold nanospheres (HGNs). (a) Schematic of HGN. (b) Transmission Electron Microscopy (TEM) image of HGN with 30 nm diameter, 3 nm shell thickness. (c) Photograph of HGN. Diameter: 60-70 nm. Shell Thickness: 5-6 nm. (d) Unstained agarose gel result of HGN with nominal diameter: 50 nm, nominal shell thickness: 10 nm. Left: Bare unfunctionalized. Right: Functionalized with thiolated DNA.
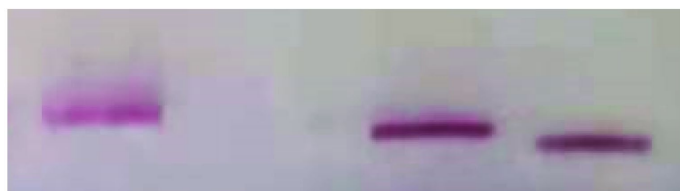
Figure A.10. Agarose gel electrophoretic mobility comparisons of fAuNPs. Left to Right: 50 nm fAuNP, 30 nm fAuNP and 10 nm fAuNP.
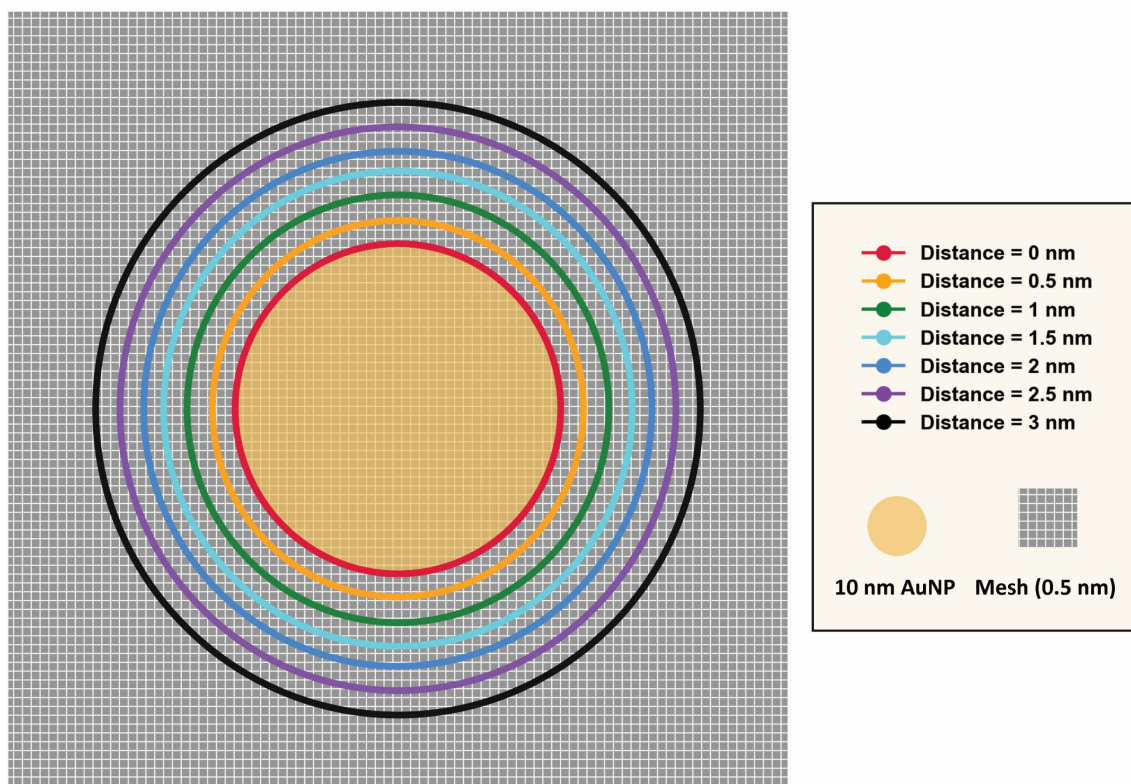
Figure A.11. Illustration of FDTD electric field data extraction.
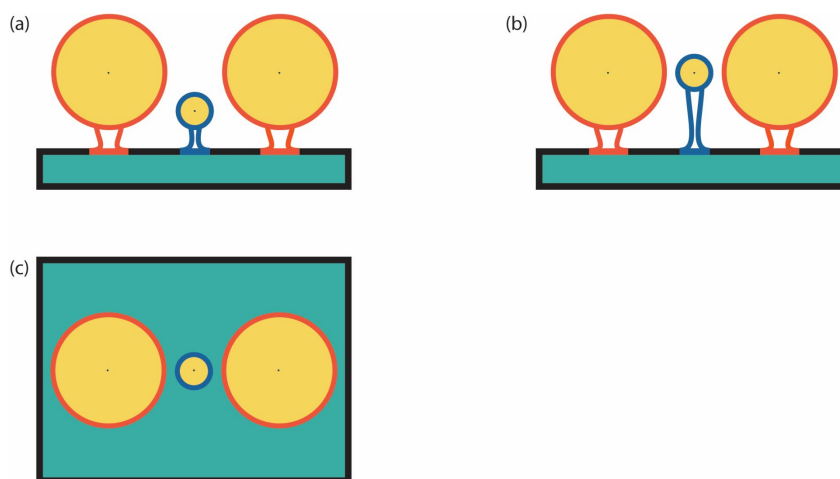
Figure A.12. Schematic of gold nanoparticle assembled on a DNA origami tile. Green squares with black outlines are DNA origami tile. Yellow circles are gold nanoparticles. Red and blue curves/lines are capturing strands of DNA origami tile, red and blue circumference are DNA ligands of large and small gold nanoparticles, respectively. (a) Side view of assembly that has same length of capturing strands for three particles. (b) Side view of assembly that has different lengths of capturing strands for three particles. (c) Top view of (a) and (b).

Helix	Sequence (5' to 3')
#39	**gtaaattgcggaat**TTTTCAGGTCATTCGCAAACCTGTT
#105	TGAAAGTAAGAACGGGTATT**gatgtgcctcactacg**
#38	TGAAAGTAAGAACGGGTATT**gatgtgcctcactacg**
#106	**gtaaattgcggaat**TTATCACCAGTAGCCAATGAAACC
#38	TTGCTCCTTTTGATAAGCATACATTTAGAATACCAAAAACGTAGATT**gatgtgcctcactacg**
#106	TGAAAGTAAGAACGGGTATT**gatgtgcctcactacg**

Table A.1. DNA sequences of outside capture strands. Extensions are in bold lowercase. The two strands having 3' end extensions are for 30 nm -10 nm -50 nm trimers only. 50 nm IPT has no outside capture strands.

Helix	Sequence (5' to 3')
#73	**taatcagcgtttcc**TTTTAAGGCACCCCAGCGGCGCGAAGCGACCT
#41	**taatcagcgtttcc**TTTTCGCGAGCATGCCTGGAAAGGCTCAACCG
#96	**taatcagcgtttcc**TTTTTAAATGTTCCTGTATTTTAACAGCCGAA
#31	**taatcagcgtttcc**TTTTATTCAAGACTCCCCCCATTAGGCCATTT

Table A.2. DNA sequences of inside capture strands. Extensions are in bold lowercase.

AuNP Size	Sequence	Notes
10 nm	GGAAACGCTGATTA*TTTT* 3'-SH	-
10 nm	GGAAACGCTGA***T(TAMRA)***TA*TTTT* 3'-SH	**TAMRA** attached to a T
30 nm or 50 nm	5' ATTCCGCAATTTAC*TTTT* 3'-SH	-
30 nm or 50 nm	SH-5'*TTTT*CGTAGTGAGGCACATC	For 30 nm - 10 nm – 50 nm
50 nm	5' TAATCAGCGTTTCC*TTTT* 3'-SH	For 50 nm IPT and Fig.2.28

Table A.3. DNA sequences of thiolated DNAs. 4 italic Ts are spacers, not used for hybridizations.

#	Sequence (5' to 3')
1	TTACAAAGCTGTAGGGTGTCTAATTCTG
2	ACAGGAACGGAATTTTGTTTGGGGATGTGTAAAACGCCAAGC
3	AGGCCTACCCCTTATAAAGGTAACCGAT
4	AATAATAATTTACTACCAGGTTAGGATTAGCGGG
5	ATTACTAGTTTAGTATATACAAGTAATTTTCGCCATAAAGGTAGTCCAGA
6	CGAACGAACAGGCAGTAGCATTTTGGGG

7	ACCGAAGCCCAATAATTATTT
8	ACAACATAATTGTTATGATATCGGAGAC
9	ACTCCTTCATTACCCAAAGTAAGACACC
10	TCAGATATAGAAGGCTTCTAAGAACGC
11	GCCCTAATTAAAAAACCACCAAGTATGT
12	ATAAAGTACCGACAGTAGTCACCAATTTAACCTAGGGCACAGTCC
13	TAGTATTATCCGTCCAGGGAACGGGAGAGCCAAAG
14	TGTTCAGCTAATGCAGATTATCAAGTATCACGATATAAGTATAGC
15	TGTAGCATGTACCGGAACAACTGAAAATATTGTATCGGTTTATCA
16	TTTTAACAAGAGAATATCGCATTAACT
17	ACAAAGCGTGAATAGGTTTAAAATCATT
18	AAAAATGGAAAATAATTACGCGCAGAAG
19	GTGCCCGTACTCATCGAGCCGTTT
20	CGAACGTACCAGAATCAGGCTCTGGCGA
21	AAGGAATATAAAAAGAGAGGCATAGCGTC
22	CTGAGAGAGAGGTGGATTAAG
23	TTTTGAAAATAAGACAGCCATATAAGAGCACAAGATGTACTGTACATGG
24	TTTAAATGCATGAAAAGTTCTACTTAGAGCTATATAATATCGCGCAGA
25	AGAAGGATTTTGTTCGACTTGACAATTT
26	CGGCTGTCATTCCATTAAGAACCTATTATTCTGA
27	ACGGATTCGCCTGATTGAAGATTAGTCAGTATAGTTTGACTTAAC
28	GCCTGATAAATTGTGTCGGAACGATGACCAATTGAGAT
29	ATAGAAAATTTTCATATTACCGCGTTAGAGCGCACCGAGAGAA
30	CGCCAGCCCACCAGCCACCCTACCGGAACCGCCTC
31	TGCCCGCGGAAACCATCCTGAATCATCAAGAAACCTATTAATCGTATTA
32	TGCAACTGGAAGCAGATTAAGAAAGATG
33	GCTTTCGAGGCATCGCCCGATATATTCGGTCTGCGGGAAACGAGG
34	GTTATCTTAGGAGCGCATCGTAAC
35	AAAAGGAAGCTTGATGCGCCGCTTGCAG
36	ATTCAAACGGTTGTAAATCATGTAGATT
37	TTTCCAGAGCCTGAACAGTAATTGGGGAAGGCGGAAATAGAGCCAGCA
38	TAGCAATGGAAAGGTAATAAGAAACGCTCCTACAT
39	GGGCCTGAAAAAAGTAAACACCAACCAA
40	ATTGCATTAATACTAAGCCTT
41	TAAGAATAACAATATCTATTAGGCGAACT
42	ATGCCACAGACAGACGGCTAATTAAAGGC
43	TTTACAAACAATTCGATTTAGTGCCGGAGCCAGCTTTCCGGC
44	ACGTCACACCATTATCATTAACCGTTCC
45	TAAGGCGTTACCAGACGCTCATTAATTGGCCACCCGACAATAAAC

46	CAGTATTGCAACAGAACGCCATTCGCGTCTGGCCTGAGCGAGCGGCGGA
47	AGTTGAAGATTAGAGTCACGTGACAGTA
48	AACGCAACATAAAGTAAATCACACGCCAAACATAACAAATGCTCTTTAC
49	GCAACTTGAGAATCAATCCAACTAACGA
50	TGAATTTAGGACTAGGGTAAAAAACGAA
51	CCAGACCAAAGTACCTCAACATTTTGCG
52	CTTAGCCGAAATCCACAAAGTGTAGCAA
53	ATGGATTACAGATTCCGACCAGGACATTCAGATAGACCTGAAA
54	TTTTAAGAATAATACAATCCAGCCTTAAATC
55	GGAATACCACATTCTTCATCATTAATAAAGGACGTTGGGAAG
56	AAACGAGAATCAAAGACGACGTACGAGGGCAGATA
57	GAACACCCTAATTTAAATAAAAACGATTAACCGAGCTGGCATAGGCGGT
58	GGTTTACCGGGGTCTTAATGCTTTCGGAGGCTGAG
59	TTCATTAGAGAAACGTAGTAAGCGATTT
60	TGAAAGTAAGAACGGGTA
61	GGGTCGAGTGCCAGAGTAGCGGCCGGAA
62	AGGCTTGAGAAAGAAACTAATCATAGTA
63	AGAACGCTTTCAAATTAATTTCGGAATC
64	CCTCAGAGAATTAGGATTCCCGGAAGTTAGCTTCA
65	TTTTTGTAATACAATGCAAATATAAAGGCCACAG
66	AGAGGCACTAAAACAGATTTGTAT
67	GGCAAATTGAAAAATAATGGGTCAACAT
68	GCTAAATAGGGTGAAGTAATGGATAAAA
69	GCTGCAAACGCCAGGCGCAACCAAAGCGATAATAC
70	CGTAATCACGCAAGTGTAGGTATTTTCA
71	AGTACATCCTTTATAACTCCAACATATA
72	TCTTTTCCGCGCGGCCAGCTGTGCGTTGAATGAGT
73	TACCAACCCAGCTCGGGAGG
74	AGAGCAAACCCTCGTTTTGCCATAGTAAAATGTTTCATAAATGTTCAGA
75	CCTTATTTCATCGGAGAGCCGATTGACA
76	TGAGGGAAGCGCTAGATAACCCAAGAAA
77	GCCACCCCACCCTCCATTTTCAATCAAG
78	AATCATAGGTTCGCAAGTATGTAATTCTGACTGGTTTGCGTGTGAT
79	TGCTCAGGAGCATGTCAATAAT
80	GACATTCGAATTATGACTTGACACCTTATCTTTAGACATCCT
81	CCTTTTTAGTACATAAAT
82	TAATTTTTTCACGTTAAAGGAACAACTTAATTTTCTGTATGG
83	TAGCTATAACCCTGTATGAAGTTAATGCCGAATAA
84	GTTTGAGATTTTGCAAGGGCGGCCTCTT

85	AATACCCAAAAGAAGAAACGCAAAAGTACTATCTT
86	AATTATTCATTTCAATTCCGAAAGAAGCGAA
87	CCAAAAAAATTACAAAACAAACATCAAGAACAGTACGGGAGAAAC
88	ATAAAAGAGTCACAACTTTACACAATAGCAAGC
89	CCCTGACCCCAAATCTTGACA
90	ATAAAACCCAGCAGGCTCATTGCCAGCTT
91	AACCAAGTACCGTCACCCACCGCATAAACAGAGTGCCTTGAGTAA
92	GATGGGCACTAACAATTTGAGGACAACTTTTAAAA
93	AGAAGGACGGATAAGAGGGTTCGGCCAC
94	GAATCGTAGACTGGTTTTGCATAACGGATACAGGT
95	AGAACCGTGACAGAAGAGGCACATGTTA
96	TATTTCAATTAGCTGAGGGGGAAATTATTTGCACG
97	TAGGGCACAAATATTCATATTTATTTT
98	GCCACCAGAGTTTCCAAACTAAGTTTTG
99	CAAACCCTCAATCATTGCTGAGAACAAATAACAACCCGTCGG
100	TACCGTCTTAAATATACCGACAAATACG
101	TAACATCAGGTCATTGTTTTACTTTGAACAAAAGA
102	ATTATTCATGCTGAGATTGGGTTAGGTA
103	ATAGCAGCACTTAGCGTCGCGTTTAGCGTTTGCC
104	TAGAAAGTAACACTCCCTCAT
105	GGAAGCAAGCCTGGCGACGTT
106	TATTCCTTCACCGCTGGTTTT
107	TTAGAACGGTCATTCTGGAGCATCGATGGTAAAACATCATAT
108	CCCGGTTAAAGCCCAAGATTGTATTTAA
109	TTTGGGCCGTATTGATAGTCGTTTCCAC
110	TCATTATACCTTATATTGGGCCTTTGAA
111	GCATCAAAGGAAGCACCTGAGTACCAAG
112	GGCAATTCATAAGTTGGGGTTTTCGTCGACTCTA
113	GACGTTAGATCTAACAACGCC
114	GGCTTTGCTTAAACGCCTTTACTCCAAACTACCAGCCGGACAATAGCCC
115	CATCTGCCAGTTTGAGGCACTCCAAACCAGGTGTTGGGGGAACAA
116	GGGAATTTATTCATAGCGTCAGTAATAAG
117	CGTCAGACACCCACTCAGAACCTCAGGAGGTTTAG
118	TTCCATAAATGATATACTGCG
119	ATCCAGTGACGGCACTACCATTTCTGAATAATGGA
120	TTGCTCCTTTTGATAAGCATACATTTAGAATACCAAAAACGTAGA
121	TCGGCCAAACCAGTGCAGCTGATTGCCCTGATTATCAGA
122	ATCCCCGGGTGAACCCTCAT
123	TTTCAGGAAAATCAAGCCACCCAGAACC

124	CTCATAGTTAGCGTAACGTAAATGTCAACAGCAACAAC
125	TCGAGCCTTTTCGTCCAACATATATAGT
126	ACTAATAAGGAATTGTCAGTT
127	ACTTCAAAAGCAAATCTTTACTTAAACAATTCATTGAATCCC
128	ATTGTAATAAAGCATCATAGCTGATAAA
129	AGTTTCCATTAAACAAGACTTGCATCGGTCGTCACCCTCAGC
130	CGGTTTGGCCAGGGCATTGCA
131	TGAACGGTTTGACCCAACCTAATACGTA
132	TATCAATAAGAGAGCGATAGCTGATAGC
133	GCAATAGAGCAGATCAATAGGTGCCACGCATCACCATATCTGGAGGAAG
134	TCAGATACGCCACCAAAAAGGAAGAGAA
135	ATATATGTGAGTTAGATT
136	CAAAATTTAACCTTATCGTCGATTTTCC
137	AATCCTTTCAATAGCCATTCGCCTCAGG
138	ACAACGGACTCATCTGTACAGGAGTAATCAACGTA
139	GATGGCTAATAGTAAGGCAAAGCATAAA
140	GAATTTAAGCCAGATCACAAACAGGTCA
141	CGCTTTGCTGAGGACAATGATTTCAGCGGAGTCGCTTTCCA
142	ATTTTTAACCGAGCTGTGTGAACGAGCC
143	TTCTAGCTGTTTCCTCGAATTTTGCATG
144	TTAGTTGCTATTTTGCACGCTAACGAG
145	CCTGCAGCCAGTCAGGTGCCTCGCTCAC
146	ACAGAGAATTTTTGAAAGGCT
147	TTTCATAATCGATAGCAGAACCCATTCCACAGAC
148	CGTGGCGTGTCTGAACCCTCC
149	CGAAACTAATGAAACAATTTCATTTGA
150	ACCAGGATGAAAACCCAATTACTATTAA
151	ACGCTGAGAGTGAATTTA
152	ATCCCAGGGCCTGTACGCGTCGAACCGC
153	ACAAATACAATGGGAATTACAGCCAGAACTGAATCT
154	TTTGCCTCGTAATCGTTGAGGCAAATAA
155	GTGAATTACCAGTCAACGAACAAAGAAGTTTACCAAATCAGGGCGGATT
156	AAAGAGAAAACAGGGAATTGGTTTACTTACGCTCAATCGTCT
157	CATAACGATATTATACAACAGAACTGGC
158	AAGATCGGGACGACTGGTGTATTGACCGTCTAAAG
159	CTGACCTTCATCAAACCAGGCACCGAACGGCGCAGACGGTCA
160	GAATCCTGAGACTACTCCGGCTTATATA
161	CGCTATTGGCGATTCAATATATGTCGTGGGAGAGG
162	TCTCAGAGATAAGGCCTGTCA

163	CGTTTTAGCGAACCTCCTAACGTCTAACATAAATAAGT
164	TAGTCAGATATCGCGTTT
165	CACATTAATCATTAATGATT
166	TTCAGAGCCGCGACGATTGGTT
167	TAATTCGTCATTCCATTT
168	CTTCTGGAAGTATTTTATCTTAAAATTT
169	TTTTTGTAGCAGACTTTT
170	AACAGTTCAAAATTTTATCAAGTGGCTT
171	TTAAATCTACGGTTGAGA
172	TTCAGATGAAGGAGAGTACCT
173	CATCAATATCCGCTCATT
174	TTGCAGTCTCTCTTTTGATGTT
175	TTTTGAATCCGTAGTTTT
176	TTGGAATAGGTCAATAGAACAAGAAA
177	TTTCTCCGTGGACCTCAAATTT
178	TTTGTAAACGTTTAAAATTTTTTGTGTGGCAAAAACGTAAAAATAGCATT
179	TTATACAGGAGATTGAGT
180	TTCCTTGATATATGGAAAGCTT
181	TAAGGGAGCATAGGCTTT
182	TTCGAAAGACATTTCATGAGTT
183	TTTCAGAGCCGAACCACCACTT
184	TTTTAGAGGAAGTCTTTT
185	TTTTTTGCTAAATTGCGAATTT
186	TTCAATTCCACGAGCTAACTTT
187	AGAGGCAAGTAATAAGAGATT
188	TTTCAAATGCTCCTGACT

Table A.4. DNA sequences of unmodified staples.

	Mean Value	Standard Deviation
Diameter of Terminal AuNP	29.44 nm	2.76 nm
Diameter of Central AuNP	7.86 nm	0.87 nm
Gap Size	3.66 nm	1.51 nm

Table A.5. Size measurements of 30 nm-10 nm-30 nm trimer.

	Mean Value	Standard Deviation
Diameter of Terminal AuNP	46.27 nm	3.77 nm
Diameter of Central AuNP	7.72 nm	1.40 nm
Gap Size	3.46 nm	1.77 nm

Table A.6. Size measurements of 50 nm-10 nm-50 nm trimer. Gap sizes might be inaccurate due to distorted structures.

	Mean Value	Standard Deviation
Diameter of Large AuNP	46.71 nm	7.13 nm
Diameter of Large AuNP	7.26 nm	1.19 nm
Gap Size	3.34 nm	1.70 nm

Table A.7. Size measurements of 50 nm IPT.

Neat TAMRA 785 nm	Neat TAMRA 633 nm	Trimers 785 nm	Trimers 633 nm	Origin	Assignment[1-5]
649 cm^{-1}	1652 cm^{-1}	1647 cm^{-1}	1642 cm^{-1}	TAMRA	C-C stretch xanthene ring
-	1582 cm^{-1}	1586 cm^{-1}	-	TAMRA	C=C ring stretch
1567 cm^{-1}	1562 cm^{-1}	1554 cm^{-1}	-	TAMRA	N-H bend
1534 cm^{-1}	1537 cm^{-1}	1529 cm^{-1}	-	TAMRA	amide II
1515 cm^{-1}	1517 cm^{-1}	-	-	TAMRA	C-N stretch, C-H bend, N-H bend
1509 cm^{-1}	-	-	-	TAMRA	ring vibration, C=C in plane vibration
1498 cm^{-1}	-	-	-	-	-
1455 cm^{-1}	1455 cm^{-1}	1469 cm^{-1}	1477 cm^{-1}	TAMRA	ring vibration
1414 cm^{-1}	1417 cm^{-1}	1415 cm^{-1}	1433 cm^{-1}	-	N-C stretch
1356 cm^{-1}	1360 cm^{-1}	1376 cm^{-1}	1366 cm^{-1}	TAMRA	C=C stretch xanthene ring
1287 cm^{-1}	1289 cm^{-1}	1333 cm^{-1}	-	TAMRA	N-H bend, CH$_2$ wag
1266 cm^{-1}	1267 cm^{-1}	-	1253 cm^{-1}	TAMRA	C-O-C stretch
1219 cm^{-1}	1223 cm^{-1}	1235 cm^{-1}	-	TAMRA	-
1189 cm^{-1}	1190 cm^{-1}	-	-	TAMRA	-
-	1123 cm^{-1}	1118 cm^{-1}	1129 cm^{-1}	TAMRA	C-H in plane bending

962 cm⁻¹	-	962 cm⁻¹	-	-	-
-	-	866 cm⁻¹	869 cm⁻¹	DNA	P-O5 + ribose ring breathing
842 cm⁻¹	852 cm⁻¹		842 cm⁻¹	TAMRA	-
-	-	782 cm⁻¹	785 cm⁻¹	DNA	Poly(dG-dC)
757 cm⁻¹	762 cm⁻¹		772 cm⁻¹	TAMRA	C-H bend out of plane
739 cm⁻¹	742 cm⁻¹	739/745 cm⁻¹	736 cm⁻¹	TAMRA	-
698 cm⁻¹	702 cm⁻¹			TAMRA	-
677 cm⁻¹	674 cm⁻¹	677 cm⁻¹	670/677 cm⁻¹	DNA	Thymine
-	652 cm⁻¹	656 cm⁻¹	653 cm⁻¹	TAMRA	C-H out of plane bending
642 cm⁻¹	630 cm⁻¹	637 cm⁻¹	636 cm⁻¹	DNA	C3'endo anti-thymidine
627 cm⁻¹	628 cm⁻¹	625 cm⁻¹	621 cm⁻¹	DNA	Guanine + ribose ring breathing
610 cm⁻¹	610 cm⁻¹	617 cm⁻¹	-	TAMRA	aromatic C-C stretch
570 cm⁻¹	572 cm⁻¹	573 cm⁻¹	572 cm⁻¹	TAMRA	-
555 cm⁻¹	-	557 cm⁻¹	-	-	-
-	532 cm⁻¹	532 cm⁻¹	532 cm⁻¹	-	-
500 cm⁻¹	506 cm⁻¹	493 cm⁻¹	-	TAMRA	-
-	-	486 cm⁻¹	486 cm⁻¹	DNA	-

Table A.8. TAMRA peak positions and assignments. 633 nm and 785 nm excitation wavelengths.

Reference

(1) Gong, T.; Kong, K. V.; Goh, D.; Olivo, M.; Yong, K. T. Sensitive surface enhanced Raman scattering multiplexed detection of matrix metalloproteinase 2 and 7 cancer markers. *Biomed Opt Express* **2015**, *6* (6), 2076-2087.

(2) Prinz, J.; Heck, C.; Ellerik, L.; Merk, V.; Bald, I. DNA origami based Au-Ag-core-shell nanoparticle dimers with single-molecule SERS sensitivity. *Nanoscale* **2016**, *8* (10), 5612-5620.

(3) Prinz, J.; Matković, A.; Pešić, J.; Gajić, R.; Bald, I. Hybrid Structures for Surface-Enhanced Raman Scattering: DNA Origami/Gold Nanoparticle Dimer/Graphene. *Small* **2016**, *12* (39), 5458-5467.

(4) Yang, J.; Palla, M.; Bosco, F. G.; Rindzevicius, T.; Alstrøm, T. S.; Schmidt, M. S.; Boisen, A.; Ju, J.; Lin, Q. Surface-Enhanced Raman Spectroscopy Based Quantitative Bioassay on Aptamer-Functionalized Nanopillars Using Large-Area Raman Mapping. *ACS Nano* **2013**, *7* (6), 5350-5359.

(5) Clark, R. J. H.; Hester, R. E. *Spectroscopy of Biological Systems*; Wiley, 1986.